Effects of capillarity and heterogeneity on flow of organic liquid in soil

Effects of capillarity and heterogeneity on flow of organic liquid in soil

Eva Louise Wipfler

Abstract

In this thesis we study the movement, interaction and (re-)distribution of three fluid phases: water, NAPL and air in water-unsaturated soil. We focus on two problems: non-drainable residual NAPL and the effect of soil layers on the redistribution of NAPL after a spill. Until now non-drainable residual NAPL has not been incorporated into multi-phase flow models. We develop a constitutive set of saturation-capillary pressure relationships that accounts for non-drainable residual NAPL. These relationships are derived from a conceptual pore scale model of which the soil is represented by packed spheres. To test the constitutive model, we develop an experiment to measure three-phase $P_c - S$ relationships and non-drainable residual saturation including independent measurement of the water saturation and pressure. We measured residual NAPL saturation up to 0.08, however, extra measurements are needed to test the residual model. Considering the effect of layered soils, first, we study the effect of an inclined soil layer with respect to the watertable on the redistribution of infiltrating LNAPL from a point source at the soil surface. Two experiments are performed using a sand filled transparent chamber. One experiment consists of LNAPL infiltration into a fine sand matrix containing a coarse sand layer and the other experiment consists of LNAPL infiltration into a coarse sand matrix containing a fine sand layer. Fluid contours were obtained using a digital camera. We modeled the experiments numerically. The numerical simulator predicts the experimental results adequately . In addition, we considered DNAPL infiltration into a water unsaturated porous medium that consists of two horizontal layers, of which the top layer has a lower intrinsic permeability than the bottom layer. We develop an analytical approximation to estimate the DNAPL pressure and saturation and the horizontal extension of the DNAPL plume just above the layer interface at steady state for low water saturations.

Keywords: Non-Aqueous Phase Liquids, three-phase flow, unsaturated zone, residual saturation, constitutive relations, heterogeneous porous media, numerical modeling, analytical solutions, experiments.

Contents

Chapter 1

Introduction: NAPL infiltration in unsaturated porous media

1.1   Introduction

Soil and groundwater contamination by Non-Aqueous Phase Liquids (NAPLs) such as organic solvents, gasoline and other petroleum products, is widespread due to leaking storage tanks, spills, and improper disposal. Although NAPLs are relatively immiscible with water, understanding the behavior of these liquids in the subsurface is important since solubility may exceed drinking water standards. After release, NAPL migrates as a separate phase downward by gravity with some lateral spreading due to capillary forces. If sufficient NAPL has been spilled, eventually, it may reach the groundwater surface. If it is less dense than water (Light-NAPL) it will accumulate as a liquid lens that floats on the groundwater surface. If it is denser than water (Dense-NAPL) it displaces groundwater and continues downward migration until it encounters a hydraulic or capillary barrier. Floating LNAPL can partly be removed by creating a pumping well (Mercer and Cohen, 1990). The LNAPL will flow towards the well facilitated by the groundwater table gradient and can be pumped into a recovery tank. Although removing DNAPL is more difficult and pressure gradients must be high, DNAPLs can be pumped out of the subsurface as well. Not all of the NAPL can be removed, since some of it is retained in the capillaries of the porous medium. This remaining NAPL can be contained hydrologically or can be removed by other techniques such as air sparging or bioremediation. To predict the NAPL that was left behind in the unsaturated zone after remediation by pumping, the mechanisms that are responsible for the flow and retention of NAPL must be understood. Therefore, such understanding is a major motive for studying the movement, interaction and

1

distribution of three fluid phases, i.e. water, NAPL and air in a porous medium: the subsurface.

The physical systems that are of interest to researchers studying NAPL contaminant transport are in many ways similar to petroleum reservoirs. In both type of systems, an aqueous phase and a non-aqueous phase coexist in the pore space of a geological matrix. In addition, often a gaseous phase is present (e.g. air in the unsaturated zone or gas in case of gravity assisted gas injection in petroleum reservoirs). In fact, many NAPLs are petroleum derivatives. Petroleum reservoirs have been studied for decades whereas subsurface contamination by NAPLs has only recently become of interest. Therefore, petroleum reservoir models form a foundation for NAPL contaminant transport models. Both petroleum reservoir models and NAPL contaminant transport models are multi-phase flow models that are based on mass conservation of each fluid phase. Gravity and pressure differences are the driving forces for fluid flow. To date, multi-phase flow models developed for modeling NAPL contamination include those of Faust (1985), Abriola and Pinder (1985), Kaluarachchi and Parker (1989) and White at al. (1995). One of the most notable differences between reservoir models and these models is that in contrast to reservoir models, it is assumed that air is at atmospheric pressure and pressure differences in the air phase are negligible. In addition, capillary forces appear to be especially important in NAPL contaminant transport problems. Capillary forces are due to interfacial tensions between the fluids and the solid in the capillaries (pores) of a porous medium (we refer to Section 1.2.2 for a detailed description of capillary forces). Since velocities are small, capillary forces highly control the distribution of the fluids in the porous medium. Furthermore, the aim of contaminated subsurface studies lead to a relatively important role for capillary forces. Usually, quantification of the unremediated NAPL is needed. This NAPL is retained in the pores due to capillary forces.

Although water, air and NAPL are distinct and separated by interfacial boundaries, some dissolution of NAPL components may occur into the groundwater. Therefore, subsurface models often include dissolution of NAPL components into water. In this thesis, however, we focus on the physical mechanisms of immiscible flow, and therefore, dissolution of NAPL is not taken into account. In the next section, a brief introduction to multi-phase flow and multi-phase flow modeling in porous media is given, with special attention to the role of capillary forces. Next, two relevant issues are introduced that are specific for three-phase flow in the subsurface. These

issues are studied in detail in this thesis.

1.2   Three phase flow

The conventional three-phase flow model consists of three mass-balance equations for water, NAPL, and air separately. We assume a rigid porous medium and the fluids are assumed to be incompressible. There is no mass exchange between the phases and no chemical reactions are considered. In the absence of sources and sinks, the mass-balance equation for water, NAPL, and air is given by:

$$\phi \frac{\partial S_i}{\partial t} + \nabla \cdot u_i = 0 \qquad i = w, o, a \tag{1.1}$$

u_i is the Darcy velocity of phase i and ϕ is the porosity, S_i is the saturation of phase i. The first term in Eq.(5.3) accounts for the accumulation of fluid whereas the second term accounts for the fluid flow. For most subsurface models, pressure differences in the gas phase (air) are assumed to be negligible as air is assumed at atmospheric pressure. This implies that the mass-balance equation for air can be eliminated and only two mass-balance equations (w,o) have to be solved. Eq.(5.3) is subject to the following constrains:

$$S_w + S_o = S_t, \qquad S_t + S_a = 1, \tag{1.2}$$

where the subscripts w=water, o=NAPL, a=air and t=total. Capillary pressure-Saturation relationships and Relative permeability-Saturation relationships are both constitutive relationships that are needed to close the set of Eq.(5.3). The *capillary pressure*, p_c, is the pressure difference between the pressure of phase i and the pressure of phase j.

1.2.1   Darcy velocity

Flow in porous media at a REV [1] scale is first described by Darcy (1856) who studied water flow through a sand column. Darcy's empirical law has since been the foundation for mathematical analysis of flow in porous media. A general version of Darcy's law can be written as:

$$u_i = -\frac{\mathbf{k_i}}{\mu_i} \cdot \nabla \left(p_i - \rho_i g z \right) \tag{1.3}$$

---

[1]Representative Elementary Volume that gives the scale at which averaged macroscopic parameters can be assigned like porosity, permeability and saturation

which gives the velocity for a fluid phase i. $\mathbf{k}$ is the intrinsic permeability tensor of the porous medium, which is a measure of the ease with which a fluid flows through a porous medium. It is porous medium dependent. g is gravity and p_i, ρ_i and μ_i are respectively the pressure, the density and the viscosity of the fluid i and z is the vertical coordinate. Darcy's equation (1.3) only holds for laminar fluid flow, non-deformable media and no density differences in one fluid. Gravity and pressure differences cause the liquid to move, where the first is also referred to as *buoyancy force*. The force or resistance that the porous medium exerts on the moving fluid is generally referred to as *viscous force*. It is proportional to the flow velocity of the fluid and the fluid viscosity, and inversely proportional to the intrinsic permeability.

To account for the resistance due to the presence of other fluid phases in the system *relative permeability* k_{ri}, is introduced in the Darcy equation:

$$u_i = -\frac{\mathbf{k}k_{ri}}{\mu_i} \cdot \nabla\left(p_i - \rho_i gz\right) \tag{1.4}$$

The relative permeability depends on the degree of contact with the solid, on the contact of the fluids with each other and on the distribution of the fluids within the porous medium. Generally, relative permeability is an empirical factor that lumps the effects of the complex interaction between the fluids and the porous medium. In most cases it is less than or equal to unity and the total sum of the relative permeabilities is generally less than unity since the fluids interfere with each other. Relative permeability is a function of the saturation of the different fluid phases.

1.2.2   Capillary Forces

If the pore space of a porous medium is occupied by more than one fluid, *the capillary force* arises. Capillary forces are incorporated in macro scale multiphase flow problems by the constitutive Capillary pressure-Saturation- Relative permeability relationships. Capillary forces are the result of the interaction between the fluids phases (interfacial tensions) and the interaction between the fluids and the porous medium (surface tensions) at the micro scale. In the following, we will first describe the forces at micro scale. Then, we introduce (macro scale) $p_c - S$ relationships and $k_r - S$ relationships and we discuss some typical features of these constitutive relationships.

The *interfacial tension* is the force per unit length acting on an arbitrary line on the interface between fluids. It results from the difference between
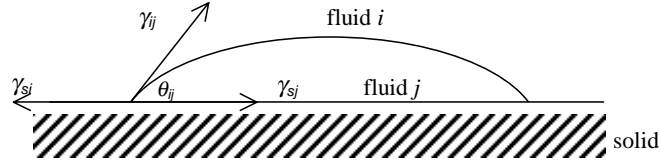
Figure 1.1: Fluid configuration in contact with a solid s. j is the wetting fluid and i is the non-wetting fluid. θ_{ij} is the contact angle and γ is the interfacial tension.

the mutual attraction of molecules within a liquid phase and the attraction of dissimilar molecules across the fluid interface. At the interface, the force that acts on the molecules is inward and therefore it costs extra energy to move particles from within the liquid to the interface. Hence, one may think of interfacial tension as the energy needed to create a unit area of interface. The *surface tension* is similar to the interfacial tension but is used for the attraction between a fluid and a solid. Fig. 1.1 shows two fluids, or a gas and a fluid in contact with a solid phase.
Equilibrium requires that:

$$\gamma_{ij} \cos \theta_{ij} = \gamma_{si} - \gamma_{sj} \tag{1.5}$$

Eq.(1.5) is called Young's equation, where γ_{ij} is the interfacial tension between fluids i and j (s refers to solid). θ_{ij} is referred to as the contact angle. If $\gamma_{ij} + \gamma_{sj} < \gamma_{sj}$, then θ_{ij} is zero and the liquid will spread indefinitely over the solid: the liquid j is completely *wetting* the solid. *Wettability* is defined as the ability of one fluid to wet or spread onto a solid surface in the presence of another fluid phase. When $0 < \theta < 90°$ the liquid j preferentially wets the solid above liquid i. It is said that the fluid partially wets the solid. The contact angle may be subject to hysteresis as the advancing contact angle might be different from the receding contact angle. This hysteresis is due to surface roughness and surface heterogeneity (Morrow, 1975). Most mineral surfaces of natural porous media are strongly water-wet (Anderson, 1986),
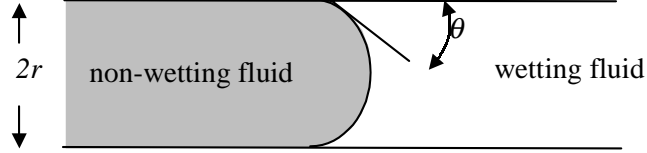
Figure 1.2: Fluid distribution in a capillary with radius r.

although, wettability might change due to surface modifications induced by NAPL presence (Zheng and Powers, 1999). Generally, it as assumed that the solid has a wettability according to the sequence water > NAPL > air. In this thesis is assumed that the porous media are water-wet.

The curvature of the interface of two immiscible fluids gives rise to a pressure difference which is proportional to the interfacial tension and the curvature:

$$p_i - p_j = \gamma_{ij} \left(\frac{1}{R_1} + \frac{1}{R_2} \right)$$
(1.6)

R_1 and R_2 are the principal radii of curvature and p_i and p_j are the pressures at the fluid phases i and j. i is the phase at the inside of the curvature (the non-wetting phase) and j is the phase at the outside of the curvature (the wetting phase). Eq.(1.6) is known as the Laplace equation. The pressure difference is called *capillary pressure*, p_c^{ij}. For a capillary tube with radius r yields (see Fig 1.2):

$$p_c^{ij} = \frac{2\gamma_{ij}}{r} \cos \theta$$
(1.7)

At macro- or REV-scale, the wetting phase is drawn into the porous medium and the non-wetting phase is expelled by the porous medium due to this capillary difference. Similarly, the wetting fluid preferentially stays in the smaller pores, and consequently, the non-wetting fluid stays in the larger pores of the porous medium. One can relate the total amount of

wetting fluid drawn into a porous medium to the pressure difference between the wetting and the non-wetting fluid over this porous medium. This leads to the characteristic macro scale relation for a porous medium, the so-called $p_c - S$ relationship. However, due to the complex geometry of natural porous media it is difficult to describe these relationships analytically. Leverett (1941) measured the macroscopic capillary pressure as a function of saturation for different combinations of fluids and porous media and he observed that capillary pressure can be written as:

$$p_i - p_j = \gamma_{ij}\sqrt{\frac{\phi}{k}}J(S) \qquad (1.8)$$

where ϕ is the porosity and $J(S)$ is the dimensionless capillary pressure, called the Leverett J function. Hence, the capillary pressure at macro scale is a function of porous media properties and fluid properties. Several J functions, which are porous medium specific, have been developed over the years of which the relationships of Brooks and Corey (1966) and van Genuchten (1980) are used most frequently in subsurface models.

During drainage, a certain amount of wetting fluid remains in the soil, also at high capillary pressures. This fluid is referred to as *irreducible* or *residual*. At the pore scale, it is the liquid that remains as disconnected blobs or pendular rings in the pores and as a film wrapped around the soil grains. For a non-wetting fluid, there is a certain minimum pressure needed to displace the wetting fluid. This minimum capillary pressure is referred to as *entry pressure* or as *threshold pressure* and is related to the largest pores of the porous medium under consideration.

$p_c - S$ functions are not unique but subject to *hysteresis*. A non-wetting fluid displacing a wetting fluid has a different $p_c - S$ relationship than a wetting fluid displacing a non-wetting fluid. The first displacement process is referred to as *drainage* and the latter is referred to as *imbibition*. Between these two extreme $p_c - S$ relationships, other (scanning) curves can be found that depend on the drainage and imbibition history. Hysteresis is due to contact angle changes as a function of the direction of displacement. Also variation of the geometry of the pores might cause hysteresis; smaller pores control the regression of wetting fluid and larger pores control the imbibition of the wetting fluid. This implies that a small pore with a spherical bulge in its middle will have different imbibition and drainage saturations for the same capillary pressure. This is also referred to as ink bottle effect. In addition, the contact angle may be different for static and dynamic conditions, which causes differences between $p_c - S$ curves derived under static
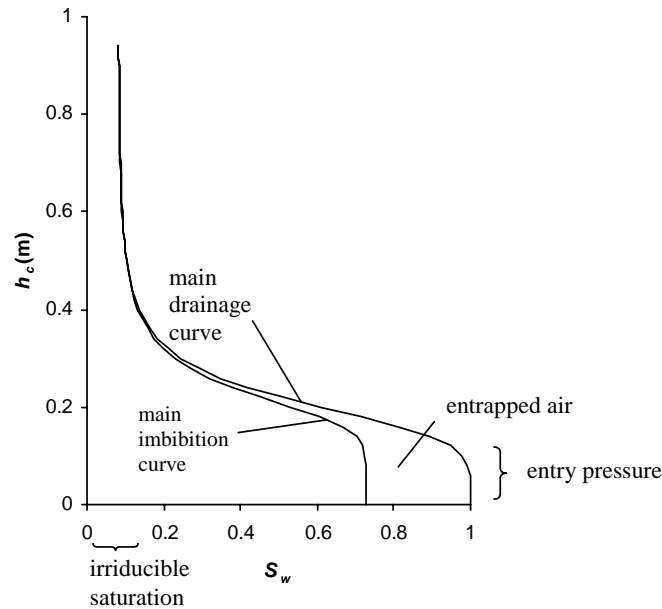
Figure 1.3: Typical two-phase water-air drainage and imbibition relationships between the water-air water-equivalent capillary pressure head, $h_c = p_c^{aw}/\rho_w g$ and the water saturation S_w, including air entrapment.

and dynamic conditions. Understanding the mechanisms that cause differences between drainage and imbibition curves and curves derived under static and dynamic conditions is still subject to research. An overview has been provided by Muccino et al. (1998). Finally, hysteresis may arise owing to non-wetting fluid *entrapment*. For wetting fluid imbibition, part of the non-wetting fluid becomes entrapped, which results in different drainage and imbibition curves. At the pore scale, the non-wetting fluid is immobilized as a result of bypassing mechanisms and snap-off (e.g. Chatzis et al., 1983). Models including hysteresis due to entrapment have been developed by Parker and Lenhard (1987) and Kaluarachchi and Parker (1992). In Figure 1.3 typical (main) drainage and (main) imbibition curves are given for water and air including air entrapment.
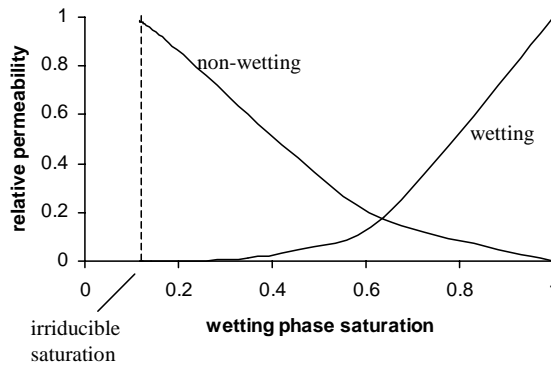
Figure 1.4: Example relative permeability functions for a wetting and a non-wetting fluid in case of drainage

1.2.3 Relative permeability-Saturation relationships

As mentioned in Section 1.2.1, relative permeability is a parameter that lumps all the effects of fluid and solid interaction to the resistivity of flow. This includes capillary forces. Relative permeability is a function of fluid saturation. Burdine (1953) as well as Millington and Quirck (1961) and Mualem (1976) proposed $k_r - S$ relationships for wetting and non-wetting fluids. In this thesis we used the relationships of Mualem (1976). An example of wetting and non-wetting relative permeability curves are given in Fig. 1.4. At residual saturation the relative permeability is equal to zero. Similar to the $p_c - S$ relationships, relative permeability is subject to hysteresis.

1.2.4 Three phases

Two-phase flow is reasonably well understood and can be modeled using the $P_c - S - k_r$ relationships that where discussed above. Three-phase flow is more complicated by the introduction of a third fluid phase into the porous medium. Three-phase flow has a unique and important feature that is not found in two-phase flow. In two-phase flow, one phase will

wet the porous medium more than the other phase. In contrast, for three
phases there will be an intermediate wetting phase which will be positioned
uniquely in the porous medium. Much of the early work on three-phase
flow has been concentrated on developing $p_c - S - k_r$ relationships. Due
to the great difficulty of directly measuring $p_c - S - k_r$ relationships of
three-phase systems, attempts have been made to predict them from two-
phase data. Leverett (1941) proposed to treat three-fluid phase systems
analogous to the two-fluid phase systems. He suggested that in case of two
fluids and one gas phase, the relation between the total liquid saturation
and the interfacial curvature of the gas-liquid interface is independent of
the number of liquids, which together form the total liquid saturation, S_t.
The two liquids are thus assumed to behave as one liquid with respect to
the gas phase. And in addition, the water-NAPL interface is assumed to be
independent of the NAPL-gas interface. Hence, $p_c^{ow} = f(S_w)$; $p_c^{ao} = f(S_t)$
and $p_c^{aw} = p_c^{ao} - p_c^{ow}$. Implicitly, it is presumed that the porous medium is
water-wet and that the NAPL is of intermediate wettability with respect to
water and air and NAPL is found everywhere between air and water. That
is, the NAPL spreads over the water-air interface. A NAPL's tendency to
spread on the water-air interface is expressed by the *Spreading Coefficient*,
given by

$$C_s^{eq} = \gamma_{aw}^e - (\gamma_{ow}^e - \gamma_{ao}^e). \tag{1.9}$$

γ_{ij}^e are the equilibrium interfacial tensions between fluid i and j when a
third phase is present (e refers to thermodynamic equilibrium). NAPLs
that spread between the water and the air and form a film between these
two liquids, results in a C_s^{eq} equal to zero, whereas, NAPLs that exhibit
finite contact angles and that form small lenses in the presence of air and
water, result in a negative C_s^{eq}. For a three-phase system with a negative
spreading coefficient, $p_c^{ao} = f(S_t, S_w)$, since direct contact of air by water
is possible.

An example of the Leverett scaling used in a multi-phase flow model
is given by Lenhard and Parker (1987). Lenhard and Parker introduced
the fluid-pair dependent parameters β_{aw}, β_{ow} and β_{ao} that are defined as
$\beta_{aw} = 1$, $\beta_{ow} = \frac{\gamma_{aw}}{\gamma_{ow}}$ and $\beta_{ao} = \frac{\gamma_{aw}}{\gamma_{ao}}$, in order to scale the $p_c - S$ curves to the
easily measurable water-air curves. The transition between both fluid phase
systems occurs at a certain critical water-NAPL capillary pressure. Above
this capillary pressure no NAPL is found and the distribution of the fluid
phases is given by the water-air capillary pressure and below this capillary
pressure three phases exit in the pore space. In order to avoid discontinuous

jumps between two- and three-phase systems the scaling parameters must fulfill:

$$\frac{1}{\beta_{ow}} + \frac{1}{\beta_{ao}} = \frac{1}{\beta_{aw}} \tag{1.10}$$

which is a direct consequence of Eq.(1.2). This is supposed to be fulfilled for spreading liquids only. We also refer to Stone Stone (1970, 1973) who also used Leverett scaling to derive three-phase constitutive relationships.

1.3 Problem description and objectives

Three-phase flow systems are characterized by the additional presence of the intermediate wetting fluid as compared to two-phase systems. In this section, two issues are introduced that are typical for three-phase flow systems. The first issue is the non-drainable residual NAPL after gravity drainage and the second issue is the effect of heterogeneity on the infiltration of NAPL. From both issues a number of questions arise. The aim of this thesis is to answer these questions.

1.3.1 Non-drainable residual NAPL

The assumption of spreading liquids in multi-phase flow models, puts a constraint to the applicability of these models. Although most NAPLs of environmental concern are spreading liquids, non-spreading liquids can also be found such as higher hydrocarbons (e.g. dodecane) and chlorinated solvents (e.g. PCE and TCE). It is still under discussion whether in a porous medium non-spreading NAPL forms a film/layer between the aqueous and the gas phase or remains as disconnected droplets (Fenwick and Blunt, 1998). Fenwick and Blunt (1998) and Dong et al. (1995) state that non-spreading liquids form a layer between the water and the gas phase, due to the capillary forces that drag the liquid into the edges of the pores. They assume that both types of liquids (spreading and non-spreading) might show similar behavior under predefined conditions (Zhou and Blunt, 1997). Kalaydjian et al. (1993) and Vizika and Lombard (1996) observed different relative permeability curves for spreading and non-spreading liquids, and in addition, a better oil recovery for spreading liquids than for non-spreading liquids. Hofstee et al. (1997) showed experimentally that below certain NAPL saturation or pressure, non-spreading liquids do not comply with the Leverett assumption. Both studies indicate that at macro scale non-spreading liquids behave differently from spreading liquids. Kalaydjian and

Tixier (1991) even state that the spreading coefficient should be included into the three-phase constitutive relationships.

The assumption, that all the intermediate wetting liquids are spreading liquids or behave like spreading liquids, implicitly assumes that there is no residual intermediate wetting fluid after drainage. Residual intermediate wetting liquid is the liquid that remains in the pores after infiltration in the unsaturated zone and downward movement due to capillary forces. We will refer to this residual liquid as *non-drainable residual* liquid. With respect to spreading liquids, non-drainable residual liquid is supposed to be very small, because they form a film. The film always stays connected and, therefore, it drains downward to the water table via film-flow under the influence of gravity until the film has a molecular thickness. Experimentally, however, non-drainable residual NAPL has been observed after gravity drainage (e.g. Mercer and Cohen, 1990; Kantzas et al., 1988; Zhou and Blunt, 1997,). This phenomenon was already recognized by Luckner et al. (1989), Waddill and Parker (1997) and Hofstee et al. (1997) but has to our knowledge never been included into multi-phase flow models. Mercer and Cohen (1990) state that non-drainable residual saturation ranges between 0.006 and 0.5 . In our opinion, the inclusion of non-drainable residual NAPL in subsurface multi-phase flow models, will give improved prediction of NAPL flow, saturation and contaminated areas. The displacement of NAPL under gravity in the presence of water and gas is referred to as gravity drainage in the petroleum industry. This process is similar to the drainage of NAPL towards the water table. The efficiency is determined by the residual NAPL saturation at the end of the drainage process. We observed that there is a slightly different focus between reservoir engineers and geohydrologists studying contaminated sites. With respect to reservoir engineers, a recovery rate of 80% will be remarkable high (Carlson, 1988) and non-drainable residual NAPL can be considered negligible. In contrast, with respect to a NAPL contaminated area, a residual saturation of 2% is a considerable source for dissolved NAPL, and might spoil a large volume of groundwater. This indicates that especially in subsurface models, non-drainable residual NAPL should be included. Until now it is not clear what pore scale phenomena are responsible for residual saturation. Pore scale observations, although they are very informative, have not been able to clarify the pore scale events (Dong et al., 1995; Schwille, 1988; Hayden and Voice, 1993, e.g.).

Non-drainable residual NAPL is the first issue we will address in this

thesis. The objective is to answer the following questions:

- How can non-drainable residual NAPL be accounted for in a macro scale
  constitutive model?

- What would a macro scale constitutive model look like if we include non-
  drainable residual NAPL?

- Can we verify the constitutive model by using an intermediate scale ex-
  perimental set up?

1.3.2 Heterogeneity

As was mentioned before, in a three-phase system there is an intermediate
wetting fluid, whose presence leads to specific three-phase flow behavior.
The intermediate wetting fluid, depending on whether it encounters a wet-
ting phase or a non-wetting phase, can display either non-wetting or wet-
ting behavior with respect to the other fluid phases. This is most noticeable
when heterogeneities are involved.

Heterogeneity or layering of porous media causes obstruction of the
infiltrating velocity of NAPL. Schroth et al. (1998) showed retention of
NAPL above (inclined) interfaces to coarser (water-unsaturated) sand. Il-
langasekare et al. (1995) observed retention above fine and coarse sand
layers, and in addition, 'macro scale' entrapment inside layers. On the
cover of this thesis, an intermediate scale experiment visualizes the effect
of horizontal layers of coarse and fine sand on the redistribution of the infil-
trating NAPL. The sand is unsaturated with water that has a green color.
The NAPL is dyed red. The experiment was conducted at the Norwegian
Geotechnical Institute, Oslo. The resistance against infiltration is due to
permeability reduction and due to the non-linear relationship between sat-
uration and capillary pressure. If the permeability or the porosity changes
between two layers in a porous medium, from Eq.(1.8), it follows that con-
tinuity of capillary pressure forces the fluid saturation to be discontinuous
across the interface between these layers. In turn, this may lead to discon-
tinuities in the relative permeability at the layer interface, as the latter is
a function of the fluid saturation. A strong reduction across a (horizontal)
interface of the relative permeability of a downward infiltrating fluid may
reduce the mobility, which in turn may reduce the fluid velocity across the
interface. This often leads to accumulation of the fluid above the interface.
Hence, heterogeneities in porous media may lead to additional spreading,

and therefore, enlargement of the contaminated area. van Dijke and van der Zee (1998) and de Neef and Molenaar (1997) analytically studied the effect of layers on non-wetting fluid infiltration. However, as far as we know no analysis has been done on the infiltration of intermediate wetting fluid in a three-phase system.

Heterogeneity is the other issue we deal with in this thesis. Our objective is to answer the following questions:

- What effect have inclined layers on the intermediate wetting fluid infiltration and do we understand the role that the intermediate wetting liquid displays with respect to the wetting water and the non-wetting air at the interface?

- Are numerical multi-phase flow models able to mimic the effect of the interaction between layer interfaces and water saturation on the infiltration of NAPL in three-phase systems?

- Can we understand and analytically describe the spreading behavior of infiltrating NAPL above an interface between two layers in a three-phase system?

- What are the main fluid and porous medium parameters that control the spreading of intermediate wetting NAPL above an interface between two layers and what is the role of the capillary pressure and the water pressure in this case?

1.4   Outline

This thesis is organized in five chapters. The aim is to answer the questions that were raised above. We performed laboratory experiments and used numerical and analytical approaches in our studies. All the chapters can be read as self-contained papers.

In Chapters 2 and 3, we consider non-drainable residual NAPL. In Chapter 2, a new constitutive model is introduced that incorporates non-drainable residual NAPL and that is based on a newly developed conceptual pore scale model. In Chapter 3, we give an overview of experimentally measured non-drainable residual NAPL and aim at verification of the constitutive model using a specially developed experimental set up. In Chapters 4 and 5, the effect of heterogeneity on NAPL infiltration is studied. In Chapter 4, we focus on the interaction between (inclined) layers and the position

of the watertable. We develop an experimental model that visualizes the effects of heterogeneities. In addition, the experimental model is used to assess whether the results obtained with the numerical multi-phase flow model, STOMP (White at al., 1995) comply with observations. In Chapter 5, we analyze the DNAPL spreading above the interface between two sandy layers using STOMP and by developing an analytical approximation that provides an estimate for DNAPL pressure, saturation and lateral spreading in the area just above the interface. We verify the accuracy of the analytical approximation by numerical calculations.

References

Abriola, L.M. and Pinder, G.F., 1985. A multiphase approach to the modeling of porous media contamination by organic compounds 2. Numerical simulation. Water Resources Research, 21(1):19–26.

Anderson, G.A., 1986. Wettability literature survey-part 1: Rock/oil/brine interactions and the effects of core handling on wettability. Journal of Petroleum Engineering, October 1986, 1125–1144.

Brooks, R.H. and Corey, A.T.,1966. Properties of porous media affecting fluid flow. Journal of Irrigation and Drainage Division, 92:61–88.

Burdine, N.T., 1953. Relative permeability calculation from size distribution data. Trans AIME, 198, 71–78.

Carlson, 1988. Performance of Hawkins Field Unit under gas drive-pressure maintenance operators and development of an enhanced oil recovery project. Proceedings of the 1988 6th SPE/DOE symposium on enhanced oil recovery, Tulsa, OK, SPE 17324.

Chatzis, I.,Morrow, N.R., Lim, H.T., 1983. Magnitude and detailed structure of residual oil saturation. Society of Petroleum Engineering Journal, April, 311–326.

Darcy, H.P.G., 1856. Exposition et application des principes a suivre et des formules a employer dans les questions de distribution d'eau. Les fontaines publiques de la ville de Dijon. Victor Dalmont, Paris, 590–594.

de Neef, M.J. and Molenaar, J., 1997. Analysis of DNAPL infiltration in a medium with a low permeability lens. Computational Geosciences, 1(2):191–214.

Dong, M., Dullien, F.A.L. and Chatzis, I., 1995. Imbibition of oil in film form over water present in edges of capillaries with an angular cross section. Journal of Colloid and Interface Science, 172:21–36.

Faust, C.R., 1985. Transport of immiscible fluids within and below the unsaturated zone: a numerical model. Water Resources Research, 21(4):587–596.

Fenwick, D.H. and Blunt, M.J., 1993. Three-dimensional modeling of three phase imbibition and drainage. Advances in Water Resources, 21(2):121–143.

Hayden, N.J. and Voice, T.C., 1993. Microscopic observation of a NAPL in a three-fluid-phase soil system. Journal of Contaminant Hydrology, 12:217–226.

Hofstee, C., Dane, J.H. and Hill, W.E., 1997. Three-fluid retention in porous media involving water, PCE and air. Journal of Contaminant Hydrology, 25:235–247.

Illangasekare T.H., Armbruster, E.J. and Yates, D.N., 1995. Non-Aqueous-Phase fluids in heterogeneous aquifers – Experimental study. Journal of Environmental Engineering, 121(8):571–579.

Kalaydjian, F. J.-M. and Tixier, M., 1991 Effect of the spreading coefficient on gas/oil capillary pressure curves in presence of connate water. SCA paper 9106, presented at the 5th Annual Technical Conference of the Society of Core analysts, San Antonio, TX, 1991.

Kalaydjian, F.J.-M., Moulu, J-C, Vizika, O., Munkerud, P.K., 1993. Three-phase flow in water-wet porous media: determination of gas/oil relative permeabilities under various spreading conditions. 68th Annual Technical Conference and Exhibition of the Society of Petroleum Engineers, Houston, TX, SPE 26671.

Kaluarachchi, J.J. and Parker, J.C., 1989. An efficient finite element method for modeling multiphase flow. Water Resources Research, 25(1):293–313.

Kaluarachchi, J.J. and Parker, J.C., 1992. Multiphase flow with a simplified model for oil entrapment. Transport in Porous Media, 7:1–14.

Kantzas, A.,Chatzis, I., Dullien, U., 1988. Enhanced oil recovery by inert gas injection. Proceedings of the 1988 6th SPE/DOE symposium on enhanced oil recovery, Tulsa, OK, SPE 17379.

Lenhard, R.J. and Parker, J.C., 1987a. Measurement and prediction of saturation-pressure relationships in three-phase porous media systems. Journal of Contaminant Hydrology, 1:407–424.

Leverett,   M.C.,   1941.   Capillary   behavior   in   porous   solids. Trans.Am.Inst.Min.Metall.Pet.Eng., 142:152–169.

Luckner, L., van Genuchten, M.Th. and Nielsen, D.R., 1989. A consistent set of parametric models for the two-phase flow of immiscible fluids in the subsurface. Water Resources Research, 25(10):2187–2193.

Mercer, J.W. and Cohen, R.M. A review of immiscible fluids in the subsurface: properties, models, characterization and remediation. Journal of Contaminant Hydrology, 6:107–163.

Millington, R.J. and Quirck, J.P., 1961. Permeability of porous solids. Trans.Faraday Soc., 57, 1200–1206.

Morrow, N.R., 1975. The effects of surface roughness on contact angle with special reference to petroleum recovery. The journal of Canadian Petroleum, Oct-Dec, 42–53.

Mualem, Y., 1976. A new model for predicting the hydraulic conductivity of unsaturated porous media. Water Resources Research, 12(3):513–522.

Muccino, J.C., Gray, W.G., Ferrand, L.A., 1998. Toward an improved understanding of multiphase flow in porous media. Reviews of Geophysics, 36(3): 401–422.

Parker, J.C. and Lenhard, R.J., 1987. A model for hysteretic constitutive relations governing multiphase flow: 1. Saturation-Pressure relations. Water Resources Research, 23 (12), 2187–2196.

Powers, S.E., Anckner, W.H., Seacord, T.F., 1996. Wettability of NAPL-contaminated sands. Journal of Environmental Engineering, October 1996, 889–896.

Schroth, M.H., Istok, J.D. and Selker, J.S., 1998. Three-phase immiscible fluid movement in the vicinity of textural interfaces. Journal of Contaminant Hydrology, 32:1–23.

Schwille, F., 1988. Dense chlorinated solvents in porous and fractured media model experiments. Lewis Publishers, Chelsea, MI.

Stone, H.L., 1970. Probability model for estimating three-phase relative permeability. Journal of Petroleum Technology, February 1970, 214–218.

Stone, H.L., 1973. Estimation of three-phase relative permeability and residual oil data. Journal of Canadian Petroleum Technology, Oct-Dec 1973, 12(4) 53–61.

van Dijke, M.I.J. and van der Zee, S.E.A.T.M., 1998. Modeling of air sparging in a layered soil: Numerical and analytical approximations. Water Resources Research, 34(3):341–353.

van Genuchten, M.Th., 1980. A closed-form equation for predicting the hydraulic conductivity of unsaturated soils. Soil Science Society American Journal, 44:892–898.

Vizika, O. and Lombard, J.-M., 1996. Wettability and spreading: two key parameters in oil recovery with three-phase gravity drainage. Soc.Pet.Eng.Reservoir Eng. (Feb.) 11:54–60.

Waddill, D.A. and Parker, J.C., 1997. Recovery of light, non-aqueous phase liquid from porous media: laboratory experiments and model validation. Journal of Contaminant Hydrology, 27:127–155.

White, M.D., Oostrom, M.,Lenhard, R.J., 1995. Modeling fluid flow and transport in variably saturated porous media with the STOMP simulator: 1.Nonvolatile three-phase model description. Advances in Water Resources, 18: 352–364.

Zheng, J. and Powers, S.E., 1999. Organic bases in NAPLs and their impact on wettability. Journal of Contaminant Hydrology, 39: 161–181.

Zhou, D. and Blunt, M., 1997. Effect of spreading coefficient on the distribution of light non-aqueous phase liquid in the subsurface. Journal of Contaminant Hydrology, 25:1–19.

Chapter 2

A set of constitutive relationships accounting for residual NAPL in the unsaturated zone*

2.1 Introduction

Contamination of groundwater by organic liquids forms a serious treat to subsurface water resources. These liquids have a low miscibility with water and move as a discrete liquid phase. A small part of the liquid may dissolve in water and small concentrations can be hazardous for humans.

Non-Aqueous Phase Liquids (NAPLs), such as gasoline, fuel oils and chlorinated hydrocarbons, may enter the subsurface from a surface spill or a leaking underground pipe or tank. Following a release of sufficient NAPL into the subsurface, NAPL moves through the pores and fractures of the soil due to gravitational and capillary forces. During this migration, the liquid leaves behind blobs or ganglia trapped and immobilized in the pores (non-drainable residual NAPL). If lighter than water, the free and mobile NAPL will drain and finally accumulate in a lens floating on the watertable and, if denser than water, it will penetrate further downward into the aquifer. Increasing the watertable leads to occluded NAPL as the water flows around the NAPL ganglia (entrapment). It is important to quantify the immobilized blobs and ganglia caused by both downward migration and entrapment because they act as a source of dissolved organic components which are gradually released. Multiphase flow models using continuum approaches have been developed to predict flow of fluids in porous media as well as component transport (Abriola and Pinder, 1985; Faust, 1985; Kaluarachchi and Parker, 1992; White et al., 1995). To include effects of immobilized fluid, both non-drainable residual NAPL and entrapped NAPL

must be accounted for in the functional relationships besides saturation, capillary pressure and permeability that are employed in continuum models. A set of functional relationships, also known as a constitutive model, that includes entrapment was developed by Lenhard and Parker (1987b), Parker and Lenhard (1987) and Kaluarachchi and Parker (1992). However, few models have been developed that include non-drainable residual NAPL until now. Waddill and Parker (1997) recognized the two processes that immobilize NAPL. They accounted for non-drainable residual NAPL by assuming a constant residual NAPL saturation. Also Luckner et al. (1989) and Hofstee et al. (1997) suggested constant non-drainable residual NAPL saturations. However, no evidence has been given for this conceptual model.

Laboratory experiments reveal that residual NAPL must not be neglected. A list of non-drainable residual NAPL saturations is given by Mercer and Cohen (1990). The list contains data that are obtained using several different measurement techniques, hence, the values are indicative. Values range between 0.006 and 0.5. The list of residual saturations demonstrates that residual saturation will be higher if a two-phase system is considered (NAPL-air) then if a three-phase system is considered (water-NAPL-air). Another characteristic of non-drainable residual NAPL is that in case of a three-phase system, the non-drainable residual NAPL saturation is strongly negatively correlated to the water saturation (Jarsö et al., 1994; Hoag and Marley, 1986). Furthermore, compared to coarse sand, fine sand has higher residual saturations (Eckberg and Sunada, 1984). Also, liquid properties have impact on the non-drainable residual saturations, as non-spreading liquids appear to be more retained than spreading liquids. A NAPL's tendency to spread on a water -air interface can be measured by the spreading coefficient. The equilibrium spreading coefficient C_s^{eq} is defined as the balance between interfacial tensions:

$$C_s^{eq} = \gamma_{aw}^e - (\gamma_{ow}^e - \gamma_{ao}^e). \tag{2.1}$$

γ_{ij}^e are the equilibrium interfacial tensions between fluid i and j when a third phase is present (the subscript w stands for water, o for NAPL and a for air, e denotes equilibrium which means that the liquids are mutually saturated). If C_s^{eq} is zero, NAPL will spread and form a film on top of the water-air interface. Whereas, if C_s^{eq} is negative, NAPL will exhibit finite contact angles and form small lenses in the presents of air and water. Kalaydjian (1992), Chatzis et al. (1988) and Zhou and Blunt (1997) ob-

served increased retention of non-spreading NAPL in water-NAPL-air systems. This difference in behavior was explained by Chatzis et al. (1988). They suggested that at low saturations spreading NAPLs form a continuous film between the air and water phase, whereas non-spreading NAPLs form disconnected blobs and pendular rings. A NAPL film drains due to gravitational forces, which results in lower residual saturations. Commonly used constitutive models rely on the assumption that in the presence of water and air, NAPLs fully drain due to their spreading behavior. Hence, after a long period, no NAPL remains in the pores. As far as we know, no specific constitutive models have been developed for non-spreading liquids. Because experiments demonstrate non-drainable residual saturations for spreading liquids as well as non-spreading liquids, we argue that non-drainable NAPL saturation should be included in the models. The objective of this work is to develop a three-phase constitutive model consisting of a set of capillary pressure-saturation relationships that accounts for both non-drainable residual NAPL saturation as well as entrapped NAPL saturation. To include non-drainable residual NAPL saturation one should consider that continuum models imply that one point in space is occupied simultaneously by the fluids water, NAPL and air and the solid phase of the porous medium. This is due to local averaging over a representative volume. Hence, smaller scale physics is reflected only in the functional relationships used in continuum models. To obtain non-drainable residual NAPL saturation at the 'continuum' scale, we first extended the concept of the NAPL behavior at the pore scale. Based on this pore scale behavior, constitutive relationships are reformulated.

To evaluate the accuracy of the residual model, we performed example calculations. In addition, we compared the output of the model with experimental data of Hofstee et al. (1997), who conducted column experiments with PCE, water and air.

2.2   Basics of constitutive model

In this section the model of Parker and Lenhard (1987) and Parker et al. (1987), used as a basis for our constitutive model, is discussed including entrapment. Similar to Parker and Lenhard (1987) in the following we refer to NAPL as oil and the gas phase as air.

2.2.1   Saturation-capillary pressure relations and scaling

In the constitutive model we distinguish between water saturation (S_w), oil saturation (S_o), air saturation (S_a) and total liquid saturation (S_t). S_t is defined as $S_w + S_o$ and S_a is equal to $1 - S_t$. Effective water and total liquid saturations are:

$$\overline{S}_w = \frac{S_w - S_m}{1 - S_m}, \tag{2.2}$$

$$\overline{S}_t = \frac{S_t - S_m}{1 - S_m}, \tag{2.3}$$

where S_m is the minimum or residual water saturation. S_m is assumed to be independent of fluid properties or saturation history. Effective oil saturation is defined as $\overline{S}_o = \overline{S}_t - \overline{S}_w$ and effective air saturation as $\overline{S}_a = 1 - \overline{S}_t$.

The $P_c - S$ relations are described by scaled variants of the empirical saturation-capillary head function of van Genuchten (1980). For the 2-phase air-water system applies

$$\overline{S}_w = \left[1 + (\alpha h_{aw})^n\right]^{-m}, \tag{2.4}$$

where α and n are porous medium parameters, $m = 1 - 1/n$, and $h_{aw} = h_a - h_w$ is the air-water capillary head. The air saturation is given by $\overline{S}_a = 1 - \overline{S}_w$. If $h_{aw} \leq 0$, $S_w = 1$. The three-phase air-oil-water system is defined by

$$\overline{S}_w = \left[1 + (\alpha \beta_{ow} h_{ow})^n\right]^{-m} \tag{2.5}$$

together with

$$\overline{S}_t = \left[1 + (\alpha \beta_{ao} h_{ao})^n\right]^{-m}. \tag{2.6}$$

The air saturation is given by $\overline{S}_a = 1 - \overline{S}_t$. $h_{ow} = h_o - h_w$ and $h_{ao} = h_a - h_o$ are the oil-water and air-oil capillary heads in which h_w, h_o and h_a are respectively the water, oil and air water equivalent pressure heads ($h_i = \frac{P_i}{\rho_w g}, i = w, o, a$ and P_i is the pressure of the phase i). If $h_{ow} \leq 0$ $S_w = 1$ and if $h_{ao} \leq 0$ $S_t = 1$. β_{ao} and β_{ow} are the scaling coefficients that relate respectively the air-oil function and the oil-water function to the air-water function.

Application of two sets of two-phase relationships was first suggested by Leverett (1941). Leverett assumed that the total liquid saturation in a multiphase system is only a function of the curvature of the gas-liquid interface. This assumption is only valid if the wetting fluid is separated
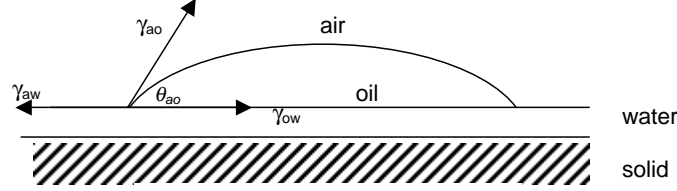
Figure 2.1: Oil lens on a water film that is that coats a solid surface (after McBride et al.,1992).

from the non-wetting fluid by the intermediate wetting fluid. Implicitly, it is assumed that water is the most wetting fluid, followed by oil and air and that there is an oil film in between water and air. Based on Leverett's assumption we can simplify the complicated interaction between three phases by separation of the fluid system in two fluid-relationships. One, the $P_c - S$ relationship between oil and air and two, the $P_c - S$ relationship between water and oil.

The scaling coefficients, β_{ao} and β_{ow}, are given by:

$$\beta_{ow} = \frac{\gamma_{aw}}{\gamma_{ow}}, \quad \beta_{ao} = \frac{\gamma_{aw}}{\gamma_{ao} \cos \theta_{ao}} \quad \text{and} \quad \cos \theta_{ao} = \frac{\gamma_{aw} - \gamma_{ow}}{\gamma_{ao}}, \qquad (2.7)$$

where γ_{ij} are the interfacial tensions between fluid i and j. θ_{ao} is the contact angle between the oil-air interface and a water film that coats the solid surface (see Fig.2.1).

2.2.2 Phase transitions

To prevent numerical instabilities, the effective water saturation is larger than zero in multiphase flow models. This restriction imposes that the water saturation must be equal to or larger than the residual water saturation. In other words, multiphase flow models deal with either a two-phase air-water system or a three-phase air-oil-water system. A change from a three-phase system to a two-phase system will take place if $\overline{S}_t$ decreases to

$\overline{S}_w$. A critical oil pressure head, h_o^c, conditions the transition from three phases to two phases and back:

$$h_o^c = \frac{\beta_{ao}h_a + \beta_{ow}h_w}{\beta_{ow} + \beta_{ao}}. \qquad (2.8)$$

If $h_o < h_o^c$, the system will consist of two phases, whereas if $h_o > h_o^c$ the system will consist of three phases. To avoid discontinuous jumps in the saturations for $h_o = h_o^c$, the three-phase water saturation has to be equal to the two-phase water saturation. Hence, $\overline{S}_t(h_{ao}) = \overline{S}_w(h_{ow}) = \overline{S}_w(h_{aw})$, and therefore, $\beta_{ao}h_{ao} = \beta_{ow}h_{ow} = \beta_{aw}h_{aw}$, where β_{aw} is equal to one. Under static conditions $h_{aw} = h_{ao} + h_{ow}$. Then, we obtain from Eq.(2.5) and (2.6) the constraint (see also Lenhard and Parker, 1987a):

$$\frac{1}{\beta_{ao}} + \frac{1}{\beta_{ow}} = 1. \qquad (2.9)$$

Note that if the scaling coefficients are defined as in Eq. (2.7), this condition will be satisfied for non-spreading liquids as well as spreading liquids.

2.2.3 Entrapment

The non-wetting phase (oil, air) can become occluded by the wetting phase (water) during imbibition by various mechanisms, e.g., bypassing, snap-off, etc. This results in non-wetting phase entrapment. Air entrapment is disregarded. Entrapped oil depends both on the historical minimum water saturation (start of the entrapment) and on the maximum oil that can become entrapped. The latter value is related to the soil and fluid properties.

We employ the model for oil entrapment of Kaluarachchi and Parker (1992). In order to include oil entrapment, the effective oil saturation is divided in the fractions free oil ($\overline{S}_{of}$) and trapped oil ($\overline{S}_{ot}$). Furthermore, the sum of the effective water saturation and the effective trapped oil saturation is defined as the apparent water saturation ($\overline{S}_{wa}$). Where oil is present, it can be entrapped according to:

$$\overline{S}_{ot} = \begin{cases} \frac{1-\overline{S}_w^{\min}}{1+L_n(1-\overline{S}_w^{\min})} - \frac{1-\overline{S}_{wa}}{1+L_n(1-\overline{S}_{wa})} & \text{for } \overline{S}_{wa} > \overline{S}_w^{\min} \\ 0 & \text{for } \overline{S}_{wa} = \overline{S}_w^{\min}, \end{cases} \qquad (2.10)$$

where $\overline{S}_w^{\min}$ is the minimum historical water saturation and L_n is the Lands factor (Land, 1968):

$$L_n = \frac{1}{\overline{S}_{ot}^{\max}} - 1. \tag{2.11}$$

$\overline{S}_{ot}^{max}$ is the maximum effective trapped oil saturation. We refer to Kaluarachchi and Parker (1992) for detailed explanation of the employed equations.

2.3 Residual constitutive model

2.3.1 Pore scale three-phase fluid distribution

Fluid flow calculations at the microscale have been reported for various pore geometries in order to define and understand continuum scale behavior. Bear (1972) performed calculations for an ensemble of capillaries. Also triangularly and rectangularly shaped pores have been used to explain macro scale observations (Dong et al., 1995; Fenwick and Blunt, 1998). Pore networks consisting of a lattice of pores and throats have been developed and used to scale up the local scale fluid behavior (see for review Ferrand et al. (1990) and Celia et al. (1995)). To define pore scale mechanisms that cause non-drainable residual oil, we choose to represent the porous medium by a ensemble of spheres. The qualitative behavior of the sphere model can be extended to a randomly distributed porous medium consisting of grains. By applying physical and chemical laws to this configuration we identify a mechanism that causes non-drainable residual oil. Whereas we do not suggest that it is the only possible mechanism, it is a plausible one and useful to develop our constitutive residual oil model.

Let us consider a porous medium that consists of packed uniform nonporous spheres of which in the horizontal direction the centers are situated at an angle of $60°$ to each other and in the vertical direction on top of each other. Hence, each sphere has 8 contact points. The spheres are strongly water-wet. Water is the most wettable fluid, then oil and finally gas. Water is at residual saturation. Therefore, a thin layer of water spreads over the sphere surfaces and a capillary ring of water is wrapped around the contact points of the spheres. We add non-spreading oil and allow the oil to drain. Because the interfacial tension at the water-air interface is higher than the water-oil interface, a small volume of water drains from the pendular rings. After drainage, intermediate wetting oil rings are situated around
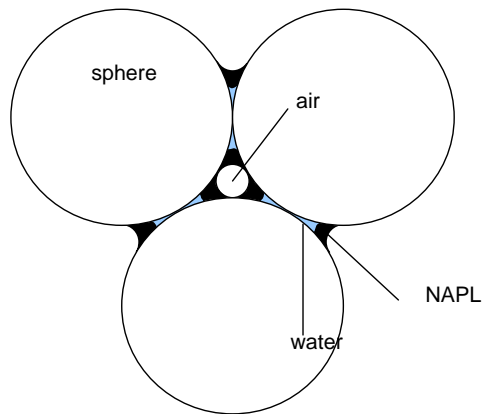
Figure 2.2: Configuration of spheres and fluids just before the oil rings disconnect.

the water rings due to interfacial forces. We assume a non-zero contact angle. Accordingly, these oil rings are not connected to each other (see Fig.2.2). Only an excess of oil can cause the rings to form interconnecting bridges. The oil that is maintained in the pendular rings is considered as the non-drainable residual oil. Hayden and Voice (1993) observed at the microscale these double pendular rings of water and oil around the contact points of sand grains as well as the water film around the grains. However, they could not determine whether an oil film connected the pendular oil rings or not.

We calculated quantitatively the volume that is occupied by the liquid in the pendular rings. The calculations (Appendix A) show that the spreading behavior of the oil controls the total volume of liquid that is retained in the pendular rings. The less spreading the oil, the higher is the volume that is retained. This behavior has also been observed in experiments by Chatzis et al. (1988) and Zhou and Blunt (1997).

Under oil drainage conditions the column of spheres retains residual water and oil in pendular rings. Imbibing oil reconnects the pendular rings and, therefore, cancels the residual oil configuration. With respect to water drainage, the retained water decreases but the total volume of retained oil

remains unchanged. After all, there is no available source of oil to fill up the void that is left by the retracting water. In case of water imbibition, the water volume grows and because water is the wetting fluid it grows within the rings around the contact points. This means that water pushes the oil ring away from the contact points of the spheres until the oil ring connects to the other oil rings. Because of capillary forces, the oil refills the void in between the three spheres and therefore, the oil remobilizes. This negative correlation between non-drainable residual oil saturation and the water saturation has also been found by Jarsjö et al. (1994) in their kerosene experiments. Also Dong et al. (1995) showed for etched glass plates similar behavior of imbibing non-spreading oil (connected oil).

We now extend the qualitative behavior to a random distribution of grains. The volume of both water and oil that is retained in the pendular rings can be defined as a threshold or critical volume. If the total liquid volume drops below this critical volume, oil will become disconnected. Hence, non-drainable residual oil is the oil that will be retained if the total liquid volume has dropped below the critical volume. The non-drainable residual oil volume is controlled by both the spreading coefficient that affects the maximum total volume of non-drainable residual liquid and the water saturation together with the history of the fluid system. The latter two both affect the balance between water and oil if oil is at residual saturation.

2.3.2   Transition to the 'continuum' scale

In agreement with the pore scale definition of non-drainable residual oil we define a non-drainable residual oil saturation (S_{or}) at the 'continuum' scale to correspond with the oil volume that will remain in the porous medium if the total liquid volume drops below a critical volume. The critical total liquid volume divided by the pore volume is the critical total liquid saturation (S_t^c). According to our pore scale model fluid properties and porous medium geometry determine this critical total liquid saturation. Hence, for each combination of fluids and porous medium a unique critical total liquid saturation can be found. The critical total liquid saturation will turn out to be the only extra parameter needed in our residual oil constitutive model in comparison to the model of Parker et al. (1987).

Similar to the critical oil pressure head defined in Eq.(2.8) a critical pressure head defines the transition to the non-drainable residual oil system. Substitution of the (effective) critical total liquid saturation $\overline{S}_t^c$ into the
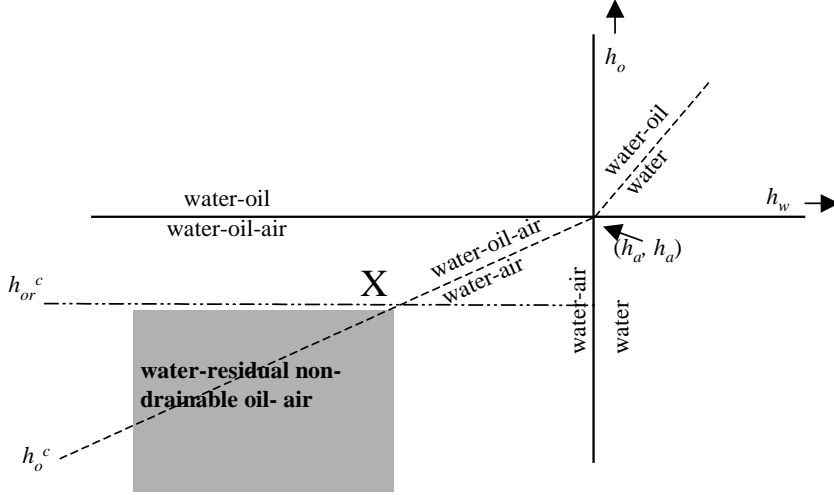
Figure 2.3: $h_w - h_o$ field. The critical pressure heads are indicated as well as the existing phases for each part of the field. X is the intersection of the h_{or}^c line and the h_o^c line at (h_a, h_a). Residual non-drainable oil will only occur when both h_o has dropped below h_{or}^c and oil is available.

capillary pressure head-saturation relation of Eq.(2.6) yields:

$$h_{or}^c = -\frac{1}{\alpha \beta_{ao}} \left[(\overline{S}_t^c)^{\frac{-1}{m}} - 1 \right]^{\frac{1}{n}} + h_a. \tag{2.12}$$

h_{or}^c is the critical oil pressure head for non-drainable residual oil. If $\overline{S}_t^c$ approaches zero, h_{or}^c will become minus infinity and there will be no non-drainable residual oil. If $\overline{S}_t^c$ approaches one, h_{or}^c will increase to h_a which implies that as soon as the porous medium becomes unsaturated ($h_o < h_a$), oil will become also residual ($h_o < h_{or}^c$). Note that we use effective saturations similar to the basic constitutive model as we assume that the residual water saturation remains unaffected by the non-drainable residual oil.

Consequently, two critical oil pressure heads control two transitions in the residual constitutive set of $P_c - S$ relationships. h_o^c controls the

transition from two phases to three phases and vice versa, whereas h_{or}^c controls the transition from free oil saturation to non-drainable residual oil saturation. From the definitions in Section 2.2.1 follows that $h_o = h_a$ controls also a transition: air is or is not present. For illustration consider Fig. 2.3 that shows a plot that is formed by the two perpendicular axes h_w and h_o and that intersect at (h_a, h_a). The critical pressure heads h_o^c and h_{or}^c are indicated in the figure. Note that these critical pressure heads only make sense in the unsaturated zone (lower left quadrant). The phases that exist in each quadrant subsection are indicated too. Lines define the transitions between the composition of phases. In the unsaturated zone, three fluid systems are distinguished, i.e., the three-phase (water-oil-air) system, the two-phase (water-air) system and the non-drainable residual oil (water-non-drainable residual oil-air) system. Non-drainable residual oil only will appear if h_o decreases below h_{or}^c and oil is available. Hence, in the figure, this will occur when the h_{or}^c-line borders the shaded field. In other words, non-drainable residual oil is formed if three conditions are fulfilled:

1. $h_o < h_a$ (unsaturated zone), and

2. $h_o < h_{or}^c$ (residual oil), and

3. $h_o^c < h_{or}^c$ (oil is available).

Non-drainable residual oil can only be formed in case of drainage. Imbibition implicitly assumes connected pendular rings which implies mobile, free oil.

In the following section, we define the set of $P_c - S$ relationships for the non-drainable residual oil system. To obtain a consistent set of $P_c - S$ relationships, the non-drainable residual oil system is defined in such a way that is compatible with the model of Parker et al. (1987).

2.3.3   The non-drainable residual oil system

We presume that the three-phase non-drainable residual oil system can be represented by two two-phase saturation pressure curves. However, whereas Parker and Lenhard developed two independent saturation curves, i.e. for the water saturation and for the total liquid saturation, in case of non-drainable residual oil these curves are not independent. At non-drainable residual oil saturation, the total liquid saturation depends not only on the

gas-oil interface but also on the gas-water interface and the water satura-
tion depends on both the gas-water interface and the oil-water interface.
Furthermore, because at the pore scale oil is separated in pendular rings,
a continuous oil pressure for the entire system does not exist anymore. We
introduce a new parameter that we refer to as the residual oil pressure
head (h_{or}). This parameter should smoothly connect the non-drainable
residual oil system to the original two-and three-phase systems of capillary
pressure-saturation relations.

In the non-drainable residual oil system, we use the same type of for-
mulation for the (effective) total liquid saturation and the (effective) water
saturation as in Section 2.2, i.e. Eq.(2.5) and (2.6). The difference be-
tween these saturations in this system is defined as the (eff.) non-drainable
residual oil saturation:

$$\overline{S}_{or} = \overline{S}_t - \overline{S}_w. \tag{2.13}$$

Substitution of the oil pressure head by the residual oil pressure head in
Eq.(2.5) and (2.6) yields for the water saturation:

$$\overline{S}_w = [1 + (\alpha\beta_{ow}(h_{or} - h_w))^n]^{-m} \tag{2.14}$$

and for the total liquid saturation:

$$\overline{S}_t = [1 + (\alpha\beta_{ao}(h_a - h_{or}))^n]^{-m}. \tag{2.15}$$

In the constitutive model of Section 2.2 (Eq.(2.5) and (2.6)) the oil pressure
head, h_o, is given and, therefore, the set of equations can be solved. Instead,
Eq.(2.13) to (2.15) can only be solved because the residual oil saturation,
$\overline{S}_{or}$, is known. This is because h_{or} is unknown. $\overline{S}_{or}$ depends both on h_w
when h_o has dropped below h_{or}^c (drainage) and on the events that occur
afterwards. The decrease of h_o below h_{or}^c coincides in the pore model with
the disconnection of the oil rings. Then, drainage or imbibition of water
and oil each lead to different patterns of capillary pressures and saturations.

The non-drainable residual oil saturation that belongs to the discon-
nection of the oil rings, we refer to as the initial non-drainable residual
oil saturation ($\overline{S}_{or}^{ini}$). Accordingly, $\overline{S}_{or}^{ini}$ is the non-drainable residual oil
saturation that belongs to the situation when h_o just has decreased below
h_{or}^c:

$$\overline{S}_{or}^{ini} = \overline{S}_t(h_{or}^c, h_a) - \overline{S}_w(h_{or}, h_w), \tag{2.16}$$

where the water saturation is defined as:

$$\overline{S}_w = [1 + (\alpha\beta_{ow}(h_{or}^c - h_w))^n]^{-m}. \tag{2.17}$$
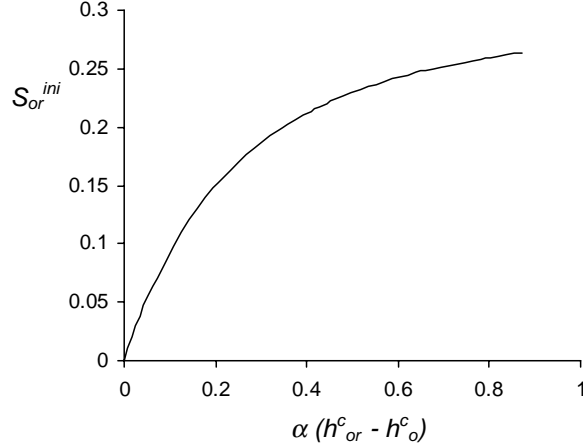
Figure 2.4: $\overline{S}_{or}^{ini}$ dependency on the difference between h_o^c and h_{or}^c normalized by α which represents the capillarity of a porous medium. For $\overline{S}_t^c = 0.3$, $\beta_{ow} = 1.8$, $\beta_{ao} = 2.25$ and $n = 3$, $\overline{S}_{or}^{ini}$ is given for an increasing distance between h_o^c and h_{or}^c. $\overline{S}_{or}^{ini}$ is zero when h_o^c is equal to h_{or}^c and increases asymptotically to $\overline{S}_t^c$ (=0.3).

Rewriting of Eq.(2.8) and substitution into Eq.(2.17) gives:

$$\overline{S}_w = \left[1 + \left(\alpha\beta_{ow}(h_{or}^c - \frac{\beta_{ow} + \beta_{ao}}{\beta_{ow}} h_o^c) \right)^n \right]^{-m} \qquad (2.18)$$

and the total liquid saturation is:

$$\overline{S}_t^c = [1 + (\alpha\beta_{ao}(h_a - h_{or}^c))^n]^{-m}. \qquad (2.19)$$

If we assume that h_a is constant at atmospheric pressure, from Eq.(2.18) and Eq.(2.19) a unique $\overline{S}_{or}^{ini}$ can be calculated for every combination of critical pressure heads. In addition, it follows from the pore scale model that $\overline{S}_{or}$ never exceeds $\overline{S}_{or}^{ini}$. That implies that $\overline{S}_{or}^{ini}$ is the maximum amount of non-drainable residual oil for a specific combination of critical oil pressure heads. Some features of the initial non-drainable residual saturation are shown in Figs.2.4 and 2.5. In Fig. 2.4, $\overline{S}_{or}^{ini}$ is given for an increasing difference between h_o^c and h_{or}^c (normalized by α). This difference may vary between zero and infinity, which depends of the location of the watertable in
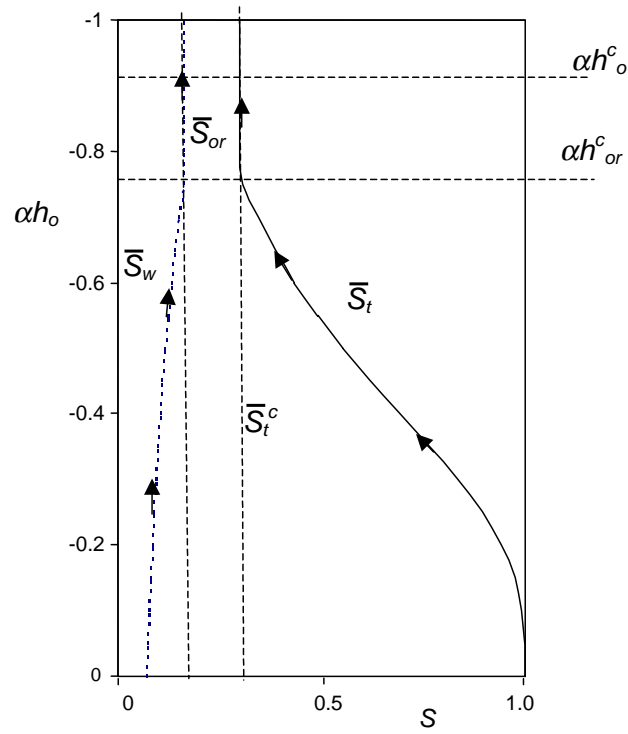
Figure 2.5: Development of the water saturation and the total liquid saturation when h_o normalized by α that represents the effect of capillarity, decreases. For $h_w = 2.1$, $\overline{S}_t^c = 0.3$, $\beta_{ow} = 1.8$, $\beta_{ao} = 2.25$ and $n = 3$ the oil pressure head (h_o) is decreased. When $\overline{S}_t$ decreases below $\overline{S}_t^c$, oil becomes residual (if so $h_o < h_{or}^c$). $\overline{S}_{or}$ would be larger when the difference between $\overline{S}_t^c$ and $\overline{S}_w$ would be larger.
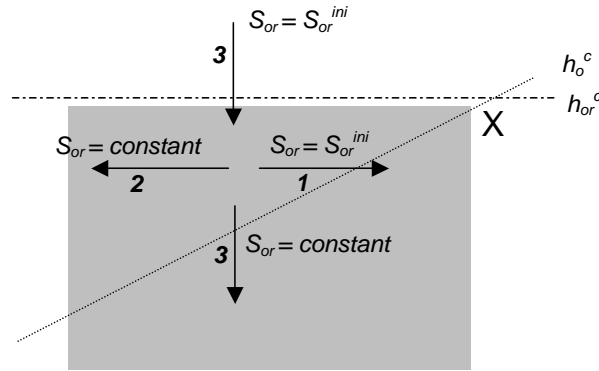
Figure 2.6: Enlargement of the $h_w - h_o$ field. X is the intersection of the h_{or}^c line and the h_o^c line and the shaded box indicate residual oil. The response of S_{or} is given for three events that correspond to the events in Table 2.1 (the event number is indicated).

nr.	Event	Pore scale effect	Effects S_{or}
1	Increase of the water pressure head.	Water pushes oil out of the area around the contact points.	S_{or} equal to $\overline{S}_{or}^{ini}$
2	Decrease of the water pressure head.	Thrinking of both rings, volume of oil remains constant.	S_{or} constant
3	Decrease of the oil pressure head.	No effect on the pendular rings.	S_{or} constant
4	Increase of the oil pressure head.	Imbibition: oil rings will reconnect.	Back to three phase system when $h_o > h_{or}$

Table 2.1: Events and effects on the residual oil saturation at the pore scale and at the macroscale.

reference to the considered location. For a certain constant water pressure head, h_w, and residual non-spreading total liquid saturation, $\overline{S}_t^c$, in Fig. 2.5 the paths followed by $\overline{S}_w$ and $\overline{S}_t$ are drawn when h_o decreases below h_{or}^c. h_w and $\overline{S}_t^c$ define h_o^c and h_{or}^c, respectively. When h_o decreases below h_{or}^c, oil becomes residual.

When oil becomes residual, the residual oil saturation is equal to $\overline{S}_{or}^{ini}$. Then, four events can take place. In Table 2.1, these events are given together with the pore scale effects that correspond to these events and the consequences for $\overline{S}_{or}$ (for static equilibrium conditions). The first three events are also indicated in Fig. 2.6, which is an enlargement of the residual subsection of the $h_w - h_o$-field (Fig. 3). For each arrow the corresponding event number is indicated. For the first event where h_w increases, the oil rings reconnect and the oil resumes to flow. After a while, the oil flow stops as it has become disconnected again and $\overline{S}_{or} = \overline{S}_{or}^{ini}$. For the second and the third event, when either the water or oil pressure head decreases, the residual oil remains constant. This implies that $\overline{S}_{or}$ equals $\overline{S}_{or}^{ini}$ that is characterized by the initial combination of critical pressure heads. $\overline{S}_{or}^{ini}$ is not characterized by the new combination of critical pressure heads belonging to the path that is followed in the $h_w - h_o$-field. For the fourth event, the situation is more complex, which will be explained below. From the definitions for residual oil (Eq.(2.13) to (2.15)) follows that h_{or} is directly related to the volume of residual oil that remains in the soil. Hence, $\overline{S}_{or}$ remains constant until (a) the real oil pressure head equals the residual pressure head. Then, (b) the volume of residual oil is equal to the volume of oil that belongs to the original three-phase system and (c) a transition to the normal three-phase system occurs.

As $\overline{S}_{or}$ is known, we are able to solve the system of equations. h_{or} can be determined iteratively from Eq.(2.13) to (2.15). Note that h_{or} depends on the residual oil saturation ($\overline{S}_{or}$) and is independent of the real oil pressure head (h_o). $\overline{S}_{or}$ is known from $\overline{S}_{or}^{ini}$ (Eq.(2.16)) together with the paths indicated in Table 2.1. Hence, the difference between $\overline{S}_t$ (Eq(2.14)) and $\overline{S}_w$ (Eq.(2.15)) is known from which h_{or} can be calculated iteratively. The result is that h_{or} is smaller than h_{or}^c but larger than h_o^c. At oil drainage conditions h_{or} is always smaller than h_o.

Of the four events we mentioned above, two cause a transition from the non-drainable residual oil system to the other systems (nr. 1 and 4). Continuity of the saturations at the transitions is guaranteed. If the h_w increases (event 1), a transition to the two-phase system will occur as soon

as h_{or} crosses the h_o^c line. As h_{or} never exceeds h_o^c and never decreases below h_{or}^c, h_{or} changes towards the intersection of h_o^c and h_{or}^c. If h_{or} reaches the intersection, then, $\overline{S}_{or}$ will be equal to $\overline{S}_{or}^{ini}$ and $\overline{S}_{or}^{ini} = 0$. Hence, only the two phases water and air will exist. If h_o increases (event 4), a transition to the three-phase system may occur. If h_o equals h_{or}, the system will turn from a residual three-phase system to a normal three-phase system and $\overline{S}_{or} = \overline{S}_o$.

2.3.4   Entrapment

Until now we did not mention entrapment in the residual oil system. When entrapment is included, the determination of the free oil saturation, the trapped oil saturation, the residual oil saturation and the water saturation is very similar to what we presented in Section 2.2.3. The definitions and model development of Kaluarachchi and Parker (1992) can be used easily, also in the residual oil system. Again, the sum of the effective water saturation and the effective trapped oil saturation is defined as the apparent water saturation ($\overline{S}_{wa}$). However, one should consider that oil can only become entrapped in case of imbibition of the aqueous phase when oil is available in the free form or as residual oil. Moreover, oil can only become residual in case of drainage of the oil phase and when oil is available in the free form or as entrapped oil.

In App. B the procedure to calculate the whole set of $P_c - S$ relations are given for the three-phase, the two-phase and the residual system.

2.4   Example calculations

In this section example calculations are presented based on the residual constitutive model. In the first example we show the response of three fluid phases in a porous medium to a decreasing oil pressure (oil drainage). In the second example we focus on the interaction between residual oil and entrapped oil (oil drainage and water imbibition). The model consists of a sequence of static capillary pressure and saturation relationships including non-drainable residual oil, hence it does not account for flow of fluids. The domain is a 1.4 m vertical soil column. Soil and fluid properties used in the simulations are given in Table 2.2. The soil properties have been chosen arbitrary. Coarser or finer sand would have given similar qualitative behavior. We recommend, however, extensive measurement of S_t^c for various sand types and fluid combinations.

Property	Example 1	Example 2
S_m	0	0
n	3	3
α [m^{-1}]	1	1
β_{ow}	1.8	1.8
β_{ao}	2.25	2.25
ρ_o	0.8	0.8
S_{ot}^{max}	0	0.5
S_t^c	0.3	0.45

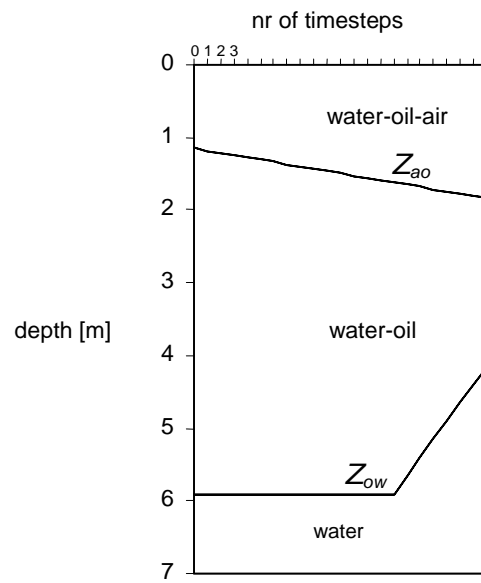**Table 2.2:** Soil and fluid properties

Figure 2.7: Fluid tables below the soil surface for a sequence of timesteps for example 2.

The model responds to variations in water and oil pressure heads in time. Each timestep, small changes in h_o and h_w are imposed to simulate fluid flow. We define the air-oil table (Z_{ao}) as the depth below soil surface where air and oil pressures are equal and the oil-water table (Z_{ow}) as the depth below surface where the oil and water pressures are equal. In example 1 we kept Z_{ow} constant at a level of 4.5 m below the soil surface and decreased Z_{ao} from the top of the column to 50 cm below, i.e. oil is drained by air. In example 2 we decreased Z_{ao} as well but then, after a few sequential timesteps, we started to increase Z_{ow} (imbition of water, see Fig. 2.7).

In Fig. 2.8 final liquid saturations are given for example 1. z is the depth of the column starting from the top. For comparison the results are shown of both our residual oil model and the model of Parker et al. (1987). The reference model shows a decrease of the total liquid saturation from the bottom of the column to the soil surface. The water saturation is more or less constant. Near the soil surface the oil saturation is zero (two-phase air-water system) because the oil pressure head is lower than the critical oil pressure head, h_o^c. Preceding fluid configurations do not affect the final fluid configuration. For the residual oil model, as soon as the oil pressure head decreases below the critical non-drainable residual value (h_{or}^c), non-drainable residual oil is formed. At the start of the simulation, non-drainable residual oil is formed at the top of the column. Later, when the oil pressure head decreases non-drainable residual oil is formed down to $z = 0.55$ m. Instead of the reference model, the final fluid configuration is history dependent. The water saturation in the residual oil model is much lower than in the reference model, whereas, the total liquid saturation is much higher. In between these saturations the non-drainable residual oil resides. Furthermore, non-drainable residual saturation possesses a smooth transition from residual oil saturation to non-residual oil saturation. This behavior corresponds with observations done by Eckberg and Sunada (1984), who studied drainage of oil in a column experiment. The oil drainage curve of the experiment is similar to Fig. 2.8.

In Fig. 2.9 the final liquid saturations are given for example 2. Similar to example 1, the results are shown for the residual model as well as the reference model of Parker et al. (1987) including entrapment. For the reference model, the total liquid saturation decreases from the bottom of the column to the soil surface. At $z = 0.6$ m, all free oil has disappeared and only entrapped oil remains. Again, the residual oil model shows distinct

Figure 2.8: Final saturations for example 1 resulting from the reference model of Parker et al. (1987) which is indicated by a dashed line and from the non-drainable residual model which is indicated by a solid line. Soil and fluid properties are given in Table 2.2.
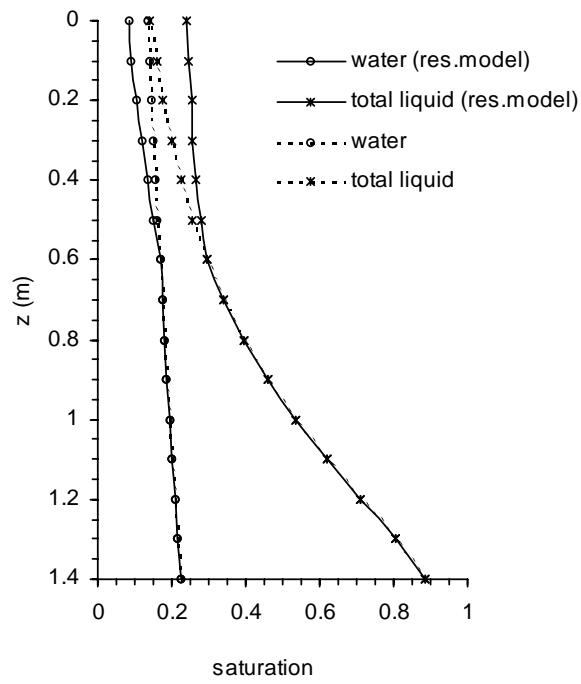
Figure 2.9: Final saturations for example 2 resulting from the reference model of Parker et al. (1987) which is indicated by a dashed line and from the non-drainable residual model which is indicated by a solid line. Soil and fluid properties are given in Table 2.2.
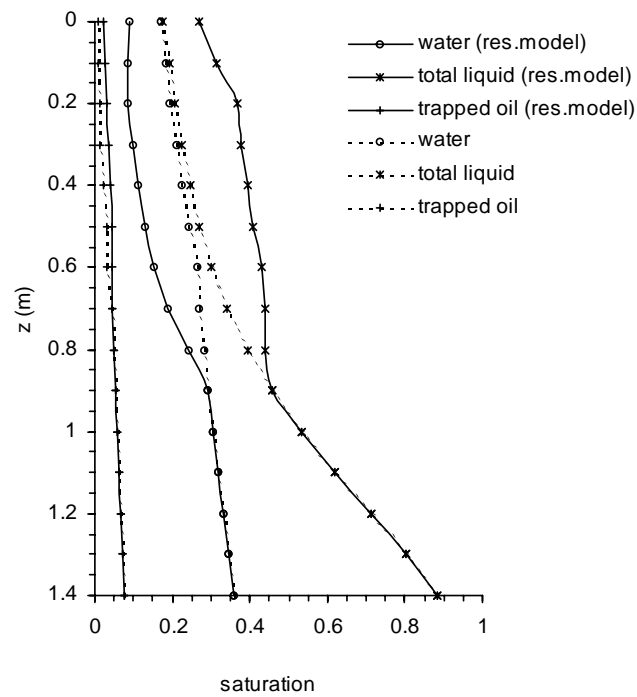
behavior. Above $z = 0.9$ m, S_t is smaller than S_t^c. This means that $h_o < h_{or}^c$ (Eq.(2.12)). Hence, above $z = 0.9$ m the oil is residual.

At the altitude where non-drainable residual oil resides entrapped oil is observed for both the reference model as well as the residual model. The oil has become entrapped by the imbibing water. However, in the residual model more oil is trapped than in the reference model, as the total available oil, i.e. free oil as well as non-drainable residual oil, can become entrapped.

2.5   Comparison with experimental data

Hofstee et al.(1997) performed a three fluid drainage experiment and measured retention curves of water, the dense NAPL perchloroethylene (PCE) and air in a column. PCE has a negative spreading coefficient of -0.0047 Nm^{-1}. Respectively, the interfacial tensions γ_{ow}, γ_{aw} and γ_{ao} are 0.0327 Nm^{-1}, 0.072 Nm^{-1} and 0.044 Nm^{-1} (PCE is denoted with the subscript o).

A 1.0 m sand column was initially filled with water and drained. After drainage, PCE was imbibed from the bottom of the column. Finally, air was allowed to enter the column by gradually decreasing the combined water-PCE pressure at the bottom of the column using an overflow. For each interval, after equilibrium had settled, water and PCE saturations where measured at different heights in the column. The PCE water-equivalent pressure head was defined as:

$$h_o = \rho_o z, \tag{2.20}$$

where z [m] is the difference in elevation between the water-PCE overflow and the location of measurement and ρ_o is the specific density of PCE [-]. This definition, that was also applied by Hofstee et al., implicitly assumes that PCE is a continuous liquid and, therefore, not residual. The capillary pressure head is defined as $h_{oa} = h_a - h_o$. Air is assumed to be the passive phase, therefore, the air pressure head (h_a) is set to zero. Hence, $h_{oa} = -h_o$.

We simulate the experiment with our residual model using the parameters measured in the two phase PCE-air drainage experiment that is presented by Hofstee et al.(1997): The effective porosity is 0.339 [-], α is 3.192 [m^{-1}] and n is 6.88 [-]. Although we could have chosen any point in the column, we choose to verify the residual oil model on the measurements that were done at 0.68 m above the bottom of the column. The few parameters that were not measured are chosen in such a way that a good (visual)

calibration to the experimental data is obtained; $S_m(\text{water})$ is chosen equal to the minimum measured water saturation (0.23) and effective critical total liquid saturation $\overline{S}_t^c$ is chosen to be 0.7. Hence, the real critical total liquid saturation is 0.77. Entrapment is not included. Similar to Hofstee et al.(1997), we decrease the equivalent PCE pressure head, h_o, from -0.06 m to -0.555 m in 99 increments of 0.005 m. The water pressure head, h_w, was not measured during the experiment. Hence, we were free to choose h_w. Good agreement is obtained if we decrease h_w from -0.22 m to -0.306 m in increments of 0.045 m. After the oil becomes residual, the water pressure decreases with smaller increments of 0.002 m, until a water pressure head of -0.4655 m is obtained.

Water, PCE and total liquid saturations during drainage of both experiment and simulation are shown in Fig. 2.10. On the vertical axis h_o as defined by Eq.(2.20) is given and on the horizontal axis the water, PCE and total liquid saturations are given. In principle, when the PCE pressure is decreased, the PCE saturation decreases too and, conversely, the water saturation increases. After the pressure head has decreased below 0.18 m the PCE saturation remains constant whereas the water saturation starts to decrease. Apparently, the PCE has become residual. As for the critical PCE pressure head (h_{or}^c) this implies that it is equal to 0.18 m. Further reduction of the PCE pressure head does not affect the PCE saturation anymore, instead, the water saturation decreases, indicating that the air-water interface has taken over control. Given the fitted water pressure heads, the model and the experiment give similar changes of the saturations. The transition to residual saturation of PCE in the experimental data match well with the transition in the residual oil model. In addition, the experimentally measured PCE saturation remains constant during the drainage experiment which corresponds with the residual PCE in the model. However, the critical total liquid saturation is very high. According to the pore scale model and calculations presented in App. A and based on the fluid characteristics of PCE, we would expect a maximum S_t^c of around 0.56. This implies that the applied S_t^c is physically not realistic for a pore model consisting of equally large spheres. Real sand, however, consists of grains of various geometries and sizes; very high S_t^c's may be possible. Experimental validation is recommended though. We recommend experimental measurements for various porous materials and various fluid combinations. As the water pressure heads were not measured during the experiment we recommend to measure them in future experiments.
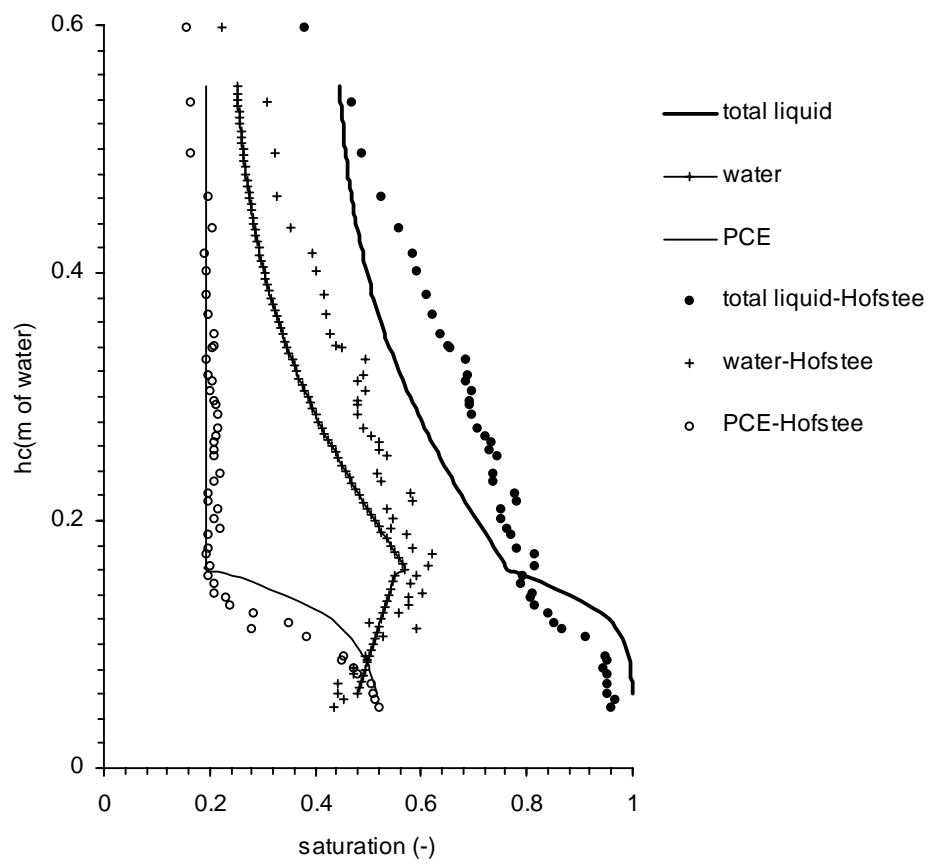
Figure 2.10: Comparison of experiment by Hofstee et al. (symbols) and calculations performed by the residual oil model (lines).

2.6 Conclusions

Non-drainable residual NAPL should be included in multiphase flow models as experiments have shown the existence of this residual NAPL.

We developed a (static) set of saturation-capillary pressure relations for a three phase system which accounts for both non-drainable residual NAPL as well as entrapped NAPL. The constitutive set of saturation-capillary pressure relations for non-drainable residual NAPL is based on qualitative relations derived from a pore scale model. According to the pore scale model, pendular rings around the contact points of sand grains retain residual water and non-drainable residual NAPL. Non-drainable residual NAPL increases for NAPLs that have a negative spreading coefficient. Furthermore, a higher water content results in a lower non-drainable residual NAPL saturation. Next, from the pore scale model follows that non-drainable residual NAPL saturation is defined as the NAPL that becomes immobilized below a threshold total liquid saturation.

The residual NAPL set of equations is formulated similar to the set of relations developed by Parker et al. (1987). Analyses showed that to include non-drainable residual NAPL a residual NAPL system has to be added to the existing two-phase and three-phase system, and a critical NAPL pressure should define the transition from free, mobile NAPL to residual NAPL. Next, in the residual NAPL system an artificial parameter is needed that reflects the mutual dependency of S_t and S_w. We denoted the latter parameter as the non-drainable residual NAPL (or oil) pressure head. The non-drainable residual NAPL pressure head depends on both the residual NAPL saturation and the history of the pressure heads and is independent of the real NAPL pressure head.

Drainage example calculations show well defined and physically consistent behavior and smooth transitions between the residual and the non-residual systems.

Entrapment can be included easily by using the model of Kaluarachchi and Parker (1992). Residual NAPL in the unsaturated zone reacts in opposite way on water level fluctuations as entrapped NAPL does. Non-drainable residual NAPL can become entrapped and entrapped NAPL can become non-drainable. In static example calculations that consist of a sequence of static $Pc - S$ relationships, we were able to state this mutual cooperation that results in retention of NAPL.

Experiments conducted by Hofstee at al. (1997) with non-drainable residual PCE were simulated as a set of successive static $Pc - S$ curves
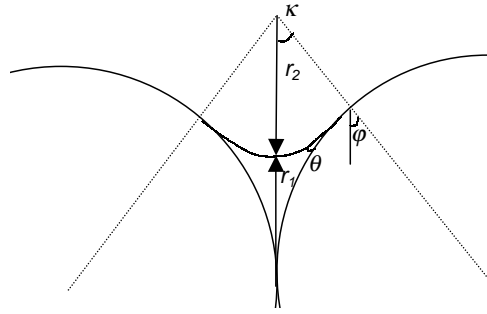
Figure 2.11: Cross-section through fluid torus (after Mayer and Stowe, 1966).

including residual NAPL. Based on parameters measured by Hofstee at al. (1997) and visually fitted parameters we found similar behavior with our model as was found in the experiment. Although more experiments will be needed to verify the model, results are promising.

Appendix A Calculation of the pore liquid volume

In the Fifties and Sixties Kruyer (1958) and Mayer and Stowe (1965,1966) performed calculations for a similar spherical configuration as we adopted in this paper. They considered only one fluid (mercury) and one gas phase. Their formulas can be used, however, to show the response of a system of disconnected rings (called torus) to the contact angle of the interface between two fluids (gas, oil) and the third fluid (water). This contact angle

$$\cos \theta_{ao} = 1 + \frac{C_s^{eq}}{\gamma_{ao}}, \qquad (2.21)$$

represents the tendency of a intermediate wetting fluid to spread in the presents of two other fluids for a strongly water wet solid (Kalaydjian, 1992).

   We assume a porous medium that consists of packed spheres of which in horizontal direction the centers are situated at an angle of 60° to each other and in vertical direction on top of each other. Hence, each sphere
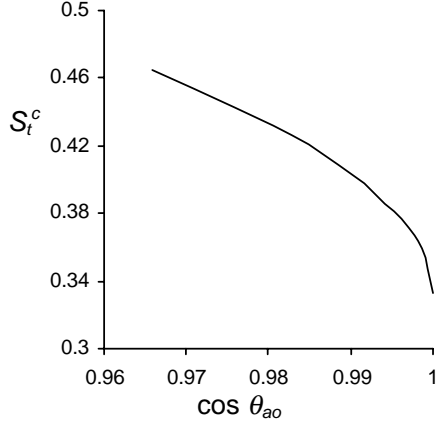
Figure 2.12: Total liquid saturation (S_t) versus $\cos\theta_{ao}$ in sphere model.

has 8 contact points. Let us consider three interconnecting rings as given in Fig. 2.2 that are about to disconnect. The centers of the spheres form an equilateral triangle. The cross-section shown gives the closest possible packing for spheres. In case of imbibition, the rings of oil will connect here and imbibe into the space between the rings and form bridges between the oil rings. We assume that the oil becomes mobile when imbibition occurs. Hence, the volume occupied by the liquid rings gives the residual volume.

Fig. 2.11 shows a cross-sections through one ring containing water as well as oil. In the figure only the air-oil interface is shown. The water film that is wrapped around the spheres and the water ring are not shown. Surface tensions cause the interface between the oil ring and the air to be curved. Actually, the air oil interface is curved in two directions and therefore two radii can be distinguished. One radius starts from the center of the ring, pointing to the middle of the air-oil interface and one defines the curve shown in the cross-sections (respectively denoted as r_1 and r_2).

Following Mayer and Stowe (1966, Eq.(10)), the volume of a toroidal volume, V_t, is given by :

$$V_t = 2\pi \left[fj^2 - f^2 j \cot\kappa - g^2 j\kappa + fg^2 - rf^2 \right], \qquad (2.22)$$

where:

- $\kappa = \varphi - \theta$ [rad],

- $f = r(1 - \sin\varphi)$ [L],

- $g = \frac{f}{\sin\kappa}$ [L],

- $j = r\cos\varphi + g\cos\kappa$ [L],

- r = radius of the spheres [L]

- θ = the contact angle of air-oil interface and the water film [rad],

- $\varphi = \frac{1}{6}\pi$, the angle between the center of a sphere and the intersection of the two liquid interfaces [rad].

The unit cell for our sphere packing is a hexagonal in horizontal direction and a square in vertical direction. The unit cell volume is therefore $V_u = \frac{6}{\sqrt{3}}r^2 * 2r$ and the volume of a sphere (V_s) is $\frac{4}{3}\pi r^3$. As the porosity is defined as $n = \frac{V_u - V_s}{V_u}$. For our packing we find $n = 0.39$ which is a reasonable value.

The liquid volume of one pendular ring associated with each contact point is shared by two spheres. Hence, the volume of residual fluids associated with each sphere or unit cell is $\frac{1}{2}V_t * 8$ (8 contact points). In Fig. 2.12 the dependency of the residual saturation (total liquid) to the contact angle is shown. The growing residual volume for an increasing contact angle coincides with the experimental observations (Zhou and Blunt, 1997; Chatzis et al., 1988); a more negative spreading coefficient gives a larger residual oil saturation.

Appendix B Summary of the residual model

Three fluid systems can be distinguished in the model:

- 2 phases (air-water),

- 3 phases (air-oil-water),

- oil is residual (air-non-drainable residual oil-water).

The critical oil pressure heads define the switches between the systems (Eq. (2.8) and (2.12)). Then, one can calculate the fluid distribution following this procedure:

1. Calculate h_o^c and h_{or}^c out of h_w, h_o and $\overline{S}_t^c$ (and the van Genuchten parameters α, n and the scaling parameters β_{aw}, β_{ow} and β_{ao}).

2. Determine which system is dealt with: two phases, three phases or residual non-drainable oil.

3. If a three or a two phase system is dealt with, calculate $\overline{S}_t$ and $\overline{S}_w$(or $\overline{S}_{wa}$ and $\overline{S}_{of}$) after these $\overline{S}_o$ by applying the relations of Section 2.2.

4. If there is residual non-drainable oil, calculate $\overline{S}_w$ (or $\overline{S}_{wa}$ and $\overline{S}_{of}$) out of the three phase or the two phase as if no residual non-drainable oil would exist (see section 2.2). Start the iterative procedure (stop if h_{or} is constant):

    (a) Calculate $\overline{S}_{or}^{ini}$ (Eq. (2.16) to (2.19)).
    (b) Calculate $\overline{S}_{or}$ (Fig. 6).
    (c) Calculate $\overline{S}_t$ (Eq. (2.13)).
    (d) Calculate h_{or} belonging to this new $\overline{S}_t$ (Eq. (2.15)).
    (e) Calculate $\overline{S}_w$ (or $\overline{S}_{wa}$ and $\overline{S}_{of}$) belonging to this new h_{or} (Eq. (2.14)). Only when $h_o > h_{or}$ (4th event) go out of the loop and calculate $\overline{S}_{or}$ like you are in a three phase system.
    (f) Go back to step 4a.

Notation

C_s^{eq}	equilibrium spreading coefficient $[\mathrm{Nm}^{-1}]$
g	gravity $[\mathrm{m\ s}^{-2}]$
h_i	water equivalent pressure head fluid i [m]
h_{ij}	water equivalent capillary pressure head fluid i and j [m]
n, m	van Genuchten porous medium parameters
P_i	pressure fluid i [Pa]
$P_{c,ij}$	capillary pressure fluid i and j [Pa]
S_i	saturation fluid i
$\overline{S}_i$	effective saturation fluid i

Z_{ij}	depth below surface where fluid pressures i and j are equal [m]
α	van Genuchten porous medium parameter [m^{-1}]
β_{ij}	scaling coefficients for $P_c - S$ relationships
γ_{ij}^e	equilibrium interfacial tension between fluid i and j [Nm^{-1}]
θ_{ij}	contact angle between solid and fluid interface
ρ_i	relative density fluid i

Subscripts

a	air
m	residual water
o	oil
of	free oil
or	non-drainable residual oil
ot	trapped oil
t	total liquid
w	water
wa	apparent water

Superscripts

c	critical
min	historical minimum
max	maximum
ini	initial

References

Abriola, L.M. and Pinder, G.F., 1985. A multiphase approach to the modeling of porous media contamination by organic compounds 2. numerical approach. Water Resources Research, 21(1):19–26.

Bear, J., 1972. Dynamics of Fluids in Porous Media. American Elsevier.

Celia, M.A., Reeves, P.C. and Ferrand, L.A., 1995. Recent advances in pore scale models for multiphase flow in porous media. Reviews of Geophysics, 33:1049–1057.

Chatzis, I., Kantzas, A. and Dullien, F.A.L., 1988. On the investigation of gravity-assisted inert gas injection using micromodels, Long Berea sandstone cores,

and computer assisted tomography. In: 63th Annual Technical Conference and Exhibition of the Society of Petroleum Engineers, Houston, TX, SPE 18284.

Dong, M., Dullien, F.A.L. and Chatzis, I., 1995. Imbibition of oil in film form over water present in edges of capillaries with an angular cross section. Journal of Colloid and Interfacial Science, 172:21–36.

Eckberg, D.K. and Sunada, D.K., 1984. Nonsteady three-phase immiscible fluid distribution in porous media. Water Resources Research, 20(12):1891–1897.

Faust, C.R., 1985. Transport of immiscible fluids within and below the unsaturated zone. Water Resources Research, 21(4):587–596.

Fenwick, D.H. and Blunt, M.J., 1998. Three-dimensional modeling of three phase imbibition and drainage. Advances in Water Resources, 21(2):121–143.

Ferrand, L.A., Celia, M.A. and Soll, W.E., 1990. Percolation-based models for pore-to lab scale calculations in multifluid porous media. In: Dynamics of Fluids in Hierarchical Porous Media. Academic, San Diego, CA, pp. 463–483.

Hayden, N.J. and Voice, T.C., 1993. Microscopic observation of a NAPL in a three-fluid-phase soil system. Journal of Contaminant Hydrology, 12:217–226.

Hoag, G.E., and Marley, M.C.,1986. Gasoline residual saturation in unsaturated uniform aquifer materials. Journal of Environmental Engineering, 112(3):586–604.

Hofstee, C., Dane, J.H. and Hill, W.E., 1997. Three-fluid retention in porous media involving water, PCE and air. Journal of Contaminant Hydrology, 25:235–247.

Jarsjö, J., Destouni, G. and Yaron, B., 1994. Retention and volatilisation of kerosine: laboratory experiments on glacial and post-glacial soils. Journal of Contaminant Hydrology, 17:167–185.

Kalaydjian.,F. J.-M., 1992. Performance and analyses of three-phase capillary pressure curves for drainage and imbibition in porous media. 67th Annual Technical Conference and Exhibition of the Society of Petroleum Engineers, Washington, DC, SPE 24878.

Kaluarachchi, J.J. and Parker, J.C., 1992. Multiphase flow with a simplified model for oil entrapment. Transport in Porous Media, 7:1–14.

Kruyer, S., 1958. The penetration of mercury and capillary condensation in packed spheres. Trans. Faraday Society, 54:1758–1767.

Land, C., 1968. Calculations of imbibition relative permeability for two- and three-phase flow from rock properties. Trans.Am.Inst.Min.Metall.Pet.Eng., 243:149–156.

Lenhard, R.J. and Parker, J.C., 1987a. Measurement and prediction of saturation-pressure relationships in three-phase porous media systems. Journal of Contaminant Hydrology, 1:407–424.

Lenhard, R.J. and Parker, J.C., 1987b. A model for hysteretic constitutive relations governing multiphase flow 2. permeability-saturation relations. Water Resources Research, 23(12):2197–2206.

Leverett,   M.C.,   1941.   Capillary   behavior   in   porous   solids. Trans.Am.Inst.Min.Metall.Pet.Eng., 142:152–169.

Luckner, L., van Genuchten, M.Th. and Nielsen, D.R., 1989. A consistent set of parametric models for the two-phase flow of immiscible fluids in the subsurface. Water Resources Research, 25(10):2187–2193.

Mayer, R.P. and Stowe, R.A., 1965. Mercury porosimetry-breakthrough pressure for penetration between packed spheres. Journal of Colloid Science, 20:893–911.

Mayer, R.P. and Stowe, R.A., 1966. Mercury porosimetry: Filling of toroidal void volume following breakthrough between packed spheres. Journal of Physical Chemistry, 70:3867–3873.

McBride, F.J., Simmons, C.S. and Cary, J.W., 1992. Interfacial spreading effects on one-dimensional organic liquid imbibition in water-wetted porous media. Journal of Contaminant Hydrology, 11:1–25.

Mercer, J.W. and Cohen, R.M., 1990. A review of immiscible fluids in the subsurface: properties, models, characterization and remediation. Journal of Contaminant Hydrology, 6:107–163.

Parker, J.C. and Lenhard, R.J., 1987. A model for hysteretic constitutive relations governing multiphase flow 1. saturation relations. Water Resources Research, 23(12):2187–2196.

Parker, J.C., Lenhard, R.J. and Kuppusamy, T., 1987. A parametric model for constitutive properties governing multiphase flow in porous media. Water Resources Research, 23(4):618–624.

van Genuchten, M.Th., 1980. A closed form equation for predicting the hydraulic conductivity of unsaturated soils. Soil Science Society American Journal, 44:892–898.

Waddill, D.A. and Parker, J.C., 1997. Recovery of light, non-aqueous phase liquid from porous media: laboratory experiments and model validation. Journal of Contaminant Hydrology, 27:127–155.

Zhou, D. and Blunt, M., 1997. Effect of spreading coefficient on the distribution of light non-aqueous phase liquid in the subsurface. Journal of Contaminant Hydrology, 25:1–19.

Chapter 3

Experimental determination of residual NAPL in the unsaturated zone*

3.1 Introduction

Spills of Non Aqueous Phase Liquids (NAPLs), such as gasoline, fuel oils and chlorinated hydrocarbons, have caused contamination of numerous aquifers. These liquids have a low miscibility with water and may move as a discrete liquid phase. After a NAPL is spilled at the soil surface, the liquid will migrate downward towards the water table due to gravitational and capillary forces. Not all of the liquid will reach the water table, since part of it becomes immobilized in the capillaries of the porous medium. We will refer to this retained NAPL as *non-drainable residual* NAPL. It is the liquid that, after drainage, exists as disconnected blobs or ganglia in the presence of water and air in a water-wet soil (Wipfler and van der Zee, 2001). In this respect it differs from entrapped NAPL which becomes immobilized by the imbibing wetting water phase by bypassing mechanisms and snap off (Chatzis et al., 1983). As far as we know, non-drainable residual NAPL has not been incorporated in multi-phase flow models that are used to model contaminated sites. For designing efficient subsurface cleanup strategies, it is essential to account for non-drainable residual NAPL in remediation, and therefore, in multi-phase flow models.

Recently, Wipfler and van der Zee (2001) developed a constitutive model that also considers non-drainable residual NAPL. The model is based on a conceptual pore scale model consisting of packed spheres of different sizes that are water-wet. The spheres are placed in a large column which is first imbibed by water and drained to residual saturation, and subsequently,

---

*by E.L.Wipfler and S.E.A.T.M. van der Zee

imbibed by NAPL and drained to NAPL residual saturation. Because water is the wetting fluid, it will wet the porous medium and form a film around the spheres at this low water saturation. In addition, a (wetting) pendular ring of water is formed around the contact points between the spheres due to capillary forces. If, after NAPL imbibition, the NAPL pressure is decreased sufficiently NAPL rings will be formed around the water rings, since NAPL is the intermediate wetting fluid. The NAPL volume in these rings is considered as non-drainable residual NAPL.

According to the model, the volume of non-drainable residual NAPL increases, if the spreading coefficient[†] decreases. Furthermore, a higher water saturation results in a lower non-drainable residual saturation. In the model of Wipfler and van der Zee (2001) non-drainable residual NAPL becomes immobilized below a certain critical total liquid saturation, S_t^c. This critical total liquid saturation is porous medium and fluid dependent.

Although the model adequately simulated the experimental data of Hofstee et al. (1997), this agreement is a shallow basis for assessing whether the model assumptions are valid. For this purpose we developed an experimental set up especially designed to measure three-phase $P_c - S$ relationships and non-drainable residual saturation including the measurement of the water saturation and pressure. Prior to the development of the experimental set up, we searched in the literature for available macroscale experimental data that could provide us with non-drainable residual saturation data. We selected a number of papers that reported non-drainable residual data and that could help to verify the constitutive model of Wipfler and van der Zee (2001). We analyzed the obtained data and, in addition, we performed a couple of experiments using the experimental set up.

3.2   Experimental data from the literature

To get a first impression of the validity of the model by Wipfler and van der Zee (2001), a number of papers was screened regarding non-drainable residual NAPL measurements after gravity drainage of NAPL. We care-

---

[†]The spreading coefficient reflects the ability of a NAPL to spread in the presence of water and air. If $C_s \geq 0$, the NAPL tends to spread between the two other phases and if $C_s < 0$, it tends to form droplets. The interfacial tensions can change as the interfaces age, i.e. they become contaminated with molecules from other liquids, which might result in a change in the spreading coefficient. The aged spreading coefficient is considered as the equilibrium spreading coefficient, C_s^{eq}. C_s^{eq} is generally lower than C_s. $C_s^{eq} = 0$ for spreading liquids and $C_s^{eq} > 0$ for non-spreading liquids.

fully selected the papers reporting non-drainable residual NAPL and the corresponding relationships to (1) the spreading coefficient, (2) the water saturation, (3) the type of experiment that was performed and (4) the type of porous medium of the experiments. The experimental data are restricted to the measurements of non-drainable residual saturation after gravity drainage, i.e. is neither increased or decreased, as other data were not available in the literature. The data, the classification of the experiments and the selection criteria are given in Appendix A.

We collected 26 non-drainable residual saturation (S_{or}) values from 9 references. Eleven S_{or} values were from spreading liquids and 15 from non-spreading liquids. Four S_{or} values are measured using sandstone, three values are from glass beads experiments and the other 19 values are obtained using sand as a porous medium. S_{or} ranges between 0.001 and 0.23 of which sandstone ranges between 0.03-0.2, sand ranges between 0.001-0.23 and glass beads between 0.006-0.02. The average value of the sandstone is slightly more than the residual saturation of the sand and the glass beads.

By considering individually the data of each paper, it is observed that the measured S_{or} is lower for spreading liquids than for non-spreading liquids. In Figure 3.1, the measured S_{or} is related to the spreading coefficient of the papers that report a series of measurements of which only C_s was varied. The equilibrium spreading coefficient, C_s^{eq} is given when it is reported in the paper or otherwise C_s is given. The lines connect the measurements reported in each individual paper. For the data set of Kantzas et al. (1988) glass beads are used whereas for the other experiments sand is used. For spreading liquids we assumed that $C_s^{eq} = 0$. Figure 3.1 shows that S_{or} has a tendency to increase when C_s/C_s^{eq} becomes more negative which is in agreement both with the pore scale model of Wipfler and van der Zee (2001) and with the expectation that non-spreading NAPL is easier broken into separate blobs and droplets. This relation between S_{or} and C_s has already been observed and mentioned in papers by e.g. Kantzas et al. (1988),Vizika and Lombard (1996) and Zhou and Blunt (1997). Still, a considerable spreading can be observed between the measured S_{or} values of the individual experiments. This might be attributed to different sand types or different performed experiments. Furthermore, although the data are selected carefully, different performance of the experiments might have biased the measured S_{or} values.

From Figure 3.1, it becomes apparent, that the levels of the different lines depends much on other properties than C_s. It is plausible, that prop-
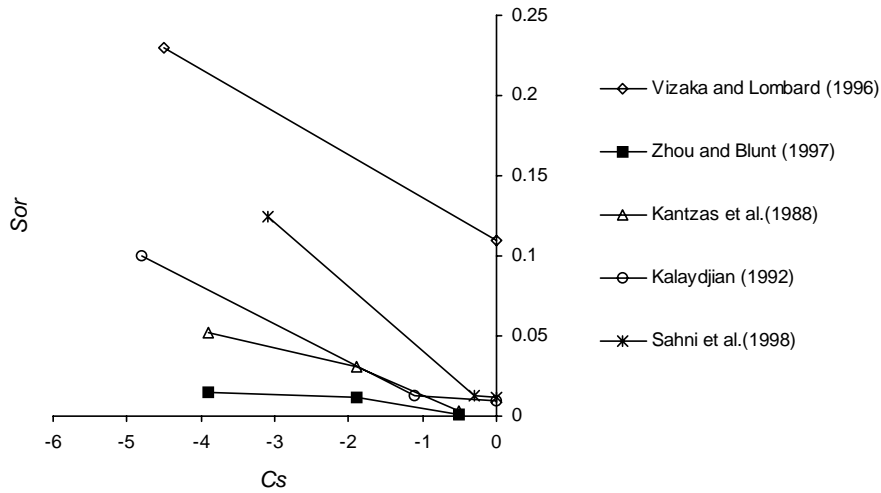
Figure 3.1: The (equilibrium) spreading coefficients, C_s and C_s^{eq} and the corresponding measured S_{or} values reported in five papers.

erties of the porous medium such as pore size distribution and grain shape are related with the different levels of $S_{or}(C_s)$-relationships. Unfortunately, the provided data are insufficient to assess such relationships. There are two major reasons why this is impossible: 1) regarding the assessment of S_{or}, there is a different focus between the papers, i.e. some papers emphasize the dependency on C_s/C_s^{eq}, whereas others focus on other parameters such as S_w, and 2) the used material (porous medium) has varies also between the different papers. It would require a more comparable description of the different porous media, in terms of e.g. mean pore size, variance and other (higher moment) pore size distribution statistics.

3.3   Experimental set up

To contribute to the data sets available from the literature, we conducted experiments. We developed a special measurement apparatus that facili-

tates independent control of the water pressure and saturation and NAPL pressure and saturation. Different from the literature data, these experiments were conducted in a suction chamber. The reason for doing so, is that we are interested in the behavior in the liquid unsaturated zone and it is not ascertained that experiments performed under overpressure can be translated to the unsaturated zone without corrections. In the suction plate apparatus we decrease the NAPL pressure which is more consistent with the physical system of the water unsaturated zone than increasing the air pressure as is done in the more commonly used pressure cells, because subsurface air can be considered at constant atmospheric pressure. In addition, a sudden increase of the air pressure may lead to high flow rates of the air, which may lead to bypassing of the NAPL leaving it as isolated blobs in the capillaries of the porous medium and an overestimation of the residual saturation. An overview of suction and pressure cell apparati used to measure two and three-phase $p_c - S$ relations, is provided by Ferrand et al. (1990).

Our suction plate apparatus uses two types of semi-permeable membranes. One separator is hydrophilic and one is hydrophobic. Both membranes enable hydraulic contact of the wetting phase from the core to the external burettes. The pressures of water and NAPL are varied independently. The apparatus is shown in Figs. 3.2 and 3.3. A stainless steel core holder with a inner diameter of 86 mm is filled with sand. Both a glass burette (50 ml) containing demineralized water and a glass burette containing NAPL (50 ml) are connected to the bottom of core holder through respectively a set of hydrophilic semi-permeable membrane filters (Nylon, 0.2 μm in pore diameter, provided by Alltech, IL,USA) and a set of hydrophobic semi-permeable membrane filters (Durapore, 0.22 μm in pore diameter, provided by Millipore, Ireland). With respect to the hydrophilic membranes, water is the wetting fluid and, therefore, the membranes have a certain entry pressure for NAPL and air. With respect to the hydrophobic membranes, the NAPL is the wetting fluid and the membranes have an entry pressure for water and air. There are four membranes, two of each type, with a diameter of 36 mm. The membranes are positioned in one of the four openings in the bottom of the core holder. The openings in the bottom are smaller (Ø 30 mm) at the first 1 mm of the bottom of the core holder to facilitate the attachment of the membranes. Each membrane is pressed against this flat stainless steel ring by a stainless steel funnel. Flat Viton rings (provided by Eriks, The Netherlands) with a inner diameter of
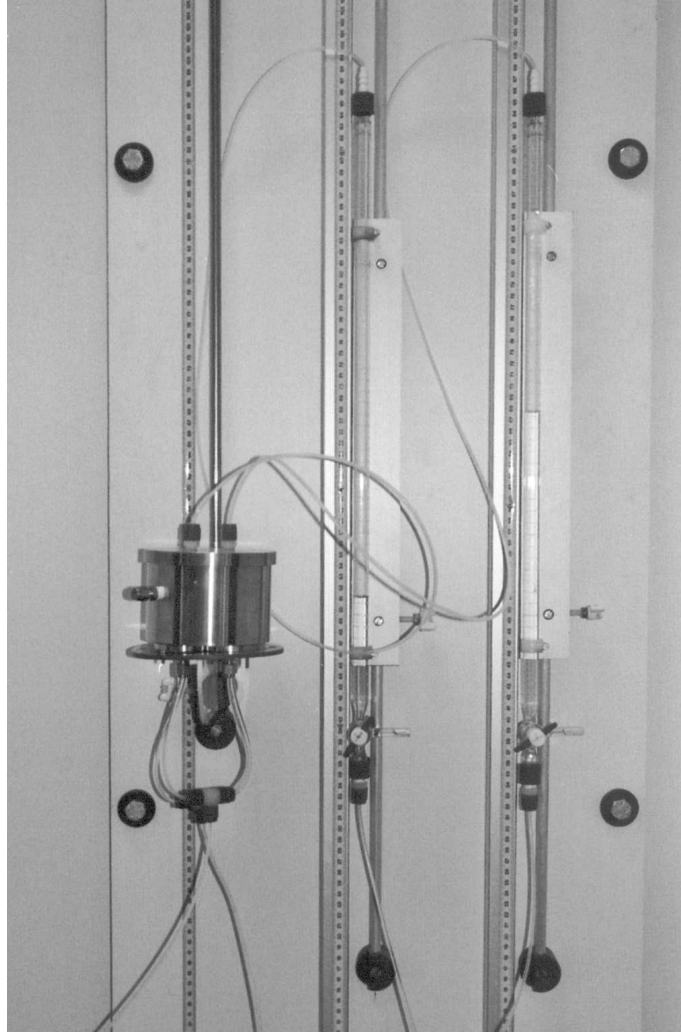
Figure 3.2: Experimental set up. A core holder is connected to two burettes containing NAPL (left) and water (right) though semi-permeable membranes that are attached to the bottom. Water and NAPL pressure in the core are increased and reduced due to lifting and lowering of the burettes. A tap is placed on the core holder and connected to the burettes to maintain the air saturated with water and NAPL and to prevent evaporation.
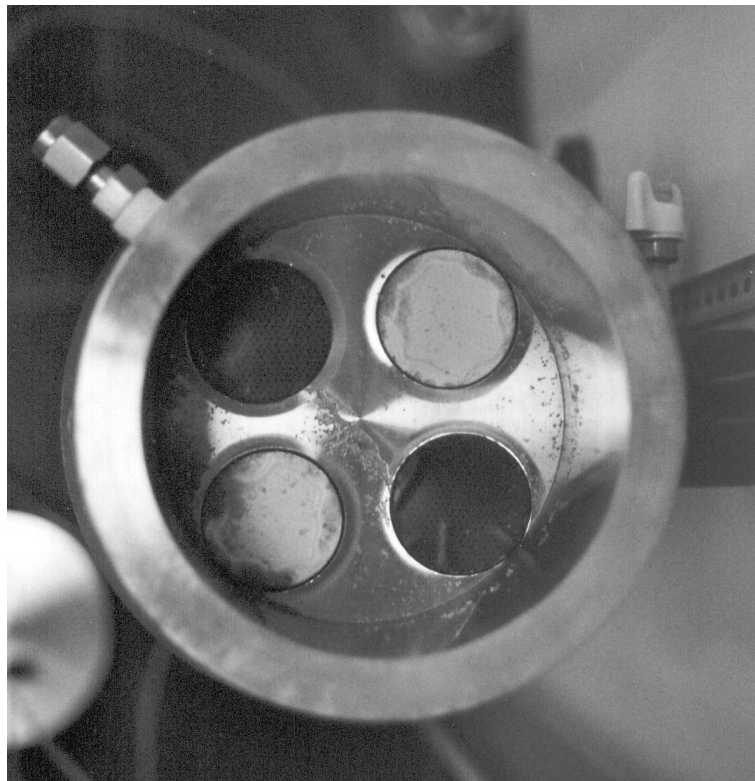
Figure 3.3: Picture from the bottom of the core holder taken from above. Four semi-permeable membranes are attached to the bottom; two are hydrophobic (dark color) and two are hydrophilic (light color). The membranes are connected to a NAPL reservoir and a water reservoir, respectively.
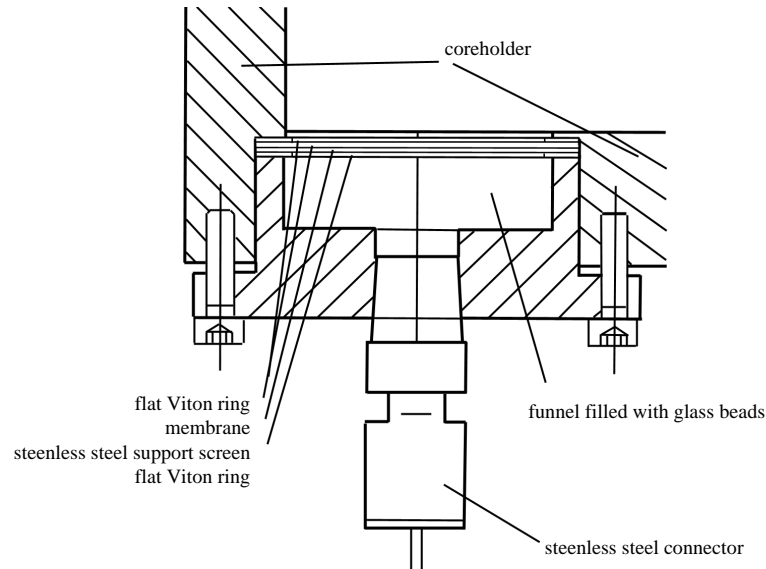
Figure 3.4: Cross-section through one funnel and core holder. The connection of the membranes to the core holder is maintained using two bolts that press the funnel tightly against a layer consisting of a flat Viton ring, a membrane, a support screen and again a flat Viton ring.

31.0 mm, an outer diameter of 36.0 mm and a thickness of 1.0 mm, are situated between the membranes and the core holder. Below the membranes a permeable stainless steel support screen is situated and between this support and the funnel again a similar flat Viton ring is posed. The funnels fit closely in the holder and they are pressed tightly to the bottom of the core holder by small bolts in order to maintain the membranes air-tight connected (see Figure 3.4).

Between the membranes and the sand, paper tissues are placed inside the core holder to gain good capillary contact. Perfluoraloxy tubes and stainless steel and Perfluoraloxy fittings (Swagelok, provided by Amsterdam Valves and Fittings BV) are screwed into the funnels and connected to the burettes. To keep the water and NAPL volumes in the funnels and in the tubes small (less effect from density differences due to pressure differences),

we filled the funnels with glass beads and we used small tubes with an outer diameter of 1/8 inch. A tap was placed loosely on top of the core holder, which prevented evaporation but maintained the air pressure at constant (atmospheric) pressure. This tap of the core holder is connected to the burettes again by perfluoraloxy tubes to facilitate the gas phase to be fully saturated by NAPL and water vapor.

Water and NAPL pressure are increased or reduced by lifting or lowering of the burettes. When hydrostatic equilibrium is reached, corresponding pressures and fluid saturations are measured in the burettes. Pressures were measured with an accuracy of 1 mm and volumes with an accuracy of 0.1 ml.

The experimental set up is able to measure three-phase $P_c - S$ relationships of which the water pressure and saturation and the NAPL pressure and saturation could be varied independently. Hence, the set up is not only able to measure non-drainable residual NAPL saturation but all three-phase $P_c - S$ relationships. However, during the development of the experimental set up, we were confronted with considerable problems due to using a suction cell. It appeared to be almost impossible to get the apparatus air-tight, especially the connection of the membranes to the core holder. Although we succeeded in getting the experimental set up air-tight, it remained sensitive to air intrusion.

3.4   Materials and methods

We selected clean washed quartz sand (99.1% quartz) that does not contain humic substances as these may affect liquid adsorption or other surface chemical reactions (Dorsilit, provided by Eurogrit, The Netherlands). The particle density of the sand is 2.6 kg/l, the dry bulk density is 1.5 kg/land the porosity is 0.423. The percentage of the particle size classes <0.063, 0.063-0.125, 0.125-0.25, 0.25-0.5, 0.5-1.0, 1.0-2.0 mm were 0.4 %, 0.2 %, 5.1 %, 51.1 %, 40.0 % and 3.1 %, respectively.

The used NAPL was non-spreading and lighter than water; n-dodecane (Merck, Germany). It was chosen because we expected to measure more pronounced residual saturations than in case of spreading liquids. Furthermore, dodecane is insoluble to water and poorly volatile. For convenience the liquid is slightly colored with Sudan IV red dye to enable visual differentiation of the NAPL from the water. Fluid characteristics of dodecane are, interfacial tensions γ_{aw}=72.1 Dyne/cm, γ_{ao}= 25.1 Dyne/cm

and γ_{ow}=53.3 Dyne/cm, the spreading coefficient C_s=-5.8 Dyne/cm, the equilibrium spreading coefficient C_s^{eq}=-6.1 Dyne/cm and the density is 0.75 kg/m^3 (Hirasaki, 1993).

Four experiments were performed. Before starting the experiments the burettes, the funnels and the connecting tubes were completely filled with the corresponding liquid (water, n-dodecane). The tissues were placed and the core holder was filled with 304 gram of sand, which coincides with a height of 3.5 cm of the core and a pore volume of 86 ml. The core was shortly vibrated. The elevation of the center of the core was taken as the reference level and attributed the height of zero. Experiments were performed at a temperature of $20° \pm 2°$.

The experimental procedure for each experiment can be summarized as follows. (1) Water is imbibed via the hydrophilic membrane at the bottom of the core holder, (2) water is drained via the bottom of the core holder, (3) n-dodecane imbibes via the hydrophobic membrane at the bottom of the core holder, (4) n-dodecane is drained via the hydrophobic membrane at the bottom of the core holder, (5) n-dodecane is introduced at the top of the core and drained.

From the beginning of the experiment fluid volumes that were imbibed or drained from the core were measured. During the NAPL drainage process, step (4), the NAPL pressures were decreased gradually and measurements were taken at every pressure interval to obtain a NAPL drainage $P_c - S$ relationship. Measurements were taken at hydrostatic equilibrium and time intervals varied between 1 and 5 days. At the end of the drainage experiment the time intervals were larger to obtain hydrostatic equilibrium. Step (5) was included to be able to distinguish between de effect of (a) NAPL displaced by water without air entrapment and (b) a downward moving NAPL spill (NAPL displacing air with air entrapment). Similar, measurements were taken when hydraulic equilibrium has been reached.

3.5   Experimental results

During the first experiment that was performed 50.9 ml water imbibed into the core holder, and subsequently, 24.7 ml of it drained. Then, dodecane imbibed through the hydrophobic membranes (70.4 ml). During this dodecane imbibition 16.2 ml water was displaced by dodecane until only 8.5 ml was contained in the core holder. After the dodecane pressure head was equal to zero, the dodecane was drained gradually (4) and at static

equilibrium the pressure heads and saturations were measured until a water equivalent dodecane pressure head h_o of -57.8 cm was reached and a non-drainable residual volume of 4.6 ml. During the dodecane drainage process the water pressure head, h_w, varied between -54.1 and -52.3 cm. The entire experiment took 26 days.

In the usually applied three-phase constitutive model of Parker et al. (1987), that does not incorporate non-drainable residual NAPL, below the critical NAPL pressure head, h_o^c, the NAPL ceases to exist since the three-phase system changes to a two-phase system. h_o^c is given by:

$$h_o^c = \frac{\beta_{ow} h_w}{\beta_{ow} + \beta_{ao}} \tag{3.1}$$

where β_{ij} is the ratio between the interfacial tensions; $\beta_{ow} = \frac{\gamma_{aw}}{\gamma_{ow}}$ and $\beta_{ao} = \frac{\gamma_{aw}}{\gamma_{ao} cos\theta_{ao}}$. At the end of the dodecane drainage in experiment 1, $h_w = -52.3$ cm. This implies that $h_o^c = -14$ cm. Below this value NAPL is not supposed to exist. In Figure 3.5, h_o and the corresponding volume of water and dodecane in the core holder are given for experiment 1. The dodecane volume in the core holder decreases strongly between $h_o = 0$ and $h_o = h_o^c$, but for $h_o < h_o^c$ still a volume of dodecane ranging between 9.3 ml and 4.6 ml remains in the core holder which might indicate that the dodecane is at residual saturation below h_o^c. Similar type of behavior has been observed by Zhou and Blunt (1997).

The dodecane volume in the core decreases when h_o is decreased. This is not in agreement with the model of Wipfler and van der Zee (2001). According to this model, the water saturation should increase caused by the reduced water-dodecane capillary pressure and the total liquid saturation should remain constant.

Experiment 2 to 4 are performed similar to experiment 1 except that the water saturation during the dodecane drainage for each experiment is different (see Figures 3.6 to 3.8). In experiment 2, first, water was imbibed (57.4 ml) and drained to 17.4 ml in the core. Then, dodecane imbibed (66.6 ml) which causes a reduction of the water volume to 12.5 ml. Next, the dodecane was drained and pressures and saturations were measured at static equilibrium until a volume of 7 ml was left behind as non-drainable residual dodecane at $h_o = -48.8$ cm. The experiment took 17 days. During the experiment h_w is approximately -45 cm which corresponds to a h_o^c of -12.1 cm. Comparison between experiment 1 and 2 reveals that the curves are very similar. The higher water saturation of experiment 2 appears to have increased the residual saturation.

experiment 1

Figure 3.5: Dodecane water-equivalent pressure heads and corresponding volumes of water and dodecane in the core holder for experiment 1. The water pressure head is approximately -53 cm. h_o^c is indicated as a dashed line.
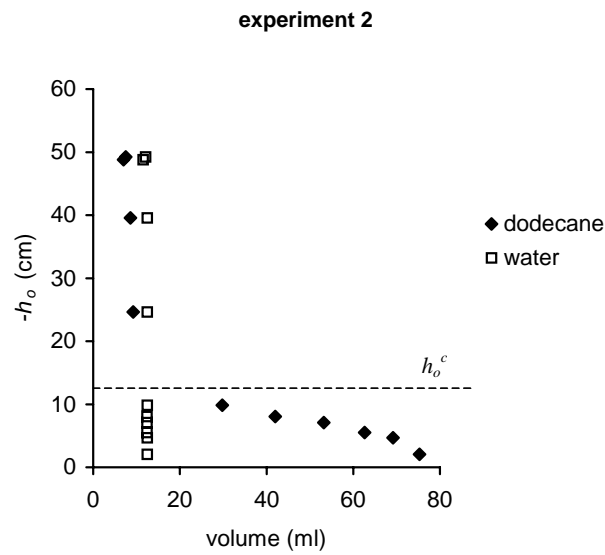
experiment 2

Figure 3.6: Dodecane water-equivalent pressure heads and corresponding volumes of water and dodecane in the core holder for experiment 2. The water pressure head is approximately -51.9 cm. h_o^c is indicated as a dashed line.

Figure 3.7: Dodecane water-equivalent pressure heads and corresponding volumes of water and dodecane in the core holder for experiment 3. The water pressure head is approximately -56.8 cm. h_o^c is indicated as a dashed line.
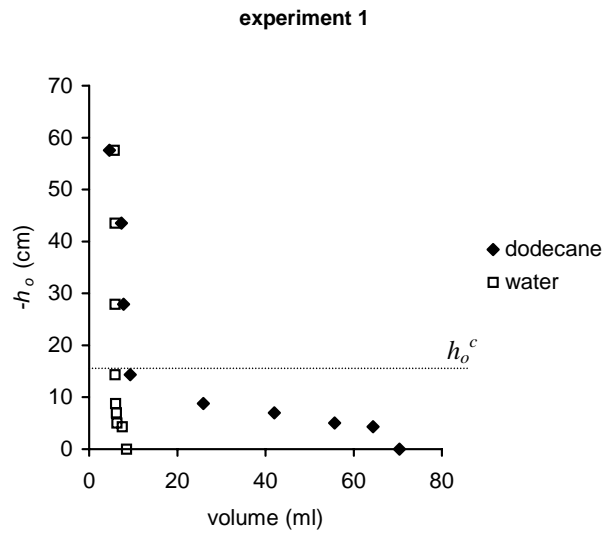
Figure 3.8: Dodecane water-equivalent pressure heads and corresponding volumes of water and dodecane in the core holder for experiment 4. The water pressure head is approximately -53 cm. h_o^c is indicated as a dashed line.
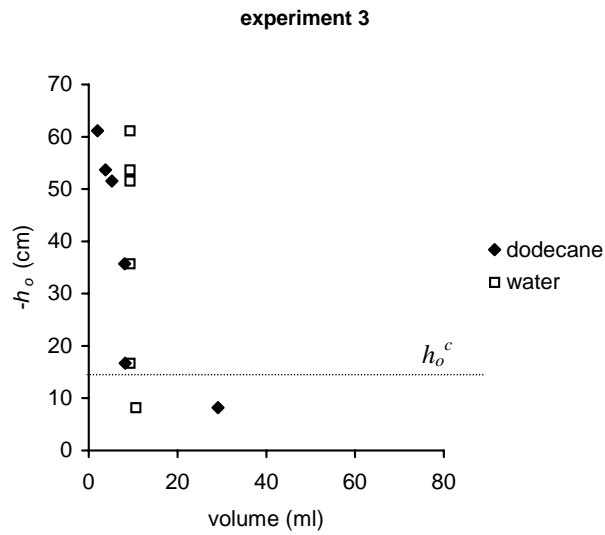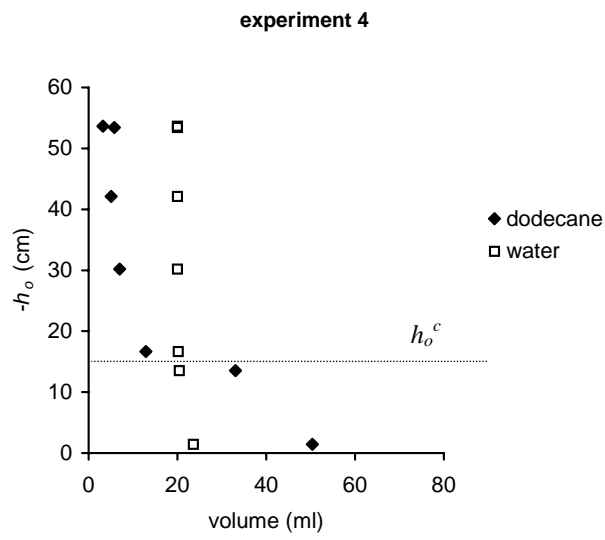
In experiment 3 and 4 we added step 5 to the procedure. To save time a lower volume of water was imbibed and drained and a lower volume of dodecane was imbibed in step 1 to 3. Hence, the dodecane drainage started at $h_o = -8$ cm instead of $h_o = 0$ cm. During the third experiment that we performed, 33.2 ml water imbibed the core and drained to 13.4 ml, and subsequently, dodecane was imbibed (46.2 ml). During this dodecane imbibition 2.2 ml of water was displaced. Then, dodecane was drained gradually and pressures and saturations were measured at static equilibrium until only 3.8 ml dodecane remained in the core at an equilibrium dodecane pressure head of -53.6 cm. Finally, 22.2 ml dodecane was introduced on top of the core and left to drain. At static equilibrium, 5.2 ml dodecane remained at a pressure head of -51.8 cm. The experiment took 11 days. During the experiment h_w is approximately -51.9 cm which corresponds to a h_o^c of -14.0 cm. The last experiment, nr. 4, consisted of imbibition of 31.3 ml water of which 7.7 ml drained until 22.2 ml water was left in the core holder. Then, dodecane was imbibed, 50.4 ml and drained until only 3.2 ml was left in the core holder at a pressure head of -53.4 cm. During dodecane imbibition 1.4 ml water was displaced by dodecane. Then, 10.1 ml dodecane was introduced from above and left to drain until only 5.8 ml was left in the core holder at a dodecane pressure head of -53.7 cm. The entire experiment took 16 days. During the experiment h_w is approximately -56.8 cm which corresponds to a h_o^c of -15.3 cm.

According to the model of Wipfler and van der Zee (2001), there is a porous medium property, the critical total liquid volume or saturation, S_t^c, that defines the total liquid saturation when NAPL is at residual saturation. In Figure 3.9 the total liquid volume, i.e. water and dodecane, is given for each experiment related to the measured h_o values. The figure shows that for the applied sand the total liquid volume at residual saturation varies for each experiment. Hence, the experimental results do not support the model at this point. Apparently, other mechanisms are involved that are not captured by the glass beads model of Wipfler and van der Zee (2001).

In addition, if we compare the volumes of water and dodecane at the end of each drainage experiment then we do not observe a correlation between the volume of dodecane retained in the core and the volume of water, which is expected from the sphere model of Wipfler and van der Zee (2001). In figure 3.10 the water saturation and the residual dodecane saturation are given at the end of step 4 for all four experiments.

Adding dodecane from the top of the core in relation to dodecane that
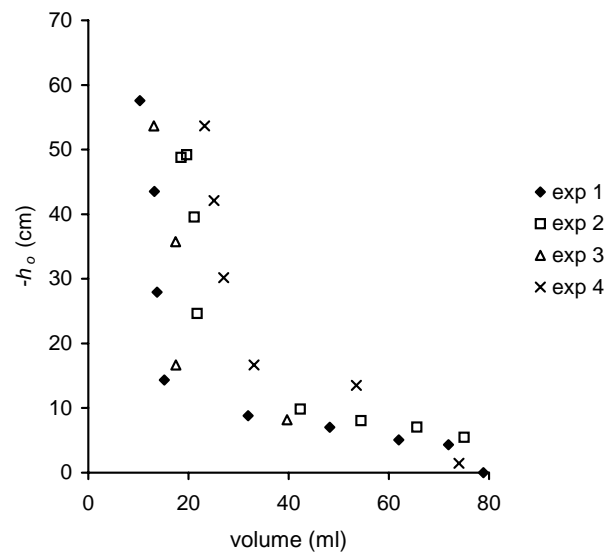
Figure 3.9: Total liquid volume corresponding to dodecane pressure heads for experiment 1 to 4.
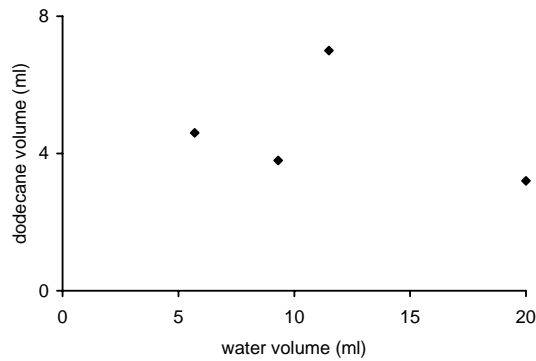
Figure 3.10: Volumes water and dodecane at the end of step (4)

is introduced from below, resulted in an increase of the retained volume of dodecane in the core: in experiment 3 the dodecane volume increased with a factor 1.4 from 3.8 ml to 5.2 ml and in experiment 4 the volume increased a factor 1.8 from 3.2 ml to 5.8 ml. This is probably due to air entrapment. When dodecane is spilled from above the air is likely to become occluded by the imbibing dodecane, whereas if the dodecane imbibed from below the air can easily move upward since it is much lighter than dodecane. This result might have impact on the modeling of dodecane spills at the subsurface, since the dodecane is generally spilled from above. In addition, the drainage and imbibition paths that are followed in future non-drainable residual NAPL experiments should be chosen carefully.

The volumetrically measured saturation was controlled gravimetrically at the end of each experiment by comparing the weight of the core holder filled with sand and tissue at the beginning of the experiments and the weight at the end of the experiments. The difference between volumes and weightings was very small. Hence, there was no mass loss due to e.g. volatilization. However, we noticed that a considerable volume of liquid was retained in the tissue. We measured for the sequential experiments 3.7, 8.2, 5.4 and 8.0 gr. that was retained in the tissue which corresponded with resp. 38.9 %, 47.4%, 40% and 31% of the retained liquids (water

and dodecane) at the end of each experiment. This is a considerable mass fraction. Considering that the liquid ratio in the tissue lies between only water and only dodecane, and considering that the pore volume of the sand is 86 ml, we may conclude that the S_{or} values after dodecane drainage are at maximum 0.053, 0.081, 0.06 and 0.067 for experiment 1 - 4, respectively. Paper can be considered as water-wet, hence, a fair assumption is that the ratio between the water and dodecane volumes in the sand is equal to the ratio in the tissue, in which case the S_{or} values after dodecane drainage (step 4) are 0.021, 0.039, 0.024 and 0.012. These residual saturation values are within the range that is reported in the literature, although the values are relatively small, especially considering that n-dodecane has a C_s^{eq} of -5.8 Dyne/cm. Hence, we may conclude that we did not observe systematic differences with observations that resulted from using pressure cells.

3.6   Discussion and conclusions

In this paper, we have considered the concept of non-drainable residual saturation of NAPLs in porous media, which has received little attention so far in the literature.

A careful selection resulted in 26 non-drainable residual saturation data that could be used to observe macroscale relationships from papers reporting experimentally obtained non-drainable residual NAPL saturation data. Residual saturation values range between 0.001 and 0.23. From these data only a relationship between the spreading coefficient and the residual saturation could be assessed. As has been shown in Figure 1, the value of S_{or} decreases as C_s becomes less negative. However, the levels of the different lines differ significantly, which indicates that S_{or} depends much on other properties besides the spreading coefficient. It is plausible, that properties of the porous medium such as pore size distribution and grain shape are related with the different levels of $S_{or}(C_s)$-relationships. Also in a qualitative sense, more detailed conclusions can not be made as such an aim would require a much more comparable description of the different porous media, in terms of e.g. mean pore size, variance and other (higher moment) pore size distribution statistics. In that respect, a systematic data acquisition for S_{or} as a function of C_s, or S_w, or porous medium properties, respectively, might help to assess which other factor(s) than the spreading coefficient may be hidden so prominently in the different S_{or}-levels of Figure 1. Perhaps more important, a systematic data set can help explain how

such high S_{or}-values as has been reported by Vizika and Lombard (1996) can develop in natural porous media.

An experimental set up has been developed especially to measure three-phase $P_c - S$ relationships including residual NAPL. The set up is a variant of the well known suction plate apparatus. The set up was used successfully to measure water and NAPL pressures and saturations independently. However, the experiment appeared to be very sensitive to unwanted air intrusion. Physically, we did not observe definite reasons for using a suction cell, i.e., we did not observe systematic differences with observations that resulted from using pressure cells, whereas the experimental problems with air leakage discourage the use of a suction cell, in favor of a pressure cell.

A non-drainable residual saturation of at most 0.081 is measured in the four measurements that we have conducted using the non-spreading liquid, dodecane, in a sandy porous medium. Such S_{or}-values are in the range that has been reported in the literature (Section 2). In view of the C_s-value of -5.8 Dyne/cm^2 in our experiment, the found value of S_{or} must still be regarded as relatively small compared with the data in the literature.

The experiments indicate that air entrapment increases the non-drainable residual saturation. Hence, a careful selection of the drainage and imbibition path followed in the experiments is recommended for future experiments. The sphere model analogon of Wipfler and van der Zee (2001) is not supported by the measurements concerning the effect of water on residual saturation. Also, a critical total liquid saturation that indicates the transition to non-drainable residual NAPL is not observed. This might indicate that other mechanisms are involved that are not captured by the sphere model analogon of Wipfler and van der Zee (2001). To determine whether the constitutive relationships for natural porous media of Wipfler and van der Zee (2001) need to be amended, additional experiments may be required.

Appendix A Non-drainable residual NAPL saturation reported in the literature

During the last decades various papers reported non-drainable residual NAPL measurements after gravity drainage of NAPL. We carefully selected the available data. The criteria we used are discussed below.

We selected only experiments with water-wet porous media (sand, sandstone and glass beads). In addition, water had to be at low saturation and

the water saturation should preferably be quantified. Next, the spreading coefficient should be known, or at least it should be known if the NAPL performed as a spreading liquid in the presence of water and air or as a non-spreading liquid. NAPL should not become entrapped by imbibing water. We only considered experiments with a low capillary number, i.e. fluid velocities and pressure differences had to be low to guarantee low viscous forces in comparison to capillary forces. Next, air was preferably at constant pressure, which is in agreement with the physical system in the soil after a NAPL spill. Furthermore, the displacement process/history of the data should be reported in the paper. Based on these considerations we selected a number of papers reporting residual saturation data.

Table 3.1 gives the experimental non-drainable residual NAPL saturation, S_{or}, after (gravity) drainage, of the experiments that were selected. In the table, if available, the spreading coefficient at thermodynamic equilibrium, C_s^{eq}, is given or otherwise the 'normal' spreading coefficient, C_s, is given. We assume that the liquids have had time to age during the experiment. In addition, if available, the (residual) water saturation, S_w, is given. The table contains only information provided by the papers. Hence, a NAPL used in different experiments might have different spreading coefficients in the table. Next, the reported non-drainable residual NAPL saturation, S_{or}, is given as well as the type of experiment and the type of porous medium. In the last column references are given.

The experiments are classified in three types: The first one, referred to as type 1, consists of a large column of which the NAPL is drained under the influence of gravity (also referred to as *free drainage* experiment). Two procedures can be followed: (1) a fully water-saturated column is drained by NAPL to low or residual water saturation which on its turn is drained by gas to residual saturation or (2) a column at low water saturation is first imbibed by NAPL (NAPL displaces gas) and then drained by gas to residual saturation (procedure followed only in the experiment performed by Eckberg and Sunada (1984)). Saturation is measured by gamma ray technique/ CT scanner or by extraction and chemical analysis. Pressures are measured at the in- and outlet. One paper measured saturation changes in time and calculated relative permeabilities (Sahni et al., 1998). If the calculated relative permeability was equal to zero, the liquid was supposed to be at non-drainable residual saturation. For this free drainage experiments, capillary-end effects lead to accumulation of water and NAPL above the bottom of the column. There is a saturation gradient over the height

of the column due to capillary forces. Only at a certain distance above
the bottom of the column non-drainable residual NAPL can be observed.
Experiments that considered this saturation gradient could provide useful
non-drainable residual saturation data and only those were reported in the
table.

The second type of experiment, referred to as type 2, consists of *con-
trolled drainage* using a semi-permeable membrane to prevent gas break-
through. A fully water-saturated column is drained by NAPL to residual
saturation which in turn is drained by gas to residual saturation. The re-
covery rate is measured gravimetrically or volumetrically to calculate (av-
erage) saturation. In some cases it was measured in combination with
gamma-ray technique or X-ray scanning or with extraction and chemical
analysis. Pressures are measured in the column by pressure transducers or
at the in- and outlet. For most of the experiments of this type flow is driven
externally applied pressure differences. Only in the experiments performed
by Kalaydjian (1992), the NAPL is drained by using a centrifuge.

The third type of experiment consists of a sand-filled column at low
water saturation with at both ends a gauze. NAPL is introduced via one
gauze by capillary rise. After equilibrium has been reached the column is
turned upside down and put into a beaker filled with sand. NAPL drainage
is measured gravimetrically.

nr	C_s	C_s^{eq}	S_w	S_{or}	type expt.	porous medium	reference
1	>0		0.24	0.03	2	sandstone	1
2	<0		0.24	0.03	2	sandstone	1
3	>0		0.13	0.04	1	sand	1
4	<0		0.14	0.01	1	sand	1
5	>0		0.03	0.07	1	sand	2
6	>0		0.16	0.006	2	glass beads	3
7	>0		0.15	0.01	2	glass beads	3
8	>0		0.21	0.02	2	glass beads	3
9	>0		-	0.2	2	sandstone	3
10	15.7		0.03	0.01	2	sand	4
11	-4.8		0.02	0.1	2	sand	4
12	-1.1		0.04	0.01	2	sand	4
13	>0		0.1	0.04	3	sand	5
14	8.5		0.17	0.11	1	sand	6
15	-4.5		0.13	0.23	1	sand	6
16	-4.7		0.25	0.2	2	sand	7
17	3.4	-0.5	0.06	0.001	1	sand, narrow distr.	8
18	-0.8	-1.9	0.06	0.011	1	sand, narrow distr.	8
19	-3.4	-3.9	0.06	0.015	1	sand, narrow distr.	8
20	3.4	-0.5	0.1	0.004	1	sand, broad distr.	8
21	-0.8	-1.9	0.1	0.03	1	sand, broad distr.	8
22	-3.4	-3.9	0.1	0.05	1	sand, broad distr.	8
23	-0.3		0.21	0.013	1	sand	9
24	3.5		0.11	0.012	1	sand	9
25	-3.1		0.18	0.124	1	sand	9
26	-0.3		-	0.1	1	sandstone	9

Table 3.1: Experimentally measured non-drainable residual saturation. In the columns are given the number of the experiment, the spreading coefficient, C_s and the equilibrium spreading coefficient, C_s^{eq}, the water saturation, S_w, the non-drainable residual saturation, S_{or}, the type of experiment, the type of porous medium and the references, respectively. Three types of experiments are distinguished. These are explained in the text. The following references are considered: 1. Dumoré and Schols (1974); 2. Eckberg and Sunada (1984);3. Kantzas et al. (1988);4. Kalaydjian (1992); 5. Jarsjö et al. (1994); 6. Vizika and Lombard (1996); 7. Hofstee et al. (1997); 8. Zhou and Blunt (1997); 9. Sahni et al. (1998)

References

Chatzis, I., Morrow, N.R., Lim, H.T., 1983. Magnitude and detailed structure of residual oil saturation. Society of Petroleum Engineering Journal, April, 311–326.

Dumoré, J.M. and Schols, R.S., 1974. Drainage capillary pressure functions and the influence of connate water. SPEJ (okt 1974) 437–444.

Eckberg, D.K. and Sunada, D.K., 1984. Nonsteady three-phase immiscible fluid distribution in porous media. Water Resources Research, 20(12):1891–1897.

Ferrand, L.A., Milly, P.C.D., Pinder, G.F., Turrin, R.P., 1990. A comparison of capillary pressure-saturation relations for drainage in two- and three-fluid porous media. Advances in Water Resources, 13(2),54–63.

Hirasaki, G.J.,1993. Structural interactions in the wetting and spreading of van der Waals fluids. J.Adhesion Sci.Technol., 7(3):285–322.

Hofstee, C., Dane, J.H. and Hill, W.E., 1997. Three-fluid retention in porous media involving water, PCE and air. Journal of Contaminant Hydrology, 25:235–247.

Jarsjö, J., Destouni, G. and Yaron, B., 1994. Retention and volatilisation of kerosine: laboratory experiments on glacial and post-glacial soils. Journal of Contaminant Hydrology, 17:167–185.

Kalaydjian.,F. J.-M., 1992. Performance and analyses of three-phase capillary pressure curves for drainage and imbibition in porous media. 67th Annual Technical Conference and Exhibition of the Society of Petroleum Engineers, Washington, DC, SPE 24878.

Kantzas, A., Chatzis, I.,Dullien, F.A.L., 1988. Enhanced oil recovery by inert gas injection. Proceedings of the 1988 6th SPE/DOE symposium on enhanced oil recovery, Tulsa, OK, SPE 17379.

Parker, J.C., Lenhard, R.J. and Kuppusamy, T., 1987. A parametric model for constitutive properties governing multiphase flow in porous media. Water Resources Research, 23(4):618–624.

Sahni, A., Burger, J., Blunt, M., 1998. Measurement of three phase relative permeability during gravity drainage using CT. Proceedings of the 1998 SPE/DOE Improved Oil Recovery Symposium, Tulsa, OK, SPE 39655.

Vizika, O. and Lombard, J.-M., 1996. Wettability and spreading: two key parameters in oil recovery with three-phase gravity drainage. Soc.Pet.Eng.Reservoir Eng. (feb.) 11:54–60.

Wipfler, E.L., Van der Zee, S.E.A.T.M., 2001. A set of constitutive relationships accounting for residual NAPL in the unsaturated zone. Journal of Contaminant Hydrology, 50:53–77.

Zhou, D. and Blunt, M., 1997. Effect of spreading coefficient on the distribution of light non-aqueous phase liquid in the subsurface. Journal of Contaminant Hydrology, 25:1–19.

Chapter 4

Infiltration and redistribution of LNAPL into unsaturated layered porous media*

4.1   Introduction

Infiltration of Non Aqueous Phase Liquids (NAPLs) into the subsurface is a serious environmental problem. Although NAPLs may be considered immiscible with water, they often have water solubilities that exceed water quality standards and, therefore, they may contribute to groundwater contamination. Understanding of the mechanisms that control NAPL behavior and the ability to predict the subsurface distribution of NAPL contribute to the success of remediation efforts. In this paper we study the effect of inclined layers of sand on the redistribution of a L(ight-)NAPL spill in the unsaturated zone by means of experiments and modeling. By investigating LNAPL redistribution in porous media with inclined layers we expect to increase our understanding of the effect at the intermediate scale (cm) of heterogeneities on the infiltration and redistribution of LNAPL in the unsaturated zone. An enhanced understanding of this type of heterogeneous system helps us to identify critical processes and to determine key parameters in the context of remediation strategies at the field scale.

Capillary forces play an important role in the case of multi-phase fluid flow in layered heterogeneous systems. With regard to wetting fluid displacement by the non-wetting fluid, also referred to as a drainage process, the entry pressure, i.e. the minimum capillary pressure needed for a non-wetting fluid to enter a porous medium, is of particular importance. Fine sand has a higher entry pressure than coarse sand; consequently, a non-wetting fluid will only penetrate into a fine sand layer saturated with the

wetting fluid, if the capillary pressure has been built up to the level of the fine sand entry pressure. Prior to entry, the fluid accumulates and spreads above the interface between coarse and fine sand. This mechanism can be observed for D(ense-)NAPL infiltration into water-saturated heterogeneous sand. Schwille (1988) and Kueper et al. (1989) experimentally investigated DNAPL infiltration into water-saturated heterogeneous sand, whereas Kueper and Frind (1991) used experimental data to validate their numerical multiphase flow model for DNAPL displacing water. Dekker and Abriola (2000) numerically investigated the effects of randomly distributed porous media on the infiltration of DNAPLs, while de Neef and Molenaar (1997) derived analytical solutions with regard to some specific layered geometries and steady-state infiltration of DNAPLs.

In the case of a wetting fluid imbibing a fine sand overlying a coarse sand, capillary forces will retain the fluid in the at the interface. The coarse sand layer forms a so-called capillary barrier. The wetting fluid saturation at the interface has to increase such that the capillary pressure at the interface decreases to a value at which the relative permeability of the coarse sand becomes greater than zero. Capillary barriers can be understood by observing $k_r - P_c$ relationships. Relative permeability defines the permeability reduction as a result of pore occupancy by other fluids and the effect of inaccessible pores to the fact that they are occupied by other fluids. Next, viscous resistance due to the other fluids in the pores is accounted for. Relative permeability depends on fluid saturation, and consequently, on capillary pressures between fluids.

In Figure 4.1, for a two-phase system, examples of relative permeability are given as a function of capillary pressure for two types of sands; coarse grained sand and fine grained sand. We used $k_r - P_c$ relationships and porous medium characteristics as mentioned in Sections 4.2.1 and 4.2.2. With regard to decreasing the capillary pressure head, $P_{cnw}/(\rho_w g)$ (imbibition process), the figure shows that wetting fluid relative permeability increases, of which the fine sand relative permeability, $k_{rw}(fine)$, increases in an earlier stage than the coarse sand relative permeability, $k_{rw}(coarse)$. For a certain capillary pressure, the coarse sand relative permeability is negligible as compared to the fine sand relative permeability. This is the well-known capillary barrier concept. The wetting fluid accumulates and spreads on top of a coarse sand layer. Capillary barriers have been studied extensively with respect to water infiltration into dry sand (an overview of capillary barrier theory was provided by Schroth et al. (1998)). Entry
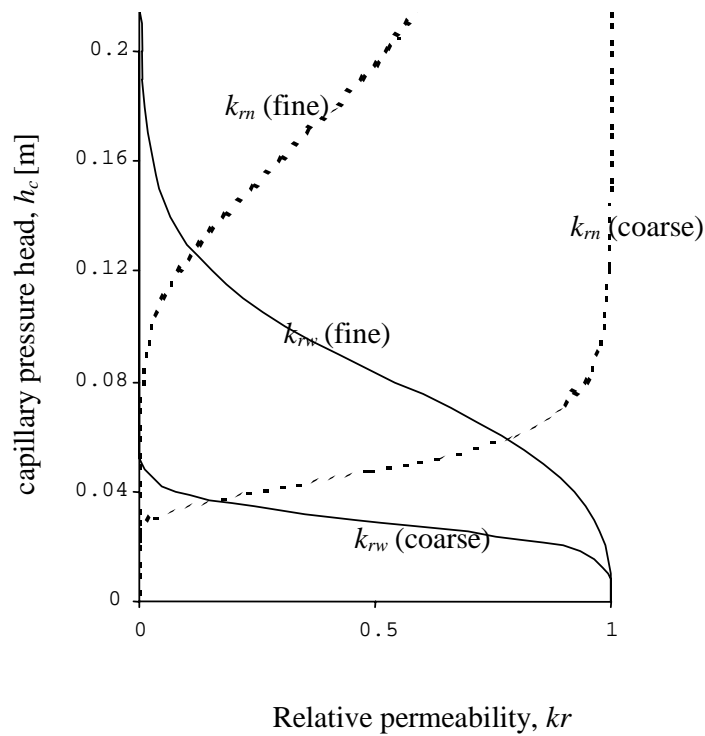
Figure 4.1: Wetting and non-wetting relative permeability related to the capillary pressure head $h_c = P_{cnw}/\rho_w g$ for fine and coarse sand. We used the $k_r - S$ relationships and the porous medium properties given in Sections 4.2.1 and 4.2.2. k_{rw} has a limit for flow in coarse layer at approximately $h_c = 0.05$ m. k_{rn} has an entry pressure for coarse sand at approximately 0.03 and for fine sand at approximately 0.08.

pressure effects can also be observed in the figure. With regard to increasing capillary pressure head (drainage process) the figure shows that the non-wetting fluid relative permeability increases, of which the coarse sand relative permeability, k_{rn}(coarse), starts to increase at an earlier stage than the fine sand relative permeability, k_{rn}(fine). This implies that a minimum capillary pressure is required for the non-wetting fluid to infiltrate into the porous medium. This pressure is higher for the fine sand.

In addition to capillary forces, the balance between the capillary and gravity forces is also of importance. This balance defines the horizontal spreading of the LNAPL at the interface and the occurrence of fingers due to instabilities of a wetting front (Glass et al., 1989).

In this paper we consider three phases; water, LNAPL and air. Water is the wetting fluid, LNAPL is the intermediate wetting fluid and air is the non-wetting fluid. Kessler and Rubin (1987); Schroth et al. (1998); Walser et al. (1999); Hofstee et al. (1998) suggest to consider infiltrating NAPL into layered unsaturated soil as an imbibition process, i.e. NAPL displacing only air. Hence, NAPL will only be retained above a capillary barrier. However, this assumption should be used with caution when the NAPL approaches a water saturated zone.

Our objective is to clarify the effect of the dominating processes during LNAPL infiltration into the vadose zone. For this purpose, we conducted intermediate-scale laboratory experiments to visualize the effect of changes in the dominating processes, i.e. changes in discontinuities of relative permeability and the changes of the relative permeabilities along the sloping layers. Furthermore, since numerical multi-phase flow models should be validated to experimental and field data before being used as a predictive tool for remediation purposes, we tested whether numerical multiphase flow models are able to simulate the functional transition of the interfaces between layers, by comparing the observed experimental LNAPL contours to the contours predicted by the finite difference numerical multi-phase flow code STOMP (White and Oostrom, 1996). Various studies have been performed to validate multi-phase flow models. This model as well as other multi-phase flow models. For example, Lenhard et al. (1995) successfully tested STOMP against hysteretic and non-hysteretic data from a three-phase flow 1-D experiment describing fluid saturation under conditions of a fluctuating water pressure. van Geel and Sykes (1994) also modeled a three-phase flow experiment focusing on the need to account for hysteresis. Hofstee et al. (1998) performed validation experiments, which revealed that

STOMP captures DNAPL infiltration into a fine sand layer in the vadose zone. However, no model validation has been done for inclined layers in the unsaturated zone with a horizontal watertable. We also performed sensitivity analyses with the numerical model in order to systematically explore 2-D LNAPL migration.

4.2 Materials and methods

4.2.1 Experiments

Two two-dimensional laboratory experiments were performed. For the first experiment the porous medium consisted of a fine sand matrix and a coarse sand layer, whereas for the second experiment the porous medium consisted of a coarse sand matrix and a fine sand layer. Both layers were inclined with respect to the watertable. An LNAPL finite point source was imposed on top of the sandy porous medium and left to redistribute.

Equipment and materials

A Plexiglas chamber measuring 40 cm x 40 cm x 2.5 cm was constructed for the purpose of the experiments, with vertical side wells to control the input and output of water. Figure 4.2 shows the main features of the experiment. The chamber was placed in a room which was kept at 18° C. Artificially crushed white sand was used as the porous medium (AWK, Germany). The grain size range of the well-graded quartz sand mixtures was 0.7-1.2 mm for the fine sand and 1.0-1.8 mm for the coarse sand. Grain sizes were sufficiently small as compared to the thickness of the chamber to allow for a continuum model approach, since generally approximately 15 pores are needed for the network models (e.g. Steele and Nieber (1994)). We used tap water to saturate the sands. The insoluble Jet-fuel A-1 (Statoil, Norway) with density 0.8 g/cm^3 and viscosity 0.0019 Pa s was used as the infiltrating LNAPL in the experiments. To enhance the contrasts between the fluids a yellow dye (Fluoroscein) was added to the water and red dye (Sudan IV) was added to the LNAPL. The surface tension of Jet-fuel A-1 dyed with Sudan IV was measured with a ring tensiometer and was 0.032 N/m. The surface tension of water we took from literature: 0.073 N/m (Weast, 1985) and since Jet-fuel A-1 is considered a spreading liquid, the interfacial tension between Jet-fuel A-1 and water is assumed to be less than 0.073-0.032=0.041 N/m.
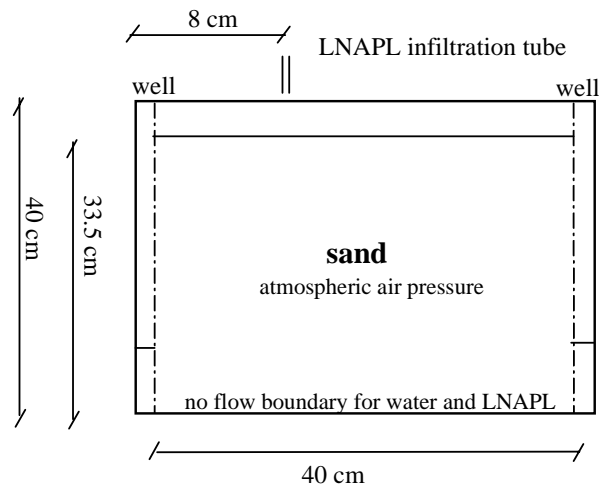
Figure 4.2: Experimental domain and boundary conditions. A total amount of 15 ml LNAPL was added through the tube. At the wells a fixed water pressure head was maintained.

Sample preparation

The plexiglass chamber was filled with water and subsequently sand was added through a funnel until a height of 33.5 cm of the sand matrix was achieved. The chamber was tilted during the filling in order to obtain tilted layers. Two types of sand configurations were studied; one coarse matrix with a fine sand layer and one fine matrix with a coarse sand layer. Both layers had a thickness of 4 cm and where located in the unsaturated part of the sand. The lowest part of the inclined layer ended in the capillary fringe of the host medium. The coarse layer was tilted at a 22° angle and the fine layer was tilted at a 28° angle. After the packing was finished, the model was allowed to remain saturated for several hours prior to draining the water until a watertable was reached at 10 cm above the bottom of the model. During the next 12 hrs no outflow of water was measured, and water was considered at steady state and at hydrostatic pressure.

Experimental procedure

LNAPL was introduced at the upper surface of the unsaturated sand, 8 cm to the left of the center of the chamber. A total amount of 15 ml LNAPL was added drop-wise to the packed sand through a tube at an infiltration rate of 1.875 ml min^{-1} for the coarse layer experiment and 1.5 ml min^{-1} for the fine layer experiment using a peristaltic pump. The water level was kept at a fixed pressure head in the wells. The LNAPL redistribution was studied by means of digital pictures taken with a digital camera at pre-defined time intervals. The LNAPL spill was left to redistribute until no LNAPL movement could be observed for 12 hrs. The coarse layer experiment was stopped after 1110 min and the fine layer experiment was stopped after 1440 min.

Measurement and analysis of hydraulic parameters

In order to define the hydraulic parameters of the two sand types we performed multi-step outflow analyses using an inverse modeling approach (van Dam et al., 1994). The multi-step outflow analysis is a variant of the one-step outflow method which was originally developed by Kool et al. (1985). In a multi-step outflow experiment a soil sample is placed in a pressure cell on top of a saturated ceramic plate with a relatively high hydraulic conductivity and a high entry pressure for air. The soil sample is initially saturated with water (the wetting fluid) introduced through the ceramic

plate at the bottom. Next, the pneumatic air pressure (non-wetting fluid) is gradually increased from above and water outflow through the plate is measured. The inverse model solves the objective function based on the head-based form of the Richards equation. We refer to van Dam et al. (1994) for a detailed theoretical development.

We adapted the multi-step outflow experiment for application to the Plexiglas chamber. Instead of increasing the air pressure we gradually decreased the water pressure at the bottom of the chamber and measured the outflow. In order to be able to perform the experiment we had to replace the bottom of the chamber by a horizontal well on which a constant head was imposed. Two experiments were performed. In the first experiment the chamber was filled with fine sand, whereas in the second experiment the chamber was filled with coarse sand. Initially, the chamber was fully water saturated and then the water pressure head was decreased in 5 or 6 steps. This took approximately 15 hrs. As the bottom of the chamber was continuously saturated, no ceramic plate was needed to prevent air entry. Although measuring the outflow at near saturation might yield less accurate results due to non-uniform flow (van Dam et al., 1994), the advantage of this approach is that a similar packing technique is achieved for determination of the hydraulic parameters as for the experiments because both packing technique and chamber are the same. Starting from the total volume of water that was introduced in the chamber (1160 ml for the fine sand and 1090 ml for the coarse sand) we calculated the porosity, ϕ, to be 0.55 and 0.52 for the fine and the coarse sand respectively. Furthermore, the (vertical) hydraulic conductivity, K, was derived by means of flow rate measurements in water saturated sand, i.e. 0.05 cm/s $\pm$ 0.007 and 0.09 cm/s $\pm$ 0.015, respectively. We fixed the porosity and the conductivity and the inverse model (van Dam et al., 1994) optimized for three parameters: the residual saturation, S_{rw}, and the van Genuchten parameters α, n. Mean values and 95 % confidence intervals are given in Table 4.1, the water-air Pc-S curves are given in Fig. 4.3. The optimized hydraulic functions are applied in the numerical model. With regard to the coarse sand, physically, zero residual water saturation is not realistic, however, to be consistent we used the exact values of the multi-step analysis for the numerical simulation.

	fine sand	coarse sand
ϕ	0.55	0.52
K [cm s^{-1}]	0.05 ± 0.007	0.09 ± 0.015
S_{rw}	0.19 ± 0.04	0 ± 0.006
n	3.9 ± 0.4	5.9 ± 3
α [m^{-1}]	8 ± 0.6	27 ± 4.5

Table 4.1: Hydraulic properties of the fine and coarse sand used in the experiments: the porosity, ϕ, the hydraulic conductivity, K, residual water saturation, S_w, and the van Genuchten parameters, α and n. For K the standard deviation is given and for S_w, n and α the 95 % confidence interval is given.
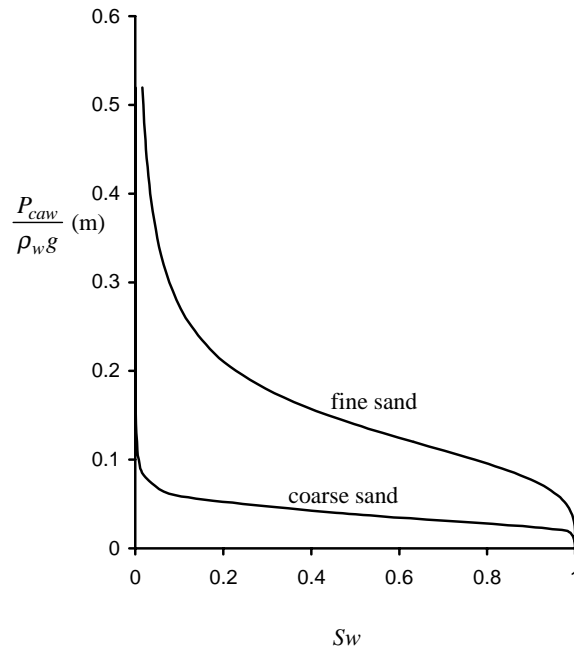

Figure 4.3: (Effective) water-air $P_c - S$ curves for coarse and fine sand resulting from the multi-step outflow analysis. We refer to Table 4.1 for the hydraulic parameters.

4.2.2   Numerical model

The experiments were simulated with the 3-D integrated finite difference multiphase flow code STOMP, using fully implicit time differencing (White and Oostrom, 1996). We assumed that each sand layer is isotropic, that both fluids are incompressible and immiscible and that air is infinitely mobile at constant pressure ($P_a = 0$) and with saturation S_a. The governing equations for the flow of water (w) or LNAPL (o) are the mass balance equation

$$\phi \frac{\partial \overline{S}_i}{\partial t} + \nabla \cdot u_i = 0 \qquad i = w, o \tag{4.1}$$

and the flux equation

$$u_i = \frac{\mathbf{k} k_{ri}}{\mu_w} \nabla (P_i + \rho_i g z), \tag{4.2}$$

where u_i is the Darcy flux of phase i, and ϕ is the effective porosity, $\mathbf{k}$ is the intrinsic permeability tensor, $\overline{S}_i$, k_{ri}, μ_i, p_i and ρ_i are respectively the effective saturation, the relative permeability, the viscosity, the pressure and the density of phase i. g is the gravitational acceleration, z is the elevation and t is time. The set of equations is completed by the constitutive relations

$$\overline{S}_w + \overline{S}_o = \overline{S}_t \quad \text{and} \tag{4.3}$$
$$\overline{S}_t + \overline{S}_a = 1. \tag{4.4}$$

$\overline{S}_i$ are effective saturations that are defined by

$$\overline{S}_w = \frac{S_w - S_{wr}}{1 - S_{wr}}, \quad \overline{S}_o = \frac{S_o}{1 - S_{wr}}, \quad \overline{S}_t = \frac{S_t - S_{wr}}{1 - S_{wr}}, \quad \overline{S}_a = \frac{S_a}{1 - S_{wr}} \tag{4.5}$$

where S_{wr} is the residual water saturation and $\overline{S}_t$ is the effective total liquid saturation. The pressure difference at the interface between the different fluid phases is $P_{cij} = P_i - P_j$, where P_{cij} is the capillary pressure between the phase i and j ($i, j = w, o, a$). We assumed that fluid wettability of the sand matrix follows the sequence water > LNAPL > air, S_t is a function of P_{cao} and S_w is a function of P_{cow} (Leverett, 1941). The use of the latter assumption makes it possible to obtain three-phase capillary pressure relations from more readily measurable water-air relations. The $P_c - S$ relations are described by scaled variants of the empirical function of van Genuchten (1980) (Parker et al., 1987). For the 2-phase air-water

system the following relationship applies

$$\overline{S}_w = \left[1 + \left(\alpha\frac{P_{caw}}{\rho_w g}\right)^n\right]^{-m},$$ (4.6)

where α and n are porous medium properties and $m = 1 - 1/n$. If $P_{caw} \leq 0$ we have $S_w = 1$. The three-phase air-oil-water system is defined by

$$\overline{S}_w = \left[1 + \left(\alpha\beta_{ow}\frac{P_{cow}}{\rho_w g}\right)^n\right]^{-m}$$ (4.7)

together with

$$\overline{S}_t = \left[1 + \left(\alpha\beta_{ao}\frac{P_{cao}}{\rho_w g}\right)^n\right]^{-m}.$$ (4.8)

If $P_{cow} \leq 0$ we have $\overline{S}_w = 1$ and if $P_{cao} \leq 0$ we have $\overline{S}_t = 1$. β_{ao} and β_{ow} are the scaling coefficients, where $\beta_{ow} = \frac{\gamma_{aw}}{\gamma_{ow}}$, $\beta_{ao} = \frac{\gamma_{aw}}{\gamma_{ao}}$ and $\beta_{aw} = 1$. γ_{ij} is the interfacial tension between fluid i and j. The Van Genuchten $P_c - S$ relationships were chosen over the often applied Brooks and Corey relationships (Brooks and Corey, 1966). The main difference between the two models is that Brooks and Corey account for a distinct entry pressure. One can question the use of the van Genuchten model because for laboratory sands a distinct entry pressure is expected. However, the van Genuchten model is a good alternative for this calibration exercise because the use of the model will only lead to a small overestimation of the LNAPL saturation near the capillary fringe. For the relative permeability, k_r, we apply the relationships proposed by Mualem (1976):

$$k_{rw} = \overline{S}_w^{1/2}[1 - (1 - \overline{S}_w^{1/m})^m]^2,$$ (4.9)

$$k_{ro} = (\overline{S}_t - \overline{S}_w)^{1/2}[(1 - \overline{S}_w^{1/m})^m - (1 - \overline{S}_t^{1/m})^m]^2.$$ (4.10)

No data with regard to residual saturation of LNAPL and air were available. Therefore, and to keep the model simple and comprehensive, hysteresis is not included (no entrapment). During the LNAPL infiltration process, air may become entrapped by LNAPL. Consequently, NAPL relative permeabilities may be higher in the model as compared to the experiment.

The set of equations was solved with a multivariable, residual-based Newton-Raphson iteration technique. The constitutive relations were computed numerically. Upwind interfacial averaging was used for the relative permeabilities, whereas harmonic averaging was used for the other components. Further details of the simulator can be found in White and Oostrom (1996).
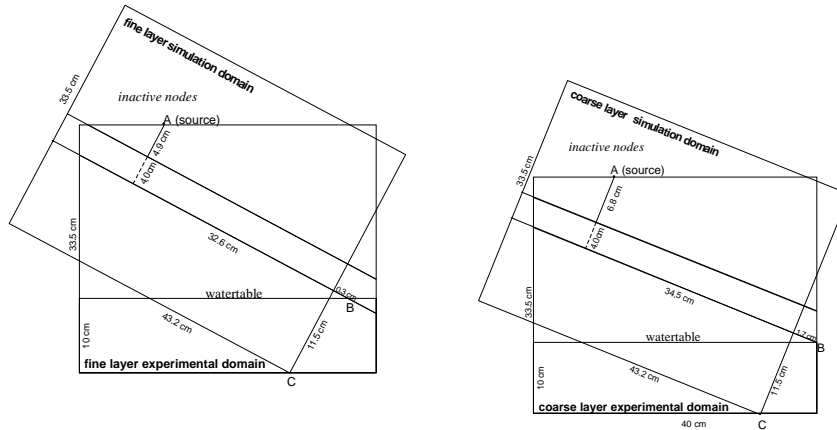
Figure 4.4: Simulated domains in relation to experimental domains for coarse layer and fine layer experiment

4.2.3   Model simulation

We assumed 2-D flow behavior in the chamber which was confirmed by preliminary model calculations, i.e. the saturation profiles showed no difference between a line source and a point source. The domain of the numerical model was rotated 22° compared to the horizontal for the coarse layer and 28° for the fine layer. Hence, the layer was not inclined as compared to the bottom of the Plexiglas chamber as in the experiment, but the entire domain was rotated. The STOMP simulator allows for rotation of the direction of gravity as compared to the grid. Because we dealt with a rectangular grid of a finite difference scheme, this was more convenient and it saved CPU time compared to a horizontal domain with a tilted layer. The 4 cm horizontal layer was situated at 11.5 cm above the bottom of the domain (see Fig. 4.4). Due to the rotated domain, the boundary conditions of the numerical model approximation differed from those of the experiment. Therefore, in the simulation, some LNAPL was observed outside the experimental domain. In order to be able to cover the main LNAPL infiltrated area, we defined a model domain slightly larger than the experimental domain (43.2 cm length, 33.5 cm height and 2.5 cm depth).

With regard to water, impermeable boundaries were assumed at all sides of the domain, except for 1.5 cm at the lower right corner (point C) that had prescribed water pressure allowing for drainage of water at the beginning of the simulation. With regard to LNAPL, impermeable boundaries were assumed as well, except for the left-hand and the right-hand side boundary on which a hydraulic gradient was imposed that enables the outflow of LNAPL on top of the capillary fringe to the right. Furthermore, above the LNAPL source nodes were assigned to be 'inactive' (gray shaded area). This implies that these nodes do not conduct fluids, and therefore, the boundary to the inactive nodes acts as an impermeable boundary.

Initially, prior to introducing LNAPL, the domain was water-saturated with a prescribed water pressure head of 48.7 cm at the lower right corner. Water was allowed to drain by gradually decreasing the prescribed pressure head at point C to a value of 10.0 cm. Water drainage was modeled until static equilibrium was reached. The model results were used as the initial conditions for the LNAPL spill simulations. Subsequently, LNAPL was introduced from a point source that was located at a distance and angle to the layer similar to those in the experiment (see Fig. 4.4). As in the experiment, 15 ml LNAPL was introduced in 8 min for the coarse layer and 10 min for the fine layer. The 2-D computational domain consisted of 5950 cells. The grid was refined near the LNAPL source, near point C and around the layer. The horizontal and vertical grid spacing varied from $\Delta x = 0.7$ cm and $\Delta z = 0.58$ cm to $\Delta x = 0.12$ cm and $\Delta z = 0.4$ cm near the LNAPL source. Use of a finer discretization was precluded by the computational demands. Hence, we were not able to check the accuracy of the discretization.

We used the porous medium and fluid properties obtained from the independent hydraulic parameters experiment. The hydraulic parameters are given in Section 4.2.1. We assumed the hydraulic conductivity to be isotropic. With regard to water, a density of 1000 kgm^{-3} and a viscosity of 0.001 Pa s were used whereas, with regard to LNAPL, we applied a density of 800 kgm^{-3} and a viscosity of 0.0019 Pa s. LNAPL saturation was calculated at time intervals similar to the time intervals between the pictures of the experiment. The LNAPL spill was modeled for a period of 1110 min for the coarse layer experiment and 1440 min for the fine layer experiment. The model contours were compared to the contours taken from the pictures of the experiment. We considered saturation lower than 0.02 as invisible.

4.3   Results

4.3.1   Experimental observations and simulation results

The LNAPL contours of both the experiments and the simulations are shown in Fig. 4.5 and 4.6 for a sequence of time steps for the coarse and the fine layer, respectively. The horizontal line in the figures indicates the watertable, whereas the diagonal lines indicate the interfaces between sand types.
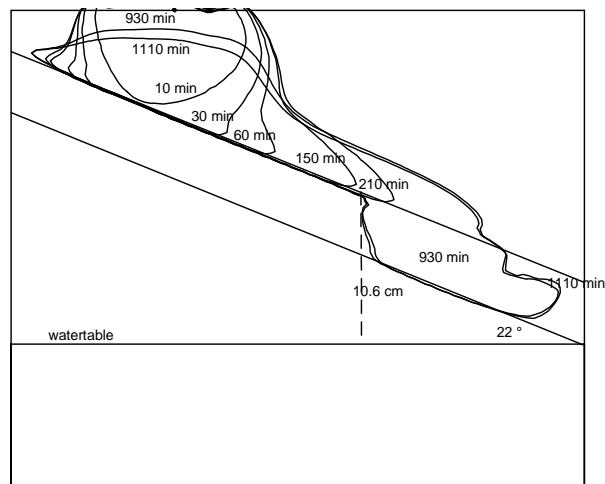
Coarse layer experiment

In general, with respect to the coarse layer the contour profiles of both the experiment and the simulation show comparable qualitative behavior (Fig. 4.5). Following application at the upper surface of the sand box, LNAPL immediately begins to infiltrate downward. Between $t = 10$ min and $t = 30$ min the coarse layer is reached and LNAPL spreads laterally to the right along the upper coarse-fine interface. This interface apparently acts as a capillary barrier to the LNAPL. Lateral spreading causes reduction of the LNAPL pressure above the interface. Consequently, the LNAPL is not able to overcome the resistance caused by the coarse layer and continues to move to the right. In the simulation, LNAPL also moves slightly to the left along the interface, which does not take place in the experiment. This indicates that in the simulation, capillary forces in the fine sand are stronger. When the LNAPL reaches the capillary fringe of the fine sand, relative permeability decreases to zero and the LNAPL accumulates. Due to this accumulation, the capillary pressure between the water and the NAPL phase is decreased and eventually declines to a value where the (now non-wetting) LNAPL relative permeability of the coarse layer is greater than in the fine layer. Then, LNAPL infiltrates into the coarse layer. Both the simulation and the experiment show LNAPL infiltration into the coarse sand at almost the same distance above the water level (10.6 cm and 9.3 cm respectively). Once inside the coarse layer, the liquid is not able to move out of it, i.e. the fine sand matrix is water saturated, and therefore, it forms a barrier to sideward flow. Hence, the presence of the inclined coarse sand layer causes the LNAPL spill to move downward along the inclination. At a certain distance above the watertable it infiltrates into the coarse sand and becomes trapped between the surrounding fine sand.

The overall agreement between experimental and simulated results is fairly good, although there are some differences. After $t = 930$ min, no

LNAPL movement can be observed in the experiment, though the liquid might still be moving within the observed contours, but in the model simulation, LNAPL is still moving. At $t = 930$ min, the LNAPL has drained out of the area near the LNAPL source, whereas in the experiment LNAPL is no longer moving visibly. This might indicate that in the experiment it is at non-drainable residual saturation (Wipfler and van der Zee, 2001; Hofstee et al., 1998) and that the simulation would improve if non-drainable residual saturation were included into the STOMP simulator. In the fine sand, the simulated LNAPL moves slower than the LNAPL in the experiment. One would expect, however, that by not including air entrapment into the model, relative permeability will be overestimated and LNAPL will move faster. The modeling results do not show this. Furthermore, the lateral spreading of the LNAPL is greater for the simulation than in the experiment. Both differences may indicate that capillary forces are stronger in the simulation. Finally, due to end effects, the LNAPL in the experiment cannot flow to the side wells because it is retained in the sand as a result of capillary forces. In the simulation, LNAPL does not reach the right boundary at this time.
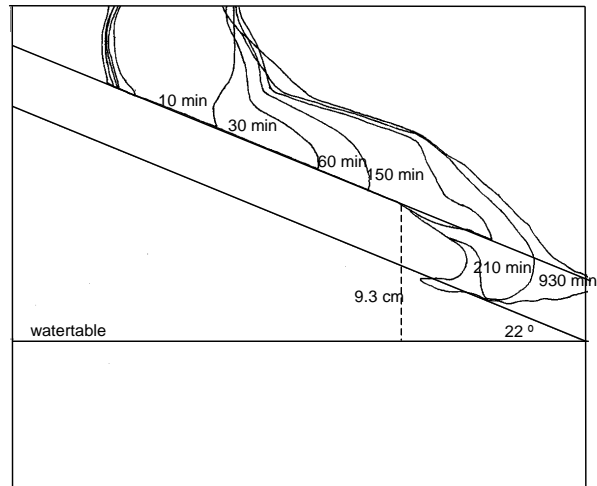
(a) Experiment

(b) Simulation

Figure 4.5: Saturation contours for coarse-sand layer in fine-sand matrix for
(a) the experiment and (b) the numerical simulation. Contours are given for each
time interval. The distance between the watertable and the height at with the
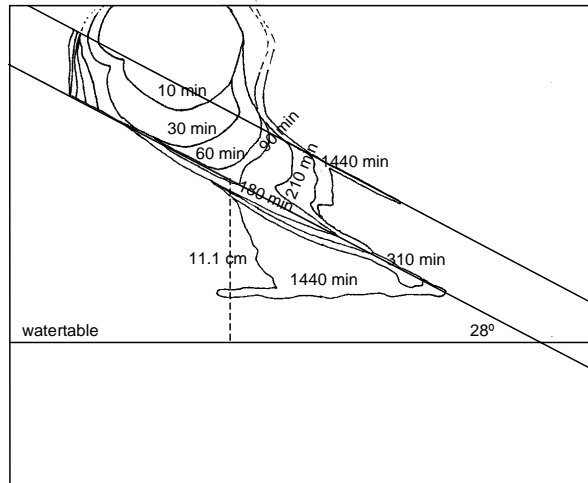LNAPL infiltrates into the coarse layer is indicated (dashed line).
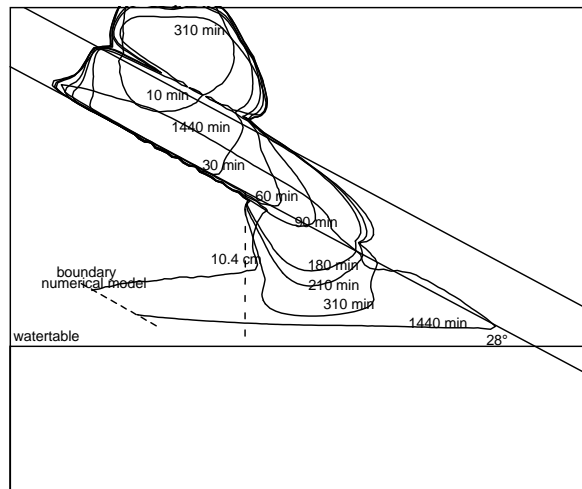
(a) Experiment

(b) Simulation

Figure 4.6: Saturation contours for fine-sand layer in coarse sand matrix for (a) the experiment and (b) the numerical simulation. Contours are given for each time interval. The distance between the watertable and the height at with the LNAPL infiltrates into the coarse layer is indicated (dashed line).

Fine layer experiment

The fine layer experimental contours are simulated accurately by the numerical model (Fig. 4.6). As the coarse sand matrix has a higher conductivity than the fine sand matrix, the LNAPL spill initially moves faster than in the previous experiment. Although it is not indicated in the figure, fingering at the LNAPL front is observed in the coarse sand. In the coarse sand, capillary forces are not able to stabilize the wetting LNAPL front instability caused by gravitational forces and small heterogeneities. The numerical model does not allow for fingering. However, fingering apparently does not change the general LNAPL behavior because the simulated shape of the LNAPL contaminated area resembles the experimental shape. The fine layer was reached prior to $t = 10$ min. The interface of the coarse sand below the fine layer acts as a capillary barrier to the LNAPL. Therefore, LNAPL is displaced downward and to the right inside the fine layer. Below, the water saturation is higher. LNAPL continues to move until the relative permeability decreases on account of the increase in water saturation, thereafter it accumulates. Next, due to the increase of the LNAPL pressure, the relative permeability ratio changes in favor of the coarse-sand relative permeability. LNAPL infiltrates into the coarse layer and a lens is formed on top of the capillary fringe of the coarse sand. Again, for the simulation and the experiment, LNAPL infiltrates into the coarse sand at the same distance above the water level (10.4 cm for the simulation and 11.1 cm for the experiment). When it has infiltrated into the coarse sand, the LNAPL lens is trapped below the fine sand layer. The LNAPL lens does not flow back into the fine layer because this layer is saturated with water. At $t = 1440$ min in the simulation, the LNAPL reaches the (rotated) bottom of the no-flow boundary and it is not able to move out of the simulated domain. This behavior differs from experimental behavior that allowed for sideward movement.

Summarizing, the presence of the fine sand layer causes the LNAPL to move laterally in the fine sand. Finally, it infiltrates into the coarser sand matrix (at a fixed distance above the water level) where it is trapped below the fine sand layer. The most pronounced difference between the experimental contours and the simulated contours can be seen at the $t = 1440$ min contour. In the experiment the total contaminated volume until $t = 1440$ min remains contaminated, whereas in the model simulation, LNAPL has drained out of the area near the LNAPL source. The difference again can be attributed to non-drainable residual LNAPL. Further-

more, the simulation shows a more pronounced breakthrough to the coarse sand. Breakthrough takes place in an earlier stage than in the experiment. In the experiment preferential flow paths are formed along the coarse-fine interface and fingers can be observed in the coarse sand caused by small heterogeneities along the interfaces in the experiment. These fingers do not occur in the simulation. It is common that fingers occur along the interface between fine and coarse sand as the conductivity of the sand increases abruptly (Glass et al., 1989). Finally, the simulated LNAPL infiltrates deeper into the capillary fringe than the LNAPL in the experiment. This may be attributed to the fact that we use the Van Genuchten model for the $P_c - S$ relationships, and therefore, we do no account for a distinct entry pressure. This implies that LNAPL can move deeper into the capillary fringe. The deeper penetration of the simulated LNAPL can also be attributed to the fact that no non-drainable residual LNAPL is held up in the simulation.

Discussion

Comparison between the three-phase continuum model simulation and the intermediate-scale experiment showed that the model is able to simulate the effects of inclined sandy layers on the infiltration of LNAPL in the unsaturated zone. Although hydraulic parameters are measured independently, the shapes of the LNAPL contaminated areas are very similar. Also, the applied assumptions appear to be appropriate. Both barriers and effects of entry pressures can be observed perfectly in the experiments as well as in the simulations. Even though the experiment shows some front instabilities in the coarse sand, this does not affect the LNAPL overall behavior. The small differences between the experimental contours and the simulations may be attributed to the fact that the capillary forces in the fine sand are stronger in the simulation and non-drainable residual LNAPL saturation is not accounted for. Neglecting air entrapment did not seem to have a major effect on LNAPL flow. However, conclusions can not be drawn since we only compared fluid contours.

4.3.2 Sensitivity analysis

The numerical model is able to simulate the interaction between the capillary forces and gravitational forces at inclined fine-coarse interfaces. We questioned the effect of small changes in the balance between these forces

Case	α_c [m^{-1}]	inclination [°]	infiltration rate [ml min^{-1}]
1	27	22	1.875
2	27	22	3.75
3	14	22	1.875
4	41	22	1.875
5	27	16	1.875
6	27	28	1.875

Table 4.2: Numerically varied parameters of the sensitivity analysis for the coarse sand layer in a fine sand matrix.

on the LNAPL behavior. In particular, with regard to remediational purposes, the distance above the watertable at which the LNAPL infiltrates into coarse sand is of interest. Because parameters can be varied easily in the model, we performed the sensitivity analysis numerically.

For the sensitivity analysis we used the coarse layer in the fine sand matrix scenario as the reference case and we varied three parameters; the LNAPL infiltration rate, the capillarity contrast at the fine to coarse interface, and the inclination of the layer. To study the effect of the capillarity contrast we only varied the Van Genuchten porous medium parameter, (α_c) of the coarse sand. For the variation of the slope we kept the distance from the source (Fig. 4.3, point A) to the coarse layer constant (6.8 cm), as well as the distance from the intersection of the watertable to the coarse layer (point B). Hence, in all cases the travel distance of the LNAPL along the interface to the capillary fringe of the fine sand was equal. In Table 4.2 the varied parameters are summarized. Case 1 is the original simulation as described in the preceding sections. Saturation profiles are given in Fig. 4.7 to 4.11.

Increasing the total LNAPL infiltration rate from 15 ml to 30 ml (3.75 cm min^{-1}) results in faster movement and a broader contaminated area (Fig. 4.7) compared with the reference case (Fig. 4.5). However, the elevation above the groundwater level where the liquid infiltrates into the coarse layer is hardly affected by the larger amount of liquid (10.4 cm instead of 10.6 cm in Case 1). The liquid moves deeper into the coarse layer than in the reference case. In conclusion, the final LNAPL distribution is not very sensitive to the total infiltration rate. If the capillarity contrast is less, the LNAPL will infiltrate relatively soon into the coarse layer, i.e. the capillarity contrast is not enough to resist the LNAPL flow at the interface
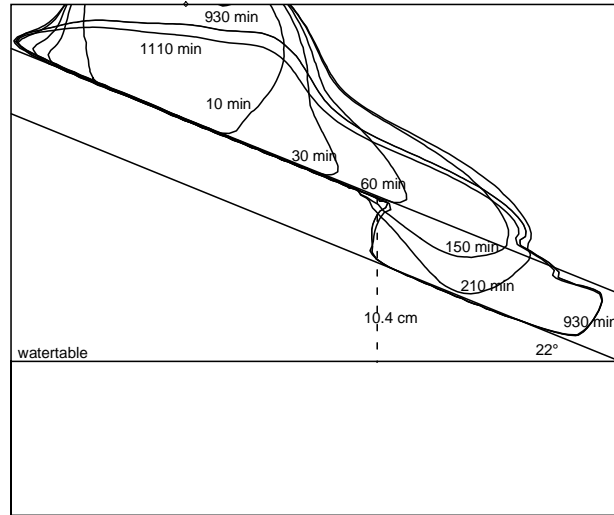
Figure 4.7: 0.02-saturation contours case 2 for $t = 10$ min to $t = 1110$ min, increased infiltration rate.

(Fig. 4.8).

This implies that LNAPL is displaced to a lesser degree in the sideward direction and that it is not trapped between the saturated fine sand layers. Greater contrast has minor effects on the LNAPL redistribution (Fig. 4.9). The LNAPL velocity along the interface is equal to the reference case, however, LNAPL intrudes at a lower level into the coarse sand, i.e. the capillary resistance against infiltration in the coarse sand is higher. This implies that the model results are sensitive to the capillarity contrast, especially with regard to minor capillarity contrasts.

Variation of the inclination of the layer (Fig. 4.10 and 4.11) shows that the vertical elevation of infiltration into the coarse layer is almost equal to the reference case , i.e. LNAPL infiltrates at an elevation above the water table of 9.7 cm and 10.8 cm for Case 5 and Case 6, respectively.

4.4   Summary and conclusions

Two laboratory 2-D experiments were carried out in a sand-filled chamber in order to qualitatively describe LNAPL infiltration in the case of inclined layers of unsaturated sand. One experiment contained a fine sand matrix

Figure 4.8: 0.02-saturation contours case 3 for $t = 10$ min to $t = 1110$ min, decreased α_c.
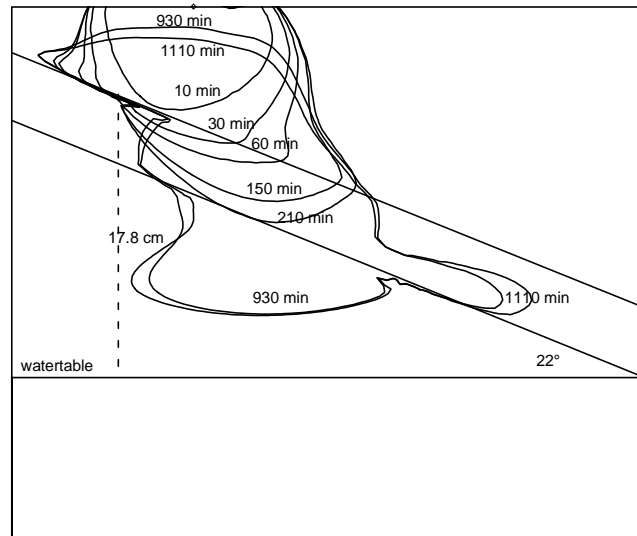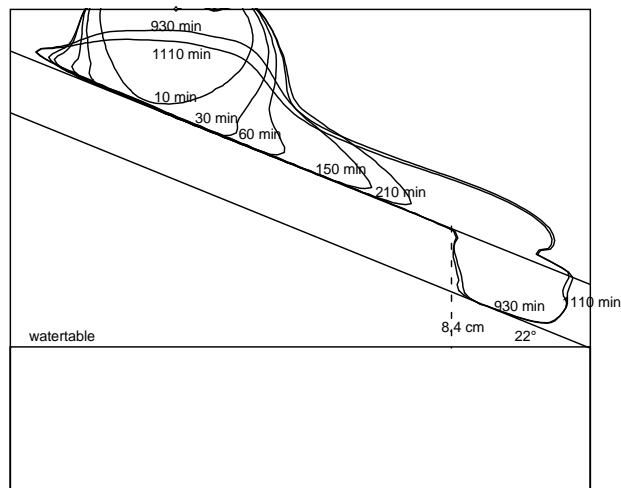

Figure 4.9: 0.02-saturation contours case 4 for $t = 10$ min to $t = 1110$ min, increased α_c.
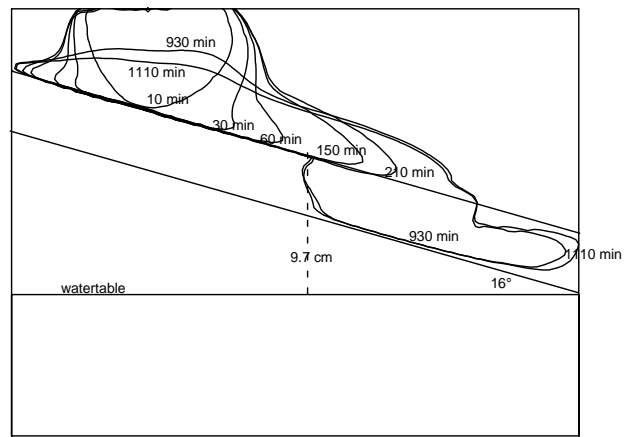
Figure 4.10: 0.02-saturation contours case 5 for $t = 10$ min to $t = 1110$ min, inclination of the coarse sand layer is $16°$.
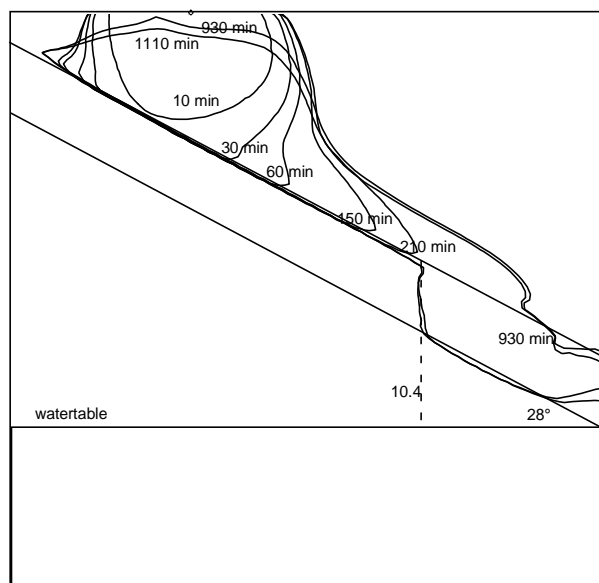

Figure 4.11: 0.02-saturation contours case 6 for $t = 10$ min to $t = 1110$ min, inclination of the coarse sand layer is $28°$.

and a coarse sand layer, whereas the other experiment contained a coarse sand matrix and a fine sand layer. The experiment with the coarse sand layer showed after LNAPL release, spreading above the coarse sand layer and movement along the interface downward to the side. At a certain distance above the watertable, it infiltrates into the coarse sand and becomes 'trapped' between the fully saturated finer sand borders. The experiment with the fine sand layer showed after release that the LNAPL experiences almost no resistance at the coarse to fine sand interface and infiltrates into the fine sand. The liquid moves downward inside the fine sand layer and infiltrates at a certain distance above the watertable to the coarse sand below, where it again becomes 'trapped' between the fine sand borders. The LNAPL behavior can be understood by considering that LNAPL might encounter two types of barriers. On the one hand, it may accumulate and spread above a coarse sand layer, that has a low water saturation and, that acts as a capillary barrier for the LNAPL before it may infiltrate into the layer. An on the other hand, it may accumulate and spread above a water saturated fine sand layer that has a high entry pressure for the infiltrating LNAPL.

The LNAPL contours obtained from numerical three-phase flow simulations agree well with the experimentally obtained contours. Despite the fact that hydraulic parameters are measured independently and air entrapment is not incorporated in the model, the shapes of the LNAPL contaminated areas are very similar. Even though fingering occurs at the micro scale, this process does not affect the overall LNAPL movement. Differences between the simulation and the experiment can be attributed to stronger capillary forces in the simulation and the fact that non-drainable residual LNAPL is not accounted for.

Sensitivity analysis performed with the numerical model shows that the qualitative LNAPL redistribution is mainly subject to the capillarity contrast between sands. A greater contrast gives more horizontal migration. The infiltration into the coarse sand layer always occurs at the same vertical level as compared to the watertable for various inclinations and various initial fluxes.

References

Brooks, R.H. and Corey, A.T.,1966. Properties of porous media affecting fluid flow. Journal of Irrigation and Drainage Division, 92:61–88.

Dekker, T.J. and Abriola, L.M., 2000. The influence of field-scale heterogeneity on the infiltration and entrapment of dense non-aqueous phase liquids in saturated formations. Journal of Contaminant Hydrology, 42:187–218.

de Neef, M.J. and Molenaar, J., 1997. Analysis of DNAPL infiltration in a medium with a low permeability lens. Computational Geosciences, 1(2):191–214.

Glass, R.J., Parlange, J-Y, Steenhuis, T.S., 1989. Wetting front instability 1. Theoretical Discussion and dimensional analysis. Water Resources Research, 25(6):1187–1194.

Hofstee, C., Oostrom, M., Dane, J.H. and Walker, R.C., 1998. Infiltration and redistribution of perchloroethylene in partially saturated, stratified porous media. Journal of Contaminant Hydrology, 34:293–313.

Kessler, A. and Rubin, H., 1987. Relationships between water infiltration and oil spill migration in sandy soils. Journal of Hydrology, 91:187–204.

Kool, J.B, Parker, J.C. and van Genuchten, M.Th., 1985. Determining soil hydraulic properties from one-step outflow experiments by parameter estimation: I. Theory and numerical studies. Soil Science Society American Journal, 49:1348–1354.

Kueper, B.H., Abbott, W. and Farquhar, G., 1989. Experimental observations of multiphase flow in heterogeneous porous media. Journal of Contaminant Hydrology, 5:83–95.

Kueper, B.H. and Frind, E.O., 1991. Two-phase flow in heterogeneous porous media. 1. Model development. Water Resources Research, 27(6):1049–1057.

Lenhard, R.J., Oostrom, M. and White, M.D., 1995. Modeling fluid flow and transport in variably saturated porous media with the STOMP simulator. 2. Verification and validation exercises. Advances in Water Resources, 18(6):365–373.

Leverett, M.C., 1941. Capillary behavior in porous solids. Trans.Am.Inst.Min.Metall.Pet.Eng., 142:152–169.

Mualem, Y., 1976. A new model for predicting the hydraulic conductivity of unsaturated porous media. Water Resources Research, 12(3):513–522.

Parker, J.C., Lenhard, R.J. and Kuppusamy, T., 1987. A parametric model for constitutive properties governing multiphase flow in porous media. Water Resources Research, 23(4):618–624.

Schroth, M.H., Istok, J.D. and Selker, J.S., 1998. Three-phase immiscible fluid movement in the vicinity of textural interfaces. Journal of Contaminant Hydrology, 32:1–23.

Schwille, F., 1988. Dense chlorinated solvents in porous and fractured media model experiments. Lewis Publishers, Chelsea, MI.

Steele, D.D. and Nieber, J.L., 1994. Network modeling of diffusion coefficients for porous media: II. Simulations. Soil Science Society American Journal, 558:1337–1345.

van Dam, J.C., Stricker, J.N.M. and Droogers, P., 1994. Inverse method to determine soil hydraulic functions from multistep outflow experiments. Soil Science Society American Journal, 56:647–652.

van Geel P.J. and Sykes, J.F., 1994. Laboratory and model simulations of a LNAPL spill in a variably-saturated sand, 2. Comparison of laboratory and model results. Journal of Contaminant Hydrology, 17:27–53.

van Genuchten, M.Th., 1980. A closed-form equation for predicting the hydraulic conductivity of unsaturated soils. Soil Science Society American Journal, 44:892–898.

Walser, G.S., Illangasekare, T.H. and Corey, A.T., 1999. Retention of liquid contaminants in layered soils. Journal of Contaminant Hydrology 39:91–108.

White, M.D. and Oostrom, M., 1996. STOMP: Subsurface Transport Over Multiple Phases. Theory Guide. PNNL-11217. Pacific Northwest National Laboratory, Richland, WA.

Wipfler, E.L., van der Zee, S.E.A.T.M., 2001. A set of constitutive relationships accounting for residual NAPL in the unsaturated zone. Journal of Contaminant Hydrology, 50:53–77.

Weast,R.C.(Editor),1985. CRC Handbook of Chemistry and Physics. CRC Press, Boca Raton, FL.

Chapter 5

Three-phase flow analysis of DNAPL infiltration in horizontally layered porous media*

5.1 Introduction

Infiltration of Non-Aqueous Phase Liquid (NAPL) into the subsurface is a serious environmental problem. Although NAPLs may be considered immiscible with water, they usually have water solubilities which exceed water quality standards, and therefore may contribute to groundwater contamination. Several remediation techniques like removal by pumping have been developed to remove NAPL from the subsurface. The effectiveness of these techniques may be poor due to spatial variation of porous medium properties like intrinsic permeability (k) and porosity (ϕ). Understanding the mechanisms that control NAPL behavior in case of heterogeneous porous medium properties and the ability to predict the subsurface distribution of NAPL is important for the success of remediation efforts.

Capillary forces play an important role in NAPL flow in heterogeneous porous media. In a two-phase system, the capillary pressure, p_c, which is the pressure difference between the wetting and the non-wetting fluid, can be written as (Leverett, 1941):

$$p_c = \gamma_{nw}\sqrt{\frac{\phi}{k}}J(S) \tag{5.1}$$

where γ_{nw} denotes the interfacial tension between the wetting fluid and the non-wetting fluid. The Leverett J function $J(S)$ depends on the wetting fluid saturation S, but is independent of porous medium and fluid properties. Consequently, if the permeability or the porosity changes between two

105

layers in a porous medium, continuity of capillary pressure forces the fluid saturation to be discontinuous across the interface between these layers. In turn, this may lead to discontinuities in the relative permeability at the layer interface, as the latter is a function of the fluid saturation. According to Darcy's law

$$u_i = \frac{-kk_{ri}}{\mu_i}\nabla(p_i - \rho_i g z), \qquad (5.2)$$

the Darcy velocity u_i of a given phase i is proportional to the pressure gradient ∇p_i, according to the mobility $\frac{kk_{ri}}{\mu_i}$, which consists of the intrinsic permeability k, the relative permeability k_{ri} and the viscosity μ_i. In Eq.(5.2) ρ_i denotes density of phase i and g denotes the gravitational acceleration, which acts in the direction of the vertical coordinate z. A strong reduction across a (horizontal) interface of the relative permeability of a downward infiltrating fluid may reduce the mobility, which in turn may reduce the fluid velocity across the interface. This often leads to accumulation of the fluid above the interface, as demonstrated by several studies that are outlined below.

The precise effect of changes of porous medium properties at the interface between layers depends on the wetting order of the infiltrating fluid relative to that of the fluids that are present in the medium. When a non-wetting fluid infiltrates (drainage) into a high permeable layer that lies on top of a low permeable layer, fluid will accumulate above the interface between the two layers. Analyses of the effect of low permeable layers on the infiltration of non-wetting fluid have been provided by van Duijn et al. (1995), de Neef and Molenaar (1997) and van Dijke and van der Zee (1998). van Duijn et al. (1995) mathematically derived a pressure condition in case of discontinuity of permeability or porosity, which admits solutions of the corresponding phase saturations. de Neef and Molenaar (1997) studied 2-D infiltration of non-wetting Dense-NAPL into a water-saturated porous medium containing a single low permeable lens of finite dimensions with a high entry pressure. They derived an explicit criterion for Dense-NAPL infiltration into the lens. van Dijke and van der Zee (1998) derived expressions for steady state non-wetting air flow below and through a low-permeable horizontal layer in an initially water saturated porous medium (air sparging). They provided an estimate for the radius of influence of the injected air. With a few modifications, their analysis applies also to Dense-NAPL infiltration above a water saturated low permeable layer. A similar problem has been studied by Pritchard et al. (2001) for vertical equilibrium flow

over the interface between two layers in layered porous media. Contrary to de Neef and Molenaar (1997) and van Dijke and van der Zee (1998), Pritchard et al. (2001) did not account for capillary pressure.

On the other hand, when a wetting fluid infiltrates (imbibition) in a high permeable layer flow may be enhanced by the high intrinsic permeability, but the wetting fluid relative permeability in such a layer is often strongly reduced. Therefore, when a wetting fluid flows downwards from a low permeable layer into a high permeable layer, its mobility usually decreases. Consequently, the wetting fluid has the potential to accumulate above the high permeable layer. This is referred to as the capillary barrier effect. Capillary barriers have been studied extensively with respect to water infiltration into dry sand of which an overview has been provided by Schroth et al. (1998).

In this paper, we consider the effect of a horizontally layered porous medium on the flow of an intermediate wetting fluid in a three-fluid phase system. We consider a water-wet soil where both water, the wetting fluid, and air, the non-wetting fluid, are present, and DNAPL, the intermediate-wetting fluid, infiltrates. The DNAPL infiltrates from a point source into a horizontal low permeable layer, which is located on top of a high permeable layer. The porous medium is unsaturated with water and the water saturation is assumed to be small near the interface between the layers. Because of the low water saturation we expect that near the interface, DNAPL displays mainly wetting fluid behavior, i.e. in interaction with air. Hence, the interface between the layers acts as a capillary barrier for the infiltrating DNAPL (Walser et al., 1999; Wipfler et al., in press). Note that, if in the given layer configuration the water saturation increases, DNAPL flow through the interface may be enhanced, as DNAPL is non-wetting relative to water.

The objective of this paper is to analyze the DNAPL spreading above the interface using a three-phase flow simulator and by developing an analytical approximation that provides an estimate for DNAPL pressure, saturation and lateral spreading in the area just above the interface when DNAPL flow has reached a steady state. We verify the accuracy of the analytical approximation by numerical calculations. The present work extends the analytical model of van Dijke and van der Zee (1998) for a two-phase system (water and air), where the non-wetting fluid (air) spreads below a low permeable layer, to a three-phase system (water, DNAPL, air), where the intermediate-wetting fluid spreads above a high permeable layer. The

analytical approximation identifies the key parameters that define the re-distribution of an intermediate wetting fluid in case of horizontally layered porous media in a three-phase system. Furthermore, the analytical approximation can easily be used for parameter combinations where the numerical procedure becomes less stable or requires very long computation times. It may also be helpful to verify newly developed numerical codes.

The paper is organized as follows. In Section 5.2 we formulate the (transient) model equations and in Section 5.2.1 we discuss an example simulation to support the analysis of the infiltration problem at steady state. We reformulate the steady state problem in dimensionless form and identify the governing dimensionless numbers in Section 5.3.1. We additionally identify DNAPL flow regimes in Section 5.3.2, which lead to a number of assumptions that will be used in the analytical approximation described in Section 5.3.3. In Section 5.3.3 we derive an ordinary differential equation for the DNAPL pressures at the layer interface that governs the DNAPL flow at steady state, followed by a discussion in Section 5.3.4. In Section 5.4.1 we show the results of numerical calculations and verify the accuracy of the analytical model by the numerical results in Section 5.4.2. In addition, we analytically perform a sensitivity analysis of the effects of the dimensionless numbers on the lateral extension of DNAPL at the interface in Section 5.4.3.

5.2   Model equations

We consider the flow of DNAPL and water in a water-wet soil, where additionally air is present at constant pressure ($p_a = 0$). Assuming that both fluids are incompressible and immiscible, the governing equations for the flow of water (w) or DNAPL (o) are the mass balance equation

$$\phi \frac{\partial \overline{S}_i}{\partial t} + \nabla \cdot u_i = 0 \qquad i = w, o. \tag{5.3}$$

u_i denotes the 3-D Darcy velocity vector of phase i, given by Eq (5.2), where the vertical component z is directed downwards, representing the depth below the soil surface. ϕ denotes the effective porosity, $\overline{S}_i$ denote the effective saturation of phase i and t denotes time. We assume that the soil consists of two horizontal layers, which are isotropic, but which have different soil properties. The effective saturations are related through $\overline{S}_w + \overline{S}_o = \overline{S}_t$ and $\overline{S}_t + \overline{S}_a = 1$, where $\overline{S}_a$ and $\overline{S}_t$ are the effective air and

total liquid saturations. Effective saturations have been derived from the actual saturations through

$$\overline{S}_w = \frac{S_w - S_{wr}}{1 - S_{wr}}, \quad \overline{S}_o = \frac{S_o}{1 - S_{wr}}, \quad \overline{S}_t = \frac{S_t - S_{wr}}{1 - S_{wr}}, \quad (5.4)$$

where S_{wr} is the residual water saturation. In the following we will use the notation S_w, S_o and S_t to denote the effective saturations. We assume that water is the wetting phase, air is the non-wetting phase and DNAPL is the intermediate-wetting phase, i.e. DNAPL is wetting relative to air, but non-wetting relative to water.

The phase pressures p_i are linked through the capillary pressure p_c^{ij} as $p_c^{ij} = p_i - p_j$, $ij = aw, ao, ow$, which in turn are functions of the effective fluid saturations. For the latter, we use scaled variants of the empirical function of Brooks and Corey (1966), which account for a distinct entry pressure, p_e, of the non-wetting fluid. For the two-phase air-water system this functional relation takes the form

$$S_w = \left(\frac{p_e}{p_c^{aw}}\right)^\lambda, \quad \text{for} \quad p_c^{aw} > p_e, \quad (5.5)$$

while $S_w = 1$ if $p_c^{aw} \leq p_e$. For the three phase air-DNAPL-water system the relations are

$$S_w = \left(\frac{p_e}{\beta_{ow} p_c^{ow}}\right)^\lambda \quad \text{for} \quad \beta_{ow} p_c^{ow} > p_e, \quad (5.6)$$

while $S_w = 1$ if $\beta_{ow} p_c^{ow} \leq p_e$, and

$$S_t = \left(\frac{p_e}{\beta_{ao} p_c^{ao}}\right)^\lambda \quad \text{for} \quad \beta_{ao} p_c^{ao} > p_e, \quad (5.7)$$

while $S_t = 1$ if $\beta_{ao} p_c^{ao} \leq p_e$. λ and p_e are Brooks and Corey parameters that represent the structure of the porous medium. β_{ow} and β_{ao} are ratios of the involved interfacial tensions, whose values are related as $\frac{1}{\beta_{ow}} + \frac{1}{\beta_{ao}} = 1$, thus ensuring continuity of S_w between the two-phase and three-phase systems, i.e. when $S_o = 0$ (Parker and Lenhard, 1987). For the functional relation between relative permeability and saturation we use the relationships proposed by Mualem (1976),

$$k_{rw} = S_w^{5/2+2/\lambda} \quad (5.8)$$
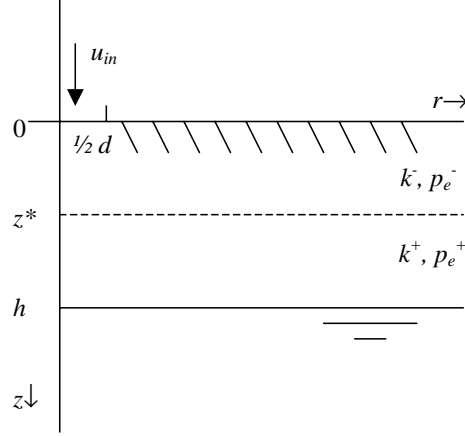
Figure 5.1: Schematic of the axially symmetric domain with two horizontal
layers, separated by the interface at $z = z^*$. DNAPL infiltrates at the soil level
$z = 0$ with an infiltration velocity, u_{in}, and the water table is located at $z = h$. The
layers have different soil properties, indicated by k^-, p_e^- and k^+, p_e^+, respectively.

and

$$k_{ro} = (S_t - S_w)^{1/2} \left(S_t^{1+1/\lambda} - S_w^{1+1/\lambda} \right)^2. \tag{5.9}$$

These relationships apply to the three-phase system as well as to the rel-
evant two-phase systems, in the sense that we use $S_t = 1$ in Eq.(5.9) for
the two-phase water-DNAPL system and that we only use Eq.(5.8) for the
two-phase air-water system. Hysteresis is not included in the analysis.

Eqs.(5.3) and (5.2) are solved in the axially symmetric domain shown
in Figure 5.1, where r is the radial coordinate. A low permeable horizontal
layer lies on top of a high permeable layer, separated by the level $z = z^*$.
The level $z = h$ corresponds to the position of the water table, which is
established by imposing a hydrostatic water pressure distribution at the
outside boundary, with $p_w = 0$ at $z = h$. DNAPL is introduced at $z = 0$
for $0 < r < \frac{1}{2}d$ with an infiltration rate of $u = u_{in}$, where d is the diameter
of the source area.

Denoting the intrinsic permeability in the high permeable layer as k^+
and in the low permeable layer as k^-, we introduce a contrast in soil prop-

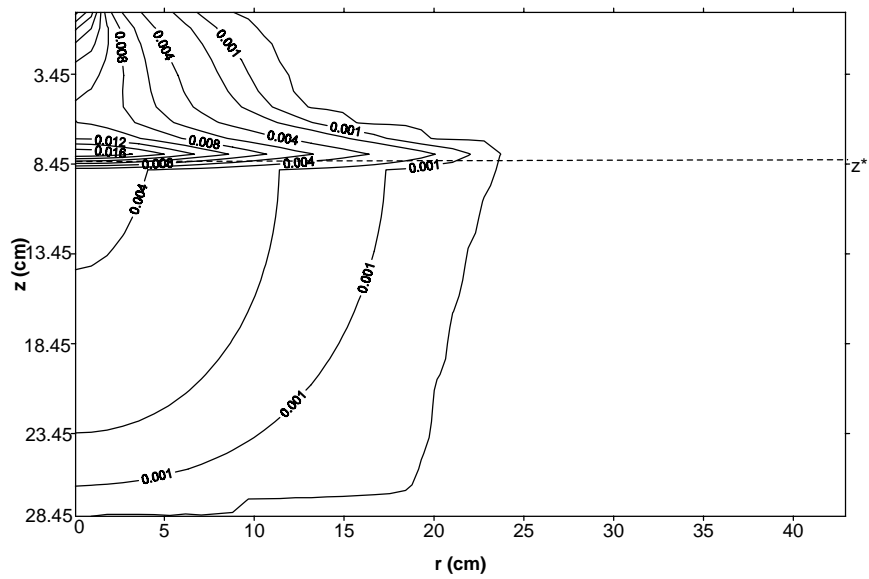**Figure 5.2:** Numerically obtained DNAPL saturation contours at steady state The horizontal dashed line indicates the interface between the two layers above which the infiltration DNAPL accumulates and spreads. Parameters values used in the calculation can be found in Tables 5.1 and 5.2.

erties by setting $k^+ = \gamma^2 k^-$, $\gamma > 1$. γ is the heterogeneity factor. Then, in agreement with the scaling theory of Leverett (1941), see Eq.(5.1), we additionally introduce contrasting entry pressures p_e^+ and p_e^- for the top and bottom layer respectively, with $p_e^+ = p_e^-/\gamma$. At the layer interface two conditions apply. Capillary pressure across the interface must be continuous and in addition, conservation of mass implies that the normal component of the flux across the interface must be continuous.

5.2.1   Example of a numerical solution

To get a qualitative picture of the behavior of infiltrating DNAPL in a layered soil, we have carried out an example simulation with parameter values presented in Tables 5.1 and 5.2. We will use the results of this calculation to support the subsequent analysis of the infiltration problem. Further details of the simulator and additional calculations are presented in Section 5.4. Obviously, the numerical calculation required a finite domain, of which the horizontal extension was taken so large that DNAPL did not reach the right-hand side boundary. At this right hand-side boundary for water the hydrostatic pressure distribution was imposed, such that the water saturation near the interface $z = z^*$ was small ($S_w = 0.016$ for this example calculation). For DNAPL a no flow condition was imposed at this boundary. At the left-hand side boundary no-flow conditions were imposed for both water and DNAPL. The bottom boundary was taken well below the level of the water table, where for water the consistent hydrostatic pressure was prescribed, while for DNAPL a pressure smaller than p_w was prescribed, such that DNAPL could move out of the domain through this boundary. The top boundary $z = 0$ was closed to both water and DNAPL, except for the area of the source, where the DNAPL flow rate was imposed as described above.

In Figure 5.2 we show the numerically obtained DNAPL saturation contours at steady state, i.e. when the amount of DNAPL flowing into and out of the domain are approximately equal and the saturation does not change anymore. The contours show that just above the interface the DNAPL has accumulated and spread out horizontally, indicating that for the present water distribution the high permeable layer indeed acts as a capillary barrier to the DNAPL infiltration. At steady state, water pressures were hydrostatically distributed anywhere in the domain, such that water did not flow anymore. In the entire domain DNAPL saturations were low, i.e. $S_o < 0.032$.

parameter	value
h [cm]	28.4
z^* [cm]	8.1
d [cm]	1.92
u_{in} [cms^{-1}]	1.667 10^{-8}
ϕ	0.4
k^- [cm^2]	6.3821 10^{-8}
p_e^- [Pa]	215
λ	2.3
γ	1.9
g [ms^{-2}]	9.793

Table 5.1: Geometry and porous medium properties used in the numerical simulations.

parameter	value
μ_w [Pa s]	1.0 10^{-3}
μ_o [Pa s]	2.0 10^{-3}
ρ_w [kgm^{-3}]	1000
ρ_o [kgm^{-3}]	1600
β_{ao}	1.8
β_{ow}	2.25
β_{aw}	1

Table 5.2: Fluid properties used in the numerical simulations.

5.3   Steady state flow analysis

5.3.1   Dimensionless formulation

We introduce the dimensionless variables:

$$T = \frac{tU_c}{\phi d}, \quad R = r/d, \quad Z = z/d, \quad U_o = u_o/U_c, \qquad (5.10)$$

where $U_c = \frac{k^- \rho_o g}{\mu_o}$ is the intrinsic DNAPL velocity of the low permeable layer. The source diameter, d, is chosen as the characteristic length. Hence, we define also the dimensionless distances $H = h/d$ and $Z^* = z^*/d$. Dimensionless pressures are defined as:

$$P_i = \frac{p_i}{p_e^-} \qquad i = w, o. \qquad (5.11)$$

Furthermore, we define the dimensionless constants:

$$N_g = \frac{k^- \rho_o g}{\mu_o u_{in}} \quad \text{and} \quad N_c = \frac{k^- p_e^-}{\mu_o u_{in} d}. \qquad (5.12)$$

N_g is the gravity number and N_c is the capillary number (both related to the low permeable layer). In agreement with the example calculation of Section 5.2.1, only DNAPL is assumed to flow at steady state, hence the water pressures are hydrostatically distributed according to

$$P_w(Z) = \frac{N_g}{N_c} \frac{\rho_w}{\rho_o} (Z - H). \qquad (5.13)$$

The governing steady state flow equations for DNAPL, following from Eqs.(5.2) and (5.3), are

$$\nabla \cdot U_o = 0 \qquad (5.14)$$

with

$$U_o = \begin{cases} k_{ro} \nabla \left(-\frac{N_c}{N_g} P_o + Z \right) & \text{for } Z < Z^* \\ \gamma^2 k_{ro} \nabla \left(-\frac{N_c}{N_g} P_o + Z \right) & \text{for } Z > Z^* \end{cases} \qquad (5.15)$$

for the low and the high permeable layers, respectively. Eqs.(5.14) and (5.15) must be solved for the only remaining unknown P_o, separately on the two sub-domains. The solutions are linked by the continuity conditions

at the interface for the DNAPL pressure and the vertical component of the DNAPL flux, U_Z, respectively, i.e.

$$\begin{aligned}
\lim_{Z \downarrow Z^*} P_o &= \lim_{Z \uparrow Z^*} P_o \\
\lim_{Z \downarrow Z^*} U_Z &= \lim_{Z \uparrow Z^*} U_Z.
\end{aligned} \tag{5.16}$$

To solve Eqs.(5.14) and (5.15), we only need a constitutive relation for the DNAPL relative permeability, k_{ro}. Using the definition for the capillary pressures and the assumption that $P_a = 0$, we rewrite relations (5.6) and (5.7) in dimensionless form as

$$S_w = \begin{cases} \hat{S}_w \left(P_o, P_w \right) & \text{for } Z > Z^* \\ \hat{S}_w \left(\gamma P_o, \gamma P_w \right) & \text{for } Z < Z^* \end{cases} \tag{5.17}$$

with $\hat{S}_w(P_o, P_w) = (\beta_{ow}(P_o - P_w))^{-\lambda}$ and

$$S_t = \begin{cases} \hat{S}_t \left(P_o \right) & \text{for } Z > Z^* \\ \hat{S}_t \left(\gamma P_o \right) & \text{for } Z < Z^* \end{cases} \tag{5.18}$$

with $\hat{S}_t(P_o) = (\beta_{ao}(-P_o))^{-\lambda}$. Then, the DNAPL relative permeability can be rewritten as

$$k_{ro} = \begin{cases} \hat{k}_{ro} \left(P_o, P_w \right) & \text{for } Z > Z^* \\ \hat{k}_{ro} \left(\gamma P_o, \gamma P_w \right) & \text{for } Z < Z^* \end{cases} \tag{5.19}$$

with $\hat{k}_{ro} \left(P_o, P_w \right) = k_{ro} \left(\hat{S}_w(P_o, P_w), \hat{S}_t(P_o) \right)$, while k_{ro} is defined by Eq.(5.9).

Notice that the definitions of Eqs.(5.17) to (5.19) are valid for $S_w < 1$ and $S_t < 1$, as we will only consider the fluid unsaturated part of the soil in the subsequent analysis. Consequently, we can also unambiguously define a critical DNAPL pressure P_o^c as a function of P_w, below which the DNAPL saturation is zero. Taking $S_o = S_t - S_w = 0$ in relations (5.17) and (5.18), this critical pressure is found as

$$P_o^c = \frac{\beta_{ow} P_w}{\beta_{ow} + \beta_{ao}}. \tag{5.20}$$

To facilitate the analysis, we have derived in Appendix A an approximate explicit relation between the reduced NAPL relative permeability $\hat{k}_{ro}$ and

P_o, P_w. As a result, the relative permeability given by Eq. (5.19) is approximated as

$$k_{ro} = \begin{cases} C_k(P_w) \left[P_o - P_o^c\right]^{\frac{5}{2}} & \text{for } Z > Z^* \\ C_k(\gamma P_w)(\gamma(P_o - P_o^c))^{\frac{5}{2}} = \\ \qquad \gamma^{-\frac{5}{2}\lambda - 2} C_k(P_w)(P_o - P_o^c)^{\frac{5}{2}} & \text{for } Z < Z^* \end{cases} \qquad (5.21)$$

which applies for small S_o, i.e. when P_o is close to P_o^c, with
$C_k(P_w) = \lambda^{5/2} \left(1 + \frac{1}{\lambda}\right)^2 (\beta_{ow} + \beta_{ao})^{5/2} (-P_w)^{-(5/2)\lambda - 9/2}$.

5.3.2   DNAPL flow regimes

To derive an analytical approximation for the lateral extension of the DNAPL at the interface between the high and the low permeable layers, we make a number of assumptions with respect to the regimes of DNAPL flow above and below the interface. The DNAPL relative permeability in the high permeable layer just below the interface is much smaller than in the low permeable layer, resulting in a smaller DNAPL mobility. Hence, we assume that below the interface the pressure gradient $\left(\frac{\partial P_o}{\partial Z}\right)$ is zero, the flow is only vertical and dominated by gravity. Then, we obtain from Eq.(5.15) that

$$U_Z \approx \gamma^2 k_{ro} \quad \text{for } Z < Z^*. \qquad (5.22)$$

As mentioned before, we may safely assume that the DNAPL saturation is small, hence we use the approximation (5.21) in the continuity condition (5.16) for U_Z to obtain

$$\lim_{Z \downarrow Z^*} \frac{\partial P_o}{\partial Z} \approx -\frac{N_g}{N_c}\left(\gamma^{-(5/2)\lambda} - 1\right) \qquad (5.23)$$

for the vertical pressure gradient just above the interface. Since we have $\lambda > 1$, this gradient is approximately equal to $\frac{N_g}{N_c}$ for sufficiently large values of the heterogeneity factor γ. If the gradient is exactly equal to $\frac{N_g}{N_c}$, DNAPL pressures just above the interface are at vertical equilibrium. Because of the relatively large absolute value of the power $(5/2)\lambda$, the contrast $\gamma > 1$ needs not be very large to yield a good approximation of the vertical equilibrium condition. Additionally, the pressure derivatives that we obtained from the example calculation of Section 5.2.1 confirm this conclusion. Consequently, we assume that in the region just above the

interface, where the DNAPL has spread out horizontally, DNAPL pressures are distributed hydrostatically, i.e.

$$P_o(R, Z) = P(R) - \frac{N_g}{N_c}(Z^* - Z).$$
(5.24)

where $P(R) = P_o(R, Z^*)$ is the DNAPL pressure at the interface.

Based on this assumption, we may explicitly define this vertical equilibrium flow region, which is shown in Figure 5.3. The region is bounded from above by the level $Z = Z_b(R)$, where the DNAPL saturation is equal to zero, i.e. $P_o(Z_b) = P_o^c$. This is a no-flow boundary for DNAPL. Using Eq.(5.24), Z_b is linked to P as

$$Z_b(R) = Z^* + \frac{N_c}{N_g}\left\{P_o^c - P(R)\right\}.$$
(5.25)

We define the maximum extension of the plume f, which occurs at the interface, i.e. $Z_b(f) = Z^*$. Instead of infiltration from the top, we assume that DNAPL is introduced via a tube with radius $1/2$, located at $R = 0$ such that the total dimensionless infiltration rate is equal to the original rate of $\pi/4N_g$. The tube has a height of $Z^* - Z_b(1/2)$. Along $Z = Z^*$ we impose a boundary condition for the vertical velocity component U_Z, which by flux continuity (Eq.(5.16)) follows from Eq.(5.22) as

$$U_Z(R, Z^*) = \gamma^2 \lim_{Z \uparrow Z^*} k_{ro}.$$
(5.26)

Obviously, at steady state the total flow rate through the interface equals

$$\int_{1/2}^{f} R U_Z(R, Z^*)dR = \pi/4N_g.$$
(5.27)

Finally, we assume that the height of the vertical equilibrium area is relatively small compared to the horizontal extension of the plume and that the water saturations are small in this region, as demonstrated in the numerical example of Section 5.2.1. Therefore, we may consider P_w and P_o^c, which according to Eq.(5.20) depends on the hydraulically distributed P_w, as constant throughout the region. For the water pressure we take the constant value, P_w^*, equal to that at the interface $Z = Z^*$, which follows from Eq. (5.13). Consequently, also the relative permeability defined by Eq(5.21) depends on P_o only, i.e. $k_{ro} = \hat{k}_{ro}(P_o, P_w^*)$ in the vertical equilibrium region.
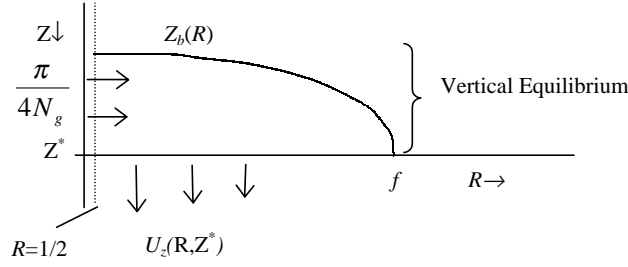
Figure 5.3: Schematic of the vertical equilibrium flow region, which is bounded by the interface at $Z = Z^*$ and by the free boundary at $Z = Z_b(R)$. At $R = 0$, between $Z = Z_b(1/2)$ and $Z = Z^*$ DNAPL is introduced via a tube with radius $\frac{1}{2}$, yielding a total infiltration rate of $\pi/4N_g$. At $Z = Z^*$ the vertical velocity component U_z is prescribed by continuity to the lower region. f denotes the maximum extension of the DNAPL plume at $Z = Z^*$.

5.3.3   Analytical flow model

Similar to the analysis of van Dijke and van der Zee (1998), we solve Eq.(5.14) combined with the first expression of Eq.(5.15) in the vertical equilibrium region presented in Figure 5.3, subject to the above described boundary conditions, to obtain the DNAPL pressure at the interface, $P(R) = P_o(R, Z^*)$. Notice that also the free boundary $Z_b(R)$, hence the maximum extension f, is unknown and will be part of the solution. First, we integrate the mass balance equation (5.14) in radial co-ordinates over the height of the region, yielding

$$\int_{Z_b}^{Z^*} \left(\frac{\partial RU_R}{\partial R} + R\frac{\partial U_Z}{\partial Z} \right) = 0. \tag{5.28}$$

Using $U_R(R, Z_b) = U_Z(R, Z_b) = 0$, where U_R and U_Z are the horizontal and vertical components of the DNAPL velocity, respectively, Eq.(5.28) becomes

$$\frac{\partial}{\partial R} \left(R \int_{Z_b}^{Z^*} U_R(R, Z)dZ \right) + RU_Z(R, Z^*) = 0. \tag{5.29}$$

To evaluate the first term of Eq.(5.29), we derive from Eq.(5.24):

$$\frac{\partial P_o(R,Z)}{\partial R} = \frac{dP(R)}{dR} \quad \text{and } dZ = \frac{N_c}{N_g} dP(R). \tag{5.30}$$

Using Eq.(5.15) and the definition of the reduced relative permeability (5.21) we find

$$\int_{Z_b}^{Z^*} U_R(R,Z) dZ = -\frac{N_c}{N_g} \int_{Z_b}^{Z^*} \hat{k}_{ro}(P_o(R,Z), P_w^*) \frac{\partial P_o(R,Z)}{\partial R} dZ =$$
$$-\frac{N_c^2}{N_g^2} D(P(R)) \frac{dP(R)}{dR} \tag{5.31}$$

where D is defined as $D(P) = \int_{P_o^c}^{P} \hat{k}_{ro}(\xi, P_w^*) d\xi$.

At the boundary $Z = Z^*$ condition (5.26) applies, where we use definition (5.21) to write $\lim_{Z \uparrow Z^*} k_{ro} = \lim_{Z \uparrow Z^*} \hat{k}_{ro}(\gamma P_o, \gamma P_w) = \hat{k}_{ro}(\gamma P, \gamma P_w^*)$. Hence, Eq.(5.29) is written as

$$\frac{-N_c^2}{N_g^2} \frac{d}{dR} \left\{ RD(P) \frac{dP}{dR} \right\} + R\gamma^2 \hat{k}_{ro}(\gamma P, \gamma P_w^*) = 0. \tag{5.32}$$

Integration of the mass balance Eq. (5.29) over R from $R = 1/2$ to $R = f$, to which we apply condition (5.27), gives the flux boundary condition at $R = 1/2$

$$-2\pi \frac{N_c^2}{N_g^2} RD(P) \frac{dP}{dR} \bigg|_{R=1/2} = \frac{\pi}{4N_g}. \tag{5.33}$$

Hence we solve the boundary value problem for P

$$\begin{cases} \frac{-N_c^2}{N_g^2} \frac{d}{dR} \left\{ RD(P) \frac{dP}{dR} \right\} + R\gamma^2 \hat{k}_{ro}(\gamma P, \gamma P_w^*) = 0 \ \text{ for } \frac{1}{2} < R < f \\ -2\pi \frac{N_c^2}{N_g^2} RD(P) \frac{dP}{dR} \big|_{R=1/2} = \frac{\pi}{4N_g}, \qquad P(f) = P_o^c. \end{cases} \tag{5.34}$$

Because the maximum horizontal extension, f, of the DNAPL is unknown, an additional boundary condition is required to solve problem (5.34). van Dijke and van der Zee (1998) have shown that this condition can be derived considering that at steady state the free boundary $Z_b(R)$ is tangential to the DNAPL flow direction at $R = f$. This leads to the condition for the gradient of P at f

$$\lim_{R \to f} \left(\frac{dP}{dR}(R) \right)^2 = \lim_{R \to f} -\gamma^2 \frac{N_g^2}{N_c^2} \frac{\hat{k}_{ro}(P, P_w^*)}{\hat{k}_{ro}(\gamma P, \gamma P_w^*)}. \tag{5.35}$$

Since for $R \to f$ P approaches P_o^c, we apply the approximations Eq.(5.21) to obtain the boundary condition

$$\frac{dP}{dR}(f) = -\gamma^{-\frac{5}{4}\lambda} \frac{N_g}{N_c}. \tag{5.36}$$

We iteratively solve the differential equation of problem (5.34) as an initial value problem starting at $R = f$, while varying the values of f, until the condition at $R = 1/2$ is matched. Further detail of the numerical solution of problem (5.34) can be found in van Dijke and van der Zee (1998). After the solution for P and f is obtained, the full solution for the DNAPL pressure P_o in the vertical equilibrium region can immediately be derived from Eq.(5.24).

5.3.4   Discussion

Mathematically, problem (5.34) is the same as the flow problem studied by van Dijke and van der Zee (1998). However, as mentioned in the introduction, the underlying physical problem exhibits two important differences. On the one hand, we consider a three-phase system instead of a two-phase system, in which P_o^c reflects the effect of the presence of the (wetting) water phase on the flow of the (intermediate-wetting) DNAPL phase. In the limiting case, water is entirely absent, i.e. when $P_w \to -\infty$ and, according to Eq.(5.20), $P_o^c \to -\infty$, DNAPL will spread infinitely at the interface. Hence, we may expect the DNAPL spreading to grow with decreasing P_o^c.

On the other hand, whereas in the model of van Dijke and van der Zee (1998) the heterogeneity reduces both the intrinsic permeability and the relative permeability to cause the infiltrating fluid to spread near the interface between the layers, the heterogeneity has opposite effects on these parameters in the present problem. Going from the low to the high permeable layer, the effect of the heterogeneity can easily be illustrated by considering the approximation for the DNAPL relative permeability, Eq.(5.21). Between the low permeable layer and the high permeable layer the intrinsic permeability increases with a factor γ^2 whereas the relative permeability reduces, according to the approximation, with a factor $\gamma^{-(5/2)\lambda-2}$. Considering the approximate vertical flux through the interface given by Eq.(5.26), we still find an overall reduction of the mobility of $\gamma^{-(5/2)\lambda}$. This mobility reduction illustrates that increasing either γ or λ, both of which are always larger than 1, enhances the spreading of the DNAPL.

Additional to the discussed dimensionless numbers P_o^c, γ and λ, problem (5.34) also contains the dimensionless numbers N_g and N_c representing the ratio between gravity, viscous forces and capillary forces, although these numbers appear in the combinations N_c/N_g and $1/N_g$. Using the analytical approximation, we will show the effect of each of these numbers on the DNAPL spreading in the next section.

5.4   Results and discussion

5.4.1   Numerical computations

We have carried out a number of flow calculations for the full problem of DNAPL infiltration described in Section 5.2 and compare the resulting steady state DNAPL distributions with those computed from the analytical approximation of Section 5.3. The simulations have been carried out using a fully implicit, 2-D axially symmetric, integrated finite difference multiphase flow code called STOMP with fully implicit time differencing (White and Oostrom, 1996). In this code, the set of equations (5.3) and (5.2) are solved with a multivariable, residual based Newton-Raphson iteration technique. Upwind interfacial averaging is used to approximate the relative permeabilities. Further details of the simulator can be found in White and Oostrom (1996).

The boundary conditions for the simulations have been imposed as described in Section 5.2. The 2-D computational domain consisted of 6210 cells. The grid was refined near the source and the layer interface, with the horizontal and vertical grid spacing varying from $\Delta r = 0.12$ cm to $\Delta r = 0.6$ cm and from $\Delta z = 0.04$ cm to $\Delta z = 0.8$ cm, respectively. The values of the non-transformed physical soil and fluid parameters, which were used in the simulator, are presented in Tables 5.1 and 5.2. These have been taken for the base case (Case 1), of which preliminary results have been presented in Section 5.2.

Compared to this base case, the dimensionless numbers defined in Section 5.3, have been varied as indicated in Table 5.3. In Cases 2 and 3 P_o^c has been varied by adjusting the hydrostatic water pressure, i.e. by varying h. In Cases 4 and 5 the ratio N_c/N_g has been varied by varying the source diameter d, in Cases 6 and 7 the capillary contrast γ has been varied, in Cases 8 and 9 the porous medium property λ has been varied and in Cases 10 and 11 N_g has been varied by varying the infiltration velocity u_{in}. In Case 12 the DNAPL has been replaced by an LNAPL. For this case the

Case	γ	λ	P_o^c	N_c/N_g	$1/N_g$ (10^{-6})
1	1.9	2.3	-5.126	0.716	3.334
2	1.9	2.3	-3.611	0.716	3.334
3	1.9	2.3	-5.265	0.716	3.334
4	1.9	2.3	-5.126	0.573	3.334
5	1.9	2.3	-5.126	0.955	3.334
6	1.7	2.3	-5.126	0.716	3.334
7	2.05	2.3	-5.126	0.716	3.334
8	1.9	2.0	-5.126	0.716	3.334
9	1.9	2.5	-5.126	0.716	3.334
10	1.9	2.3	-5.126	0.716	2.500
11	1.9	2.3	-5.126	0.716	4.168
12	1.9	2.3	-5.126	0.716	3.334

Table 5.3: Dimensionless parameters and numbers used in the computations

NAPL density has been given the value $\rho_o = 800$ kg m^{-3}. By simultaneously increasing the values of k^- to 1.2764 10^{-7} cm^2 and of d to 3.84 cm, the dimensionless numbers have been kept the same as for Case 1.

For the base case, we found that the spreading of the plume above the interface is sensitive to the vertical discretization. For example, decreasing the Δz from the cells around the interface from 0.08 cm to 0.04 cm increased the spreading of the plume by up to 2.5%. Due to computational restrictions we have not decreased the gridsize any further. This may imply that the simulator slightly under-predicts the spreading of the plume. In every case the flow became stationary. We defined the steady state time as the time beyond which the flux across the interface is more than 99.4 % of the infiltrating flux. The steady state time for the cases 1 to 12 varied between 28.4 yr. (case 8) and 80 yr. (case 9). The computation time was approximately 4 hrs.

Note that the scale of the simulated flow problems is smaller than for most realistic problems, because of restrictions concerning convergence, grid size and computation time. However, the dimensionless analysis shows how the simulations can be scaled up without changing the results. E.g. multiplication of the extension of the domain, the diameter of the source, d, the intrinsic permeability of the low permeable layer, k^-, and the entry pressure, p_e^-, by the same factor, keeps the dimensionless numbers the same as in the presented calculations. Furthermore, a larger and probably more

realistic extension of the plume above the layer interface can be obtained by increasing γ or λ, as discussed in Section 5.3.4. However, increasing these factors leads to numerical convergence problems and it requires a much finer grid and significantly larger computation times. Fortunately, the analytical approximation still provides a good estimate of the plume extension at steady state as we will show in the next subsection.

5.4.2 Comparison of analytical and numerical results

In Figure 5.4 both the analytical and the numerical solutions for the DNAPL pressure $P_o - P_o^c$ at the interface level $Z = Z^*$ are presented as a function of the radial co-ordinate R for the parameters of Case 1. The maximum horizontal extension of the plume f is attained where $P_o - P_o^c = 0$. The profiles show good agreement, although near $R = 1/2$ the two solutions deviate slightly, which is probably caused by the different DNAPL inflow conditions. Furthermore, the analytical solution underestimates the extension of the plume by about 15 %. The assumptions in the analytical approximation of strictly gravity-driven flow below the layer interface and of complete vertical pressure equilibrium just above the interface contribute both to this underestimation. In addition, in the analytical approximation P_o^c has been assumed constant, equal to the value at $Z = Z^*$, throughout the vertical equilibrium region, which is a slight overestimation of the numerically obtained values.

For comparison, we present in Figure 5.5 the analytically and numerically calculated DNAPL saturation profiles at the interface for the parameters of Case 1. For the analytical approximation, this profile has been calculated from the $P_o - P_o^c$ values presented in Figure 5.4, using Eqs.(5.17) and (5.18), where for the water pressure the value $P_w(Z^*)$ has been taken from the hydrostatic distribution (5.13). The agreement between the two solutions is similar to that for the pressure profiles of Figure 5.4, although the agreement is worse near $R = 1/2$ as a result of the non-linear relation between saturation and pressure.

To quantify the agreement between the analytically and numerically obtained solutions, we have compared the maximum extensions of the plume at $Z = Z^*$, which we refer to as f_a and f_n, respectively, through the relative error $(f_n - f_a)/f_n$. In Figure 5.6 the relative error is presented as a function of the normalized dimensionless parameters. As shown in Figures 5.4 and 5.5, for Case 1 $f_a = 10.8$ and $f_n = 12.7$, such that the relative error of the reference case was 14.9%. According to Figure 5.6 increasing either
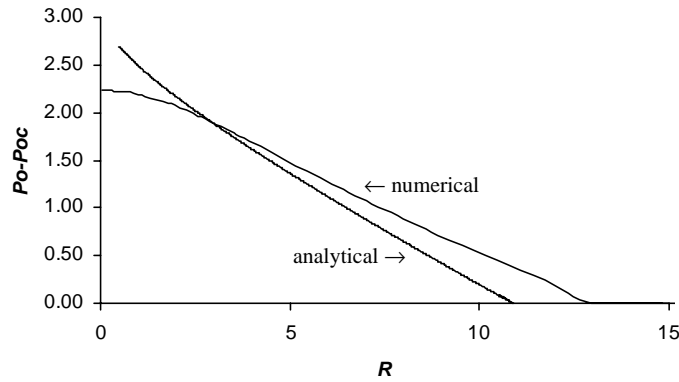
Figure 5.4: Dimensionless numerically and analytically calculated DNAPL pressure profiles at the interface between the low and the high permeable layers for the parameters of Case 1. When $P_o - P_o^c = 0$ the maximum extension of the plume is reached.

λ or γ results in a better agreement of the analytical approximation with the numerical calculation, whereas $1/N_g$ and N_g/N_c hardly affect the accuracy of the analytical solution. As discussed in Section 5.3.4 both γ and λ lead to an increase of the mobility difference across the interface which increases the agreement with the assumptions underlying the analytical approximation. Furthermore, if the critical DNAPL pressure P_o^c decreases, the relative error decreases. Notice that a decrease of P_o^c corresponds to an increase of the the normalized value, as P_o^c is negative valued. Finally, the analytical approximation for the LNAPL simulation is equally accurate as for DNAPL. For this case the numerically obtained extension $f_n = 12.9$, with a relative error of 16.3 %.

5.4.3   Sensitivity analysis

To quantify the effect of the dimensionless parameters on the spreading of the plume above the interface, we have performed a sensitivity analysis for the horizontal extension f of the plume using the analytical approximation. The analytically calculated extensions f_a of the plume are shown in Figure
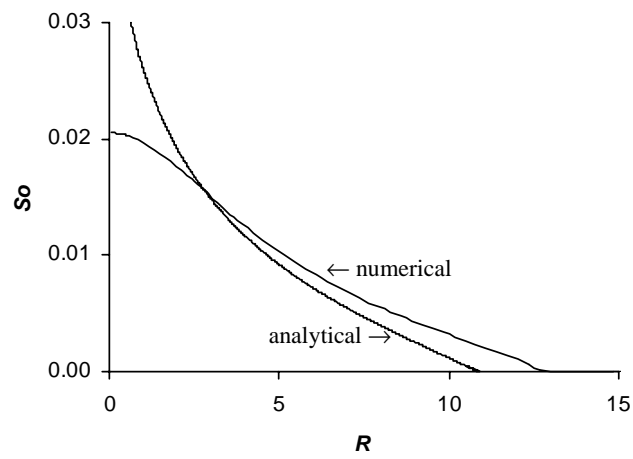
Figure 5.5: Numerically and analytically calculated DNAPL saturations the interface between the low and the high permeable layers for the parameters of Case 1.
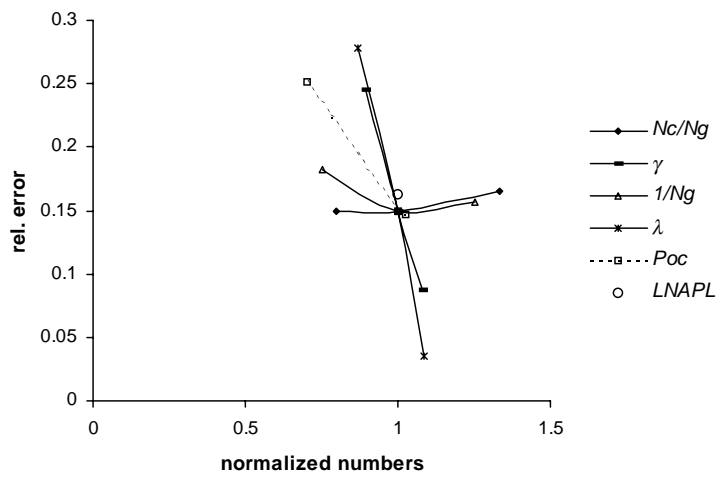
Figure 5.6: Relative error of the numerically and analytically obtained plume extension as a function of the dimensionless parameters. The dimensionless parameters are normalized by those of Case 1. The LNAPL simulation has been carried out for the parameters of Case 1 but with a different NAPL density.

Figure 5.7: Sensitivity of the extension of the plume at the interface, f, to dimensionless parameters, relative to the extension for Case 1. Also the dimensionless numbers are normalized by those of Case 1.

5.7, normalized by the value $f_{a1} = 12.7$ for Case 1, as $\frac{f_a - f_{a1}}{f_{a1}}$. Notice that we have considered extensions for a fairly wide range of the parameters, which we would not have been able to obtain numerically because of the co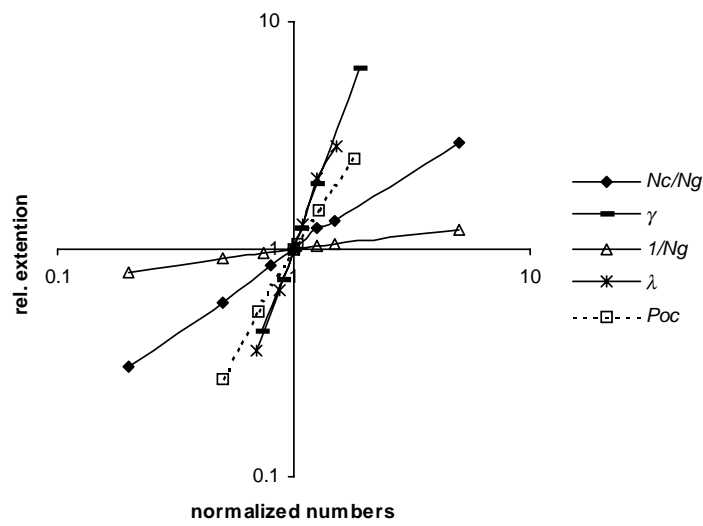mputational problems discussed above, although convergence restrictions of the analytical approximation still require a limited increase of the normalized P_o^c and λ. The extension of the plume appears to be particularly sensitive to λ and γ, because these parameters strongly affect the mobility differences across the interface. The cases with larger λ and γ values are more interesting than those with smaller values, as the former give very accurate approximations of the plume extension, according to Figure 5.7, and are difficult to obtain numerically. In agreement with the discussion of Section 5.3.4 also the value of P_o^c has a considerable effect on the plume extension. When P_o^c decreases (i.e. when the normalized P_o^c increases) less water is present and the NAPL can spread out further. Similarly, increasing the value of $\frac{N_c}{N_g}$, which represents the absolute value of the entry pressures, as $\frac{N_c}{N_g} = \frac{p_e^-}{\rho_o g}$, leads to a larger extension. However, from Figure 5.7 we conclude that the corresponding analytical approximations are not increasingly more accurate. Finally, $\frac{1}{N_g}$, which represents the effect of the infiltration rate, has only a small effect on the spreading of the plume.

5.5   Conclusions

We have considered DNAPL infiltration into a water unsaturated porous medium that consists of two horizontal layers, of which the top layer has a lower intrinsic permeability than the bottom layer. DNAPL is intermediate-wetting relative to the wetting water and the non-wetting air. We have demonstrated that the layer interface forms a barrier to DNAPL flow due to the fact that the DNAPL mobility is lower in the high permeable layer, which causes the DNAPL to spread out horizontally just above the interface. As a result, the DNAPL pressure distribution just above the layer interface is close to vertical equilibrium, while below the interface DNAPL flow is approximately gravity-driven. Based on these observations, we have developed an analytical approximation to estimate the DNAPL pressure and saturation and the horizontal extension of the DNAPL plume just above the layer interface at steady state for low water saturations.

The analytical approximation shows that the steady state DNAPL infiltration is determined by 5 dimensionless numbers: the heterogeneity factor γ, the Brooks and Corey capillary pressure parameter λ, the gravity number

N_g, the ratio of the capillary and gravity numbers N_c/N_g, and the critical DNAPL pressure P_o^c, which indicates the effect of the water saturation on the flow of DNAPL.

To test the validity of the analytical approximation, we have compared its predictions with the results of a three-phase flow simulator for a number of parameter combinations. For most of these combinations the analytical approximation predicts the DNAPL pressure and saturation profiles at the interface adequately, although it slightly underestimates the horizontal spreading of the plume at the interface. We have shown that for increasing γ and λ, which lead to larger mobility differences across the layer interface, the accuracy of the approximation improves. The approximation improves also for decreasing P_o^c, indicating lower water saturations. The analytical model provides also an accurate prediction for the horizontal spreading when the DNAPL is replaced by an LNAPL under otherwise similar conditions.

Using the analytical approximation, we have carried out a sensitivity study with respect to the maximum horizontal extension of the plume. It turns out that the extension of the plumes appears to be highly sensitive to variation of the dimensionless numbers P_o^c, λ and γ. The extension increases for increasing values of λ and γ and for decreasing values of P_o^c, which underlines that in general the analytical approximation improves when the horizontal spreading is larger.

Appendix A Relative permeability approximation

For P_o close to the critical NAPL pressure, P_o^c, the reduced NAPL relative permeability $\hat{k}_{ro}$ can be approximated by an expansion in terms of $P_o - P_o^c$. From Eq. (5.18) follows that

$$\hat{S}_t(P_o) = \left(\frac{-1}{\beta_{ao}P_o}\right)^\lambda = \left(\frac{\frac{-1}{\beta_{ao}P_o^c}}{\frac{P_o-P_o^c}{P_o^c}+1}\right)^\lambda = (-P_w)^{-\lambda}\left(1 - \beta_{ao}\frac{P_o - P_o^c}{-P_w}\right)^{-\lambda},$$
$$(5.37)$$

where we have used definition (5.20) for P_o^c and the constraint $\frac{1}{\beta_{ao}} + \frac{1}{\beta_{ow}} = 1$ to find $P_o^c = \frac{P_w}{\beta_{ao}}$. Using the binomial expansion $(1+x)^\alpha = 1 + \alpha x + O(x^2)$ for small x, we obtain for $\hat{S}_t$ the first order approximation

$$\hat{S}_t(P_o) \approx (-P_w)^{-\lambda}\left(1 + \lambda\beta_{ao}\frac{P_o - P_o^c}{-P_w}\right). \qquad (5.38)$$

Similarly, we approximate $\hat{S}_w$, defined in Eq. (5.17), by

$$
\begin{aligned}
\hat{S}_w(P_o, P_w) &= (-P_w)^\lambda \left(1 - \beta_{ow} \frac{P_o - P_o^c}{-P_w} \right)^{-\lambda} \\
&\approx (-P_w)^{-\lambda} \left(1 + \lambda \beta_{ow} \frac{P_o - P_o^c}{-P_w} \right)
\end{aligned} \tag{5.39}
$$

where we have again used definition (5.20) for P_o^c to find $P_o^c - P_w = \frac{-P_w}{\beta_{ow}}$. Note that by introducing P_o^c into Eq.(5.37) we have obtained an artificial dependence of S_t on P_w. We did this to obtain a similar form of the equation as Eq.(5.39).

To approximate the NAPL relative permeability, we substitute expressions (5.37) and (5.39) in Eq. (5.9) to find

$$
\begin{aligned}
&\hat{k}_{ro}(P_o, P_w) \approx \lambda^{1/2} \left(\beta_{ao} + \beta_{ow} \right)^{1/2} (P_w)^{-(5/2)\lambda - 5/2} (P_o - P_o^c)^{1/2} \\
&\left(\left(1 + \lambda \beta_{ao} \frac{P_o - P_o^c}{-P_w} \right)^{1+1/\lambda} - \left(1 + \lambda \beta_{ow} \frac{P_o - P_o^c}{-P_w} \right)^{1+1/\lambda} \right)^2
\end{aligned} \tag{5.40}
$$

Using again the binomial expansion, we obtain the final approximation

$$
\hat{k}_{ro}(P_o, P_w) \approx C_k(P_w) (P_o - P_o^c)^{5/2} \tag{5.41}
$$

where $C_k(P_w) = \lambda^{5/2} \left(1 + \frac{1}{\lambda} \right)^2 (\beta_{ow} + \beta_{ao})^{5/2} (-P_w)^{-(5/2)\lambda - 9/2}$.

Notation

C_k	DNAPL relative permeability coefficient
d	diameter of DNAPL source [m]
D	dimensionless relative permeability integral
f	dimensionless radial position of the free boundary, Z_b of the DNAPL plume at $Z = Z^*$
g	gravity [m s^{-2}]
$h(H)$	(dimensionless) distance from the soil surface to the watertable [m]
k	intrinsic permeability [m^2]
k_{ri}	relative permeability of phase i
$\hat{k}_{ri}$	reduced relative permeability of phase i
N_c	capillary number
N_g	gravity number
P	dimensionless DNAPL pressure at $Z = Z^*$
$p_i(P_i)$	(dimensionless) pressure phase i

$p_c^{ij}(P_c^{ij})$ (dimensionless) capillary pressure fluid i and j [Pa]

p_e entry pressure [Pa]

P_o^c dimensionless critical NAPL pressure [Pa]

$r(R)$ (dimensionless) radial coordinate [m]

$S_i(\overline{S}_i)$ (effective) saturation phase i

$t(T)$ (dimensionless) time [s]

$u_i(U_i)$ (dimensionless) velocity of fluid phase i [ms^{-1}]

u_{in} infiltration velocity [ms^{-1}]

U_c characterisic velocity [ms^{-1}]

$z(Z)$ (dimensionless) vertical coordinate [m]

β_{ij} scaling coeficients for fluid phase i and j

γ heterogeneity factor

γ_{nw} interfacial tension between the wetting
and the non-wetting fluid [Nm^{-1}]

λ Brooks and Corey porous medium parameter

μ_i viscosity phase i [Pa s]

ρ_i density phase i [kg m^{-3}]

ϕ effective porosity

Subscripts

a air

b boundary

o DNAPL

r residual

R radial direction

t total

w water

Z vertical direction

Superscripts

c critical

$+$ high permeable porous medium

$-$ low permeable porous medium

$*$ layer interface

References

Brooks, R.H. and Corey, A.T.,1966. Properties of porous media affecting fluid flow. Journal of Irrigation and Drainage Division, 92:61–88.

de Neef, M.J. and Molenaar, J., 1997. Analysis of DNAPL infiltration in a medium with a low permeability lens. Computational Geosciences, 1(2):191–214.

Leverett, M.C., 1941. Capillary behavior in porous solids. Trans.Am.Inst.Min.Metall.Pet.Eng., 142:152–169.

Mualem, Y., 1976. A new model for predicting the hydraulic conductivity of unsaturated porous media. Water Resources Research, 12(3):513–522.

Parker, J.C. and Lenhard, R.J., 1987. A model for hysteretic constitutive relations governing multiphase flow: 1. Saturation-Pressure relations. Water Resources Research, 23 (12), 2187–2196.

Pritchard, D., Woods, A.W. and Hogg, A.J., 2001. On the slow draining of a gravity current moving through a layered permeable medium. J. Fluid Mech. 444, 23-47.

Schroth, M.H., Istok, J.D. and Selker, J.S., 1998. Three-phase immiscible fluid movement in the vicinity of textural interfaces. Journal of Contaminant Hydrology, 32:1–23.

van Dijke, M.I.J. and van der Zee, S.E.A.T.M., 1997. A similarity solution for oil lens redistribution including capillary forces and oil entrapment. Transport in Porous Media, 29:99-125.

van Dijke, M.I.J. and van der Zee, S.E.A.T.M., 1998. Modeling of air sparging in a layered soil: Numerical and analytical approximations. Water Resources Research, 34(3):341–353.

van Duijn, C.J., Molenaar, J. and de Neef, M.J., 1995. Effects of capillary forces on immiscible two-phase flow in heterogeneous porous media. Transport in Porous Media, 21:71–93.

Walser, G.S., Illangasekare, T.H. and Corey, A.T., 1999. Retention of liquid contaminants in layered soils. Journal of Contaminant Hydrology 39:91–108.

White, M.D. and Oostrom, M., 1996. STOMP: Subsurface Transport Over Multiple Phases. Theory Guide. PNNL-11217. Pacific Northwest National Laboratory, Richland, WA.

Wipfler, E.L. Ness, M., Breedveld, G.D. Marsman, A. and van der Zee, S.E.A.T.M. Infiltration and redistribution of LNAPL in unsaturated layered porous media. Journal of Contaminant Hydrology, in press.

Summary

Contamination of groundwater by organic liquids, such as gasoline, fuel oils and chlorinated hydrocarbons, forms a serious treat to subsurface water resources. These liquids have a low miscibility with water and move as a discrete liquid phase. A small part of the liquid may dissolve in water and small concentrations can be hazardous for humans. These organic liquids that are also referred to as Non-Aqueous Phase Liquids (NAPLs), may enter the subsurface from a surface spill or a leaking underground pipe or tank. Following a release of sufficient NAPL into the subsurface, NAPL moves through the pores of the soil due to gravitational and capillary forces.

An enhanced understanding of NAPL flow in the subsurface is needed to identify the critical processes and to determine key parameters in the context of remediation strategies at the field scale. In this thesis we study the behavior of NAPL in soil experimentally and numerically. we focus on the physical aspects of this behavior in the unsaturated part of the soil. This implies that we study the movement, interaction and (re-)distribution in a porous medium (soil) of three fluid phases: water, NAPL and air. The porous medium is water-wet, i.e. water is the wetting fluid, NAPL is the intermediate wetting fluid and air is the non-wetting fluid. This leads to typical three-phase flow behavior. We focus on two problems that are both related to NAPL redistribution into unsaturated soil after a spill: (1) non-drainable residual NAPL and (2) the effect of soil layers on the redistribution of NAPL after a spill. In addition to the introduction, the thesis contains 4 chapters which can be read as self-contained papers.

Non-drainable residual NAPL is considered to be the NAPL that remains in the capillaries of a porous medium after (gravity) drainage and displacement by air in the presence of residual water in a water-wet soil. Although for remediation strategies it is important to consider this residual NAPL, until now it has not been incorporated into multi phase flow models.

In Chapter 2 we develop a constitutive set of saturation-capillary pressure ($P_c - S$) relationships that accounts for non-drainable residual NAPL and that can be used by multi-phase flow models. These relationships are derived from a conceptual pore scale model of which the soil is represented by packed spheres. According to the model, NAPL becomes immobilized (residual) below a certain critical total liquid saturation, S_t^c. This critical total liquid saturation is porous medium and fluid dependent. Next, the non-drainable residual NAPL saturation increases, when the spreading coefficient of a NAPL decreases. Furthermore, a higher water saturation results in a lower non-drainable residual saturation. Although the model adequately simulated one individual experimental non-drainable residual NAPL data set, this agreement is a shallow basis for assessing whether the model assumptions are valid.

For this purpose we developed an experiment especially designed to measure three-phase $P_c - S$ relationships and non-drainable residual saturation including independent measurement of the water saturation and pressure. We performed four experiments. We used the fluids water, non-spreading dodecane and air, and sand as the porous medium. The measured non-drainable residual saturation was at most 0.081. From the experimental results no correlation could be observed between the water saturation and the residual NAPL saturation. This might indicate that other mechanisms are involved that are not captured by the constitutive model. In advance of the development of the experimental set up, we searched in the literature for available macroscale experimental data that could provide us with non-drainable residual saturation data that are related to porous medium properties, fluid properties and fluid saturations. After a careful selection we obtained 26 non-drainable residual NAPL data from 9 references. Measured values of non-drainable residual saturation varied between 0.001 and 023. From these data only a relationship between the spreading coefficient C_s, and the residual saturation S_{or}, could be assessed. The value of S_{or} decreases as C_s becomes less negative. It would require a much more comparable description of the different porous media, and a systematic data acquisition for S_{or} as a function of macroscale properties to assess which other factor than the spreading coefficient might be hidden in the data.

Changes of porous medium properties such as permeability and porosity across an interface between two soil layers might change the redistribution of NAPL. The mobility may decrease or increase across the interface, which is dependent on the permeability of the layers, the capillarity of the layers

and the wetting role that is played by the NAPL with respect to water and air. The effect of these changes have been studied in Chapter 4 and 5.

In Chapter 4 we focussed on the effect of an inclined soil layer with respect to the watertable. Two experiments were performed using a sand filled transparent chamber. The first experiment consisted of Light-NAPL infiltration into a fine sand matrix containing a coarse sand layer and the second experiment consisted of LNAPL infiltration into a coarse sand matrix containing a fine sand layer. The sand was partially saturated with water. We modeled the experiments numerically. The observed LNAPL behavior can be understood by considering that LNAPL might encounter two types of barriers. On the one hand, it may accumulate and spread above a coarse sand layer, that has a low water saturation and, that acts as a capillary barrier for the LNAPL before it may infiltrate into the layer. An on the other hand, it may accumulate and spread above a water saturated fine sand layer that has a high entry pressure for the infiltrating LNAPL. Sensitivity analysis performed with the numerical model shows that the qualitative LNAPL redistribution, in case of inclined layers, is mainly subject to the capillarity contrast between sands.

In Chapter 5 we considered Dense-NAPL infiltration into a water unsaturated porous medium that consists of two horizontal layers, of which the top layer has a lower intrinsic permeability than the bottom layer. The layer interface forms a barrier to DNAPL flow, which causes the DNAPL to spread out horizontally just above the interface. We have developed an analytical approximation to estimate the DNAPL pressure and saturation and the horizontal extension of the DNAPL plume just above the layer interface at steady state for low water saturations. The analytical approximation shows that the steady state DNAPL infiltration is determined by five dimensionless numbers: the heterogeneity factor γ, the Brooks and Corey capillary pressure parameter λ, the gravity number N_g, the ratio of the capillary and gravity numbers N_c/N_g, and the critical DNAPL pressure P_o^c, which indicates the effect of the water saturation on the flow of DNAPL. We compared its predictions with the results of a numerical three-

phase flow simulator for a number of parameter combinations. For most of these combinations the analytical approximation predicts the DNAPL pressure and saturation profiles at the interface adequately, although it slightly underestimates the horizontal spreading of the plume at the interface. Using the analytical approximation, we carried out a sensitivity study with respect to the maximum horizontal extension of the plume. The extension of the plumes appears to be highly sensitive to variation of the dimensionless numbers P_o^c, λ and γ. The extension increases for increasing values of λ and γ and for decreasing values of P_o^c.

Samenvatting

Grondwaterverontreiniging door organische vloeistoffen, zoals brandstoffen (benzine) en gechloreerde koolwaterstoffen, is een serieuze bedreiging voor de beschikbaarheid van schoon en veilig water voor mens en dier. Deze vloeistoffen zijn slecht mengbaar met water en stromen als een separate vloeistoffase door de bodem. Een klein deel lost op in het grondwater en vormt daarmee een bedreiging voor mens en milieu. In de literatuur worden deze organische verontreinigingen vaak aangeduid met de afkorting NAPL, naar het engelse Non-Aqueous Phase Liquids (vrij vertaald als 'vloeistoffen die geen water zijn'), hieronder zullen wij ze met olie aanduiden. Door bijvoorbeeld een lekkende pijpleiding of een lekkende ondergrondse olieopslag kan de olie in de bodem komen. Als er veel olie is gelekt, volgt deze zijn weg naar beneden door de poriën van de grond onder invloed van capillaire krachten en de zwaartekracht.

Om de belangrijkste processen en parameters te kunnen identificeren voor bijvoorbeeld saneringsdoeleinden, is een beter inzicht in de stroming van olie in de bodem van belang. Daartoe is er in dit proefschrift zowel experimenteel als modelmatig studie gedaan naar het gedrag van oliën in de bodem. We hebben ons met name gericht op het fysische gedrag van deze oliën in het onverzadigde deel van de bodem. Dit houdt in dat we de beweging, interactie en (her-)verdeling hebben bestudeerd van drie vloeistoffasen: water, olie en lucht in een poreus medium (de bodem). Het water wordt het sterkst aangetrokken door het poreuze medium, wat betekent dat het water de 'bevochtigende' vloeistof is ten opzichte van olie. Olie is vervolgens het meest bevochtigend ten opzichte van lucht. Deze bevochtigingvolgorde leidt tot typische stromingsgedrag. Twee belangrijke fenomenen die beiden gerelateerd zijn aan (3-fasen) stroming van olie in de onverzadigde zone worden in dit proefschrift belicht: (1) residuele olie na drainage en (2) het effect van gelaagdheid van de bodem op de stroming van olie.

Residuele olie na drainage is de olie die achterblijft in de poriën na een

138

lozing. De olie heeft in eerste instantie lucht verplaatst uit de poriën en is vervolgens zelf weer deels vervangen door lucht. Dit alles in de aanwezigheid van residueel water. Voor saneringsdoeleinden is het belangrijk om deze achtergebleven olie mee te nemen in de (meerfasen) stromingsmodellen, wat tot nu toe niet is gebeurd.

In Hoofdstuk 2 is een constitutieve set van saturatie-capillaire druk $(P_c - S)$ relaties uitgewerkt welke residuele olie verdisconteert. Deze set van vergelijkingen kan worden opgenomen in meerfasenstromingsmodellen. De relaties zijn afgeleid van een conceptueel model op porieschaal waarin de bodem wordt gerepresenteerd door een serie gestapelde bolletjes. Uit het model volgt dat olie residueel wordt wanneer de totale vloeistofsaturatie (van water en olie) gedaald is onder een zeker kritiek niveau, S_t^c. S_t^c is poreus medium en vloeistof afhankelijk. De residuele oliesaturatie wordt hoger wanneer de spreidingscoëfficiënt kleiner wordt en een hogere watersaturatie leidt tot een lagere residuele oliesaturatie. Het constitutieve model is toegepast op een experimentele meetreeks en bleek deze goed te simuleren. Echter, dit vormde een te smalle basis om de aannames die zijn gemaakt in het model te kunnen verifiëren.

Om het model te kunnen verifiëren hebben we een experimentele opstelling ontwikkeld die zowel drie-fasen $P_c - S$ relaties kan meten als residuele olie. Daarnaast voorziet de opstelling in onafhankelijke meting van watersaturatie en -druk ten opzichte van de oliesaturatie en -druk. Met de opstelling zijn vier experimenten gedaan. Het poreuze medium bestond uit kwartszand en de vloeistoffasen waren water, dodecaan en lucht. De gemeten residuele oliesaturatie was maximaal 0.081. We vonden geen correlatie tussen de watersaturatie en de residuele oliesaturatie. Dit zou kunnen betekenen dat andere mechanismen dan die welke door het constitutieve model waren voorzien, belangrijke invloed zouden kunnen hebben op de vorming van residuele olie. Voorafgaand aan het experiment is er een literatuurstudie gedaan naar beschikbare macroschaal experimentele data waarmee de relatie tussen residuele olie en de eigenschappen van een poreus medium en vloeistoffen duidelijker zou worden. Na een grondige selectie bleven er 26 residuele oliemetingen over verkregen van 9 referenties. De gemeten residuele oliesaturatie-waarden varieerde tussen 0.001 en 0.23. De data leverde alleen een duidelijke relatie op tussen de spreidingcoëfficiënt, C_s en de residuele olie, S_{or}; S_{or} neemt toe voor een kleinere C_s. Een uitgebreidere vergelijkende studie van de verschillende gebruikte poreuze media, en een systematische data acquisitie van S_{or} en andere macroschaal param-

eters zal nodig zijn om eventuele andere relaties te kunnen vaststellen.

Een overgang tussen twee verschillende bodemlagen van de poreus medi-umeigenschappen zoals doorlatendheid en porositeit, kan de stroming en distributie van olie sterk veranderen. De mobiliteit kan toenemen of afne-men bij een overgang tussen twee bodemlagen, afhankelijk van de doorla-tendheid van de lagen en de capillariteit en de bevochtiging van het poreuze medium door de olie in relatie tot water en lucht. De effecten van deze veranderingen op zo'n overgang tussen twee lagen zijn bestudeerd in de Hoofdstukken 4 en 5.

In Hoofdstuk 4 richtten wij ons op het effect van een schuine zandlaag in de bodem ten opzichte van het (horizontale) grondwaterniveau. Er zijn twee experimenten uitgevoerd in een doorzichtige bak gevuld met zand. De beweging van de vloeistoffen werden vastgelegd met een digitale camera. In het eerste experiment werd olie gedruppeld in een bak gevuld met fijn zand waarin een schuine grove zand laag is gelegd. In het tweede experiment werd de olie gedruppeld in een bak gevuld met grof zand waarin een schuine laag is gelegd van fijn zand. Het zand in beide experimenten was onverzadigd met water. The experimentele resultaten zijn numeriek gemodelleerd. Het gedrag van de olie die zowel experimenteel als modelmatig werd gevonden kon worden verklaard uit het feit dat olie in de onverzadigde zone twee soorten barrières tegen kan komen. Ten eerste kan het accumuleren en spreiden boven een grove zandlaag met een lage watersaturatie die zich gedraagt als een 'capillary barrier' voor de olie voordat het kan infiltreren. Ten tweede zal de olie zich ophopen en spreiden boven een water verzadigde laag van fijn zand die een hoge intreedruk heeft voor de olie. Er is tevens een gevoeligheidsanalyse uitgevoerd met het numerieke model. De analyse geeft aan dat de oliedistributie in het geval van schuine lagen hoofdzakelijk wordt bepaald door het capillaire contrast tussen de lagen.

Hoofdstuk 5 behandelt de infiltratie van olie in een onverzadigd poreus medium dat dit keer bestaat uit twee horizontale zandlagen, waarvan de toplaag een lagere doorlatendheid heeft dan de laag eronder. De over-gang tussen de zandlagen vormt een barrière voor de stroming van de olie waardoor de olie zich erboven horizontaal uitspreid. Een analytische be-nadering wordt afgeleid voor de oliedruk en -saturatie en de horizontale breedte van de olielaag net boven de overgang tussen de twee zandlagen voor een steady state situatie. De analytische benadering laat zien dat het stromingsprobleem wordt bepaald door vijf dimensieloze parameters: de heterogeneitsfactor γ, de Brooks and Corey capillaire druk parameter λ,

het gravitatie-getal N_g, de ratio tussen het gravitatie en het capillaire getal $\frac{N_c}{N_g}$, en de kritische oliedruk P_o^c. De laatste geeft het effect van de watersaturatie op de overgang tussen de zandlagen weer. De analytische benadering is vergeleken met de resultaten van een numeriek stromingsmodel voor een aantal parametercombinaties. Hoewel er een lichte onderschatting is van de spreiding van de olielaag, geeft de analytische benadering voor het grootste deel van de combinaties een adequate voorspelling van de oliedrukken en saturaties boven de overgang tussen de zandlagen. Met behulp van de analytische benadering is er een gevoeligheidsstudie uitgevoerd naar het effect op de breedte van de olielaag. Deze breedte blijkt tamelijk gevoelig voor de dimensieloze getallen P_o^c, λ en γ (De breedte van de olielaag groeit voor grotere λ en γ waarden en voor kleinere P_o^c waarden).

Nawoord

Het boekje dat nu voor je ligt is het resultaat van vijf jaar onderzoek waarin ik de interactie tussen olie, water, lucht en zand heb bestudeerd. Dit onderzoek heb ik altijd met veel plezier gedaan. Vooral de eerste drie jaar vond ik erg prettig; er was nog geen echte deadline in zicht en ik kon in grote vrijheid mijn werk vormgeven en uitbouwen. Ik kreeg verder de mogelijkheid vele congressen, cursussen en workshops te bezoeken wat zeer motiverend werkte. Zoals waarschijnlijk veel promovendi met mij, kijk ik nu bij het afronden van het proefschrift terug op een turbulent laatste jaar. Het proefschrift moest af, ik had een nieuwe baan in het verschiet en moest mijn secretarisfunctie bij Gaia nog afronden. Daarnaast had ik de zorg voor Sophie. Maar gelukkig kreeg ik de steun van velen om mij heen die mij hebben geholpen door deze periode heen te komen. Daarvoor wil ik iedereen; vrienden, collega's en familie bedanken.

In dit nawoord wil ik graag een aantal mensen specifiek noemen die direct danwel indirect een bijdrage hebben geleverd aan dit proefschrift.

Ten eerste wil ik Sjoerd bedanken als begeleider. Ik vond onze samenwerking prettig. Je hebt een coachende stijl van begeleiden en je liet me veel vrijheid om mijn eigen onderzoek te sturen. Iets waar ik dankbaar gebruik van heb gemaakt. Vooral de stap om zelf een experiment op te zetten heb je gesteund. Het is jammer dat de resultaten van het experiment niet geheel zijn geworden wat we ervan verwacht hadden. Desalniettemin, vond ik het een leuke ervaring en heb ik gemerkt dat juist de combinatie van modelleren en experimenteren mij erg goed ligt.

Ik wil ook Annemieke Marsman en Rink van Dijke bedanken. Annemieke was vijf jaar lang mijn kamergenoot en collega en daarnaast hebben we ook nog enkele jaren samen gecarpooled. Annemieke, ik vond het erg leuk om met jou de dagelijkse beslommeringen te becommentariëren en te delen, om met jou inhoudelijk te discussiëren en natuurlijk om samen naar Oslo, Boston, New York, Delft etc. te gaan. Daarnaast wil ik je bedanken

141

voor het lezen en becommentariëren van enkele hoofdstukken van dit proefschrift. Ik vind het erg leuk dat we nu weer collega's zijn geworden. Rink, hoewel onze samenwerking pas in 2002 echt op gang kwam, vond ik deze erg prettig. Ik vond het ook erg inspirerend om in Edinburgh op bezoek te komen. Je hebt behoorlijk aan hoofdstuk 5 gesleuteld, maar het is dan ook erg goed geworden, vind ik. Wie weet krijgt onze samenwerking nog eens een vervolg.

Daarnaast wil ik Gijs Breedveld en Marianne Ness van het Noorse Geotechnische Instituut in Oslo bedanken voor de samenwerking en inzet betreffende het experiment van Hoofdstuk 4. Zoals jullie hebben gemerkt heb ik een van jullie producten op de voorpagina geplaatst. Ik vond dat de foto goed verbeeldde wat heterogeniteit en capillariteit voor een patronen kunnen opleveren bij indringing van olie in de bodem. I thank Mr. H. Kallevik from Statoil Trondheim, Norway for providing the interfacial tension of Jet Fuel A.

Bij de opzet en uitwerking van het experiment dat is beschreven in Hoofdstuk 3 heb ik de steun gehad van met name Simon Maasland die gedurende het gehele ontwerp- en uitvoeringsproces mij (technisch) heeft ondersteund en heeft meegeleefd. Daarnaast heb ik steun gehad vanuit het Dietz Laboratorium van de Technische Universiteit Delft in de persoon van André Hoving. André heeft geholpen met het ontwikkelen en uitvoeren van de roestvrijstalen uitvoering van het experiment nadat enkele kunststofexemplaren toch niet bestand bleken tegen de verschillende oliën. Ook Ernst Went wil ik niet vergeten, die er uiteindelijk voor heeft gezorgd dat het experiment luchtdicht werd.

Voor het beschikbaar stellen van de numerieke code STOMP voor de meerfasenstromingsberekeningen wil ik Mart Oostrom van het 'Pacific Northwest National Laboratory' in Richland, US bedanken. Ook wil ik Cor Hofstee bedanken voor het beschikbaar stellen van zijn experimentele data. We zullen in de toekomst nog verder werken op het gebied van residuele olie en niet-spreidende vloeistoffen in een andere setting. Ik ben benieuwd welke nieuwe inzichten nog naar boven zullen komen.

Voor de gezellige klets tijdens de lunches en andere gelegenheden wil ik de (oud-)aio's en collega's van Bodemkwaliteit bedanken. Ik vond het altijd erg prettig in de kelder en de grote mate van solidariteit heb ik altijd erg gewaardeerd.

Tot slot wil ik natuurlijk vooral Kit Buurman, mijn vriend en partner bedanken voor zijn steun en voor het geven van een fijn thuis, samen met Sophie, waar ik altijd op kan terugvallen.

Louise

Curriculum Vitae

Louise Wipfler werd geboren op 1 augustus 1970 te Zevenaar. In 1988 behaalde zij het VWO diploma aan het St. Ludger College te Doetinchem. Na een korte periode Bouwkunde te hebben gestudeerd aan de Technische Universiteit Delft, begon zij in 1990 aan de studie Civiele Techniek aan dezelfde universiteit. Zij studeerde in 1995 af bij de vakgroep Waterbeheer, Milieu- en Gezondheidstechniek bij de sectie Geohydrologie. Haar afstudeeronderzoek was getiteld: Een nieuw transportmodel voor verontreiniging in grondwater. In 1996 en 1997 was zij werkzaam als wetenschappelijk gastmedewerker aan de Technische Universiteit van Catalonië, Spanje. Zij deed daar onderzoek op het gebied van de stochastische geohydrologie.

In 1998 startte zij als promovenda bij de Wageningen Universiteit bij de vakgroep Bodemkwaliteit. Zij werkte daar zowel experimenteel als modelmatig aan meerfasenstroming van organische vloeistoffen in de bodem. De belangrijkste resultaten van haar promotieonderzoek staan in dit proefschrift beschreven. De laatste twee jaar van haar promotieonderzoek zette zij zich tevens in voor de positie van Nederlandse 'aardwetenschappelijke' vrouwen als secretaris van Gaia, het netwerk voor vrouwen uit de Aardwetenschappen.

Vanaf maart 2003 is zij werkzaam als onderzoeker bij het Nederlands Instituut voor Toegepaste Geowetenschappen (TNO) bij de sectie Geosaneringsonderzoek.